Strong-field induced plasma formation in solid dielectrics

im Fachbereich Physik der Freien Universität Berlin eingereichte

Dissertation

zur Erlangung des akademischen Grades
doctor rerum naturalium
(Dr. rer. nat.)
vorgelegt von

Peter Jürgens

im Dezember 2019

Diese Arbeit wurde zwischen Oktober 2015 und März 2019 am *Max-Born-Institut für nichtlineare Optik und Kurzzeitspektroskopie im Forschungsverbund Berlin e.V.* angefertigt.

Erstutachter:	Prof. Dr. Marc J.J. Vrakking
Zweitgutachter:	Prof. Dr. Thomas Baumert

Tag der Disputation: 10.12.2020

4π

Short Summary

The buildup of an electron-hole plasma during the interaction of a solid dielectric with intense, ultrashort laser pulses entails a wealth of successive processes. The dynamics of the strong-field induced plasma are thereby of utmost interest for both fundamental research as well as for optimizing industrial applications. In particular, the relative importance of the various excitation mechanisms participating in the production of the electron-hole plasma is of substantial relevance. This thesis aims at elucidating the relative contribution of the two major excitation mechanisms - strong-field and electron-impact ionization - to the generation of an electron-hole plasma in strong-field driven solid dielectrics.

The first two chapters of this thesis are dedicated to a theoretical description of the fundamental, ultrafast, light-matter interaction and resulting phenomena. Afterwards, the experimental apparatus, designed and implemented to enable two-color pump-probe experiments in transparent solids, is described. Results obtained by characterizing the absorption of a weak probe laser pulse during propagation through an excited region of a bulk a-SiO_2 sample shed light on the ultrafast excitation and relaxation dynamics in fused silica. In contrast to previously reported findings, the results show a strong dependence of the relaxation time on the intensity of the mid-infrared pump laser pulse. An explanation based on the detrapping of self-trapped carriers due to vibrations of the crystal lattice is proposed.

In a second set of time-resolved experiments low-order harmonics generated by a two-color field in fused silica are analyzed regarding their underlying nonlinear generation process. By linking the experimental results to numerical simulations, a previously unreported ionization current is identified as the main source of low-order harmonic generation in strongly excited SiO_2. A further analysis of the corresponding phase matching condition indicates that a novel self-quasi-phase matching mechanism, associated with the formation of a quasi-stationary wave close to the rear surface of the target significantly enhances the conversion efficiency of the wave mixing process.

Finally, the results are linked and interpreted enabling the reconstruction of the strong-field induced plasma formation and the identification of the relative role of strong-field and electron-impact ionization. Based on the discussed findings it is demonstrated that electron-impact ionization is the prevailing excitation mechanism in laser-excited SiO_2 at intensities close to the damage threshold.

The presented results offer tremendous potential for future advanced plasma diagnostics and provide an original approach for the optimization of laser-micromachining applications in dielectric materials.

Kurzzusammenfassung

Die Erzeugung eines Elektron-Loch-Plasmas während der Wechselwirkung von Dielektrika mit intensiven, ultrakurzen Laserpulsen zieht eine Vielzahl von Folgeprozessen nach sich. Dabei ist die Dynamik des vom Laserfeld erzeugten Plasmas, sowohl für die Grundlagenforschung als auch für industrielle Anwendungen von großem Interesse. Insbesondere der relative Beitrag der verschiedenen Anregungsmechanismen, die zu der Produktion des Elektron-Loch-Plasmas beitragen, ist von erheblicher Relevanz. Ziel der vorliegenden Dissertation ist daher die Analyse der relativen Rolle der zwei Hauptanregungsmechanismen - Starkfeld- und Stoßionisation - in der Erzeugung des Plasmas in laserangeregten Dielektrika.
Die ersten zwei Kapitel dieser Arbeit widmen sich der theoretischen Beschreibung der fundamentalen Licht-Materie-Wechselwirkung und den daraus resultierenden Phänomenen auf ultrakurzen Zeitskalen. Anschließend ist der experimentelle Aufbau für zeitaufgelöste Messungen in transparenten Festkörpern beschrieben.
Die Charakterisierung der Absorption eines schwachen Abfragepulses nach der Propagation durch einen angeregten Bereich einer Quarzglasprobe liefert experimentelle Daten zu ultraschnellen Anregungs- und Relaxationsdynamiken des erzeugten Elektron-Loch-Plasmas. Die dargestellten Resultate weisen im Gegensatz zu bereits veröffentlichten Ergebnissen eine starke Abhängigkeit der Relaxationszeit von der Laserintensität auf. Ein auf einer erneuten Anregung von gefangenen Ladungsträgern durch die Vibrationen des Kristallgitters basierender Erklärungsansatz wird diskutiert.
In einer zweiten experimentellen Studie werden Harmonische niedriger Ordnung von zwei Laserpulsen unterschiedlicher Wellenlänge in SiO_2 erzeugt und hinsichtlich des zugrundeliegenden Erzeugungsmechanismus analysiert. Die Verknüpfung der experimentellen Ergebnisse mit numerischen Simulationen offenbart einen bisher unbekannten Beitrag, den Ionisationsstrom, als dominierende Quelle zur Erzeugung niedriger Harmonischer in laserangeregtem Quarzglas. Die Analyse der zugehörigen Phasenanpassungsbedingung deutet auf einen neuartigen, mit der Ausbildung einer stehenden Welle nahe der Rückseite des Substrates assoziierten, Quasiphasenanpassungsmechanismus hin.
Abschließend ermöglicht die Verknüpfung und Interpretation der beschriebenden Ergebnisse die Rekonstruktion des durch Starkfeldionisation erzeugten Elektron-Loch-Plasmas und die Identifikation der relativen Rolle von Starkfeld- und Stoßionisation. Basierend auf den erhaltenen Resultaten kann eindeutig nachgewiesen werden, dass unter den gegebenen experimentellen Bedingungen Stoßionisation der dominierende Anregungsprozess in laserangeregtem Quarzglas nahe der Zerstörschwelle ist.
Die vorgestellten Ergebnisse weisen auf ein immenses Potenzial für zukünftige Plasmadiagnosemethoden hin and stellen einen neuartigen Ansatz für die Optimierung von laserinduzierten Modifikationen in Dielektrika dar.

Table of Contents

Chapter 1

Introduction

The formation of an electron-hole plasma during the interaction of an intense ultrashort laser pulse with a solid dielectric constitutes the first step in a chain of events leading to a permanent modification of the material. At sufficient laser intensities the electric field of the laser pulse is able to promote initially bound electrons from the valence to anti-bonding states in the conduction band by nonlinear excitation mechanisms. The removal of electrons from bonding states not only alters the optical properties of the irradiated target but also induces a softening of the crystal lattice. A subsequent relaxation of the conduction band electron density leads to defect formation resulting in permanent structural changes. A plethora of applications such as data storage [1], writing of waveguides [2, 3] and waveguide splitters [4] and a multitude of cutting purposes [5, 6] to name but a few rely on the modification of transparent materials by intense laser radiation. Thereby, fused silica is often used as a model material because of its mechanical, optical and chemical stability.
The utilization of ultrashort laser pulses in the femtosecond (fs) regime instead of longer pulse durations holds several advantages [7]. In particular the probability for the excitation of electrons from the valence to the conduction band strongly depends on the intensity of the incident laser field. Therefore, in order to reach the necessary threshold intensity for the formation of an electron-hole plasma the associated energy per pulse is significantly reduced for fs pulses. Shorter pulses with smaller pulse energies lead to a smaller amount of energy coupled into the material. Hence, a smaller heat affected zone is generated in the irradiated sample compared to longer pulses of the same intensity. The laser-induced changes of the material are furthermore spatially confined due to the nonlinearity of the excitation process. This enables high-precision micromachining and writing of complex three-dimensional geometrical structures.
While micromachining of transparent materials using fs laser pulses has already been demonstrated more than two decades ago [8, 9], current research focuses on the interaction of transparent solids with even shorter - few-cycle - pulses [10–

13]. Few-cycle laser pulses are nowadays routinely generated by either spectral broadening in gas-filled hollow-core fibers followed by external pulse compression [14, 15] or by optical parametric chirped pulse amplification (OPCPA) [16, 17]. Employing few-cycle laser pulses for micromachining of transparent solids promises further improvement of the precision and controllability of the modification process. However, a potential refinement of laser-induced modification techniques in solid dielectrics not only relies on the availability of few-cycle laser sources. Rather, a precise understanding of the underlying fundamental mechanisms leading to the structural modifications of the target is crucial.
With regards to the tremendous potential of ultrashort pulse laser micromachining [18–21] a lot of theoretical and experimental efforts have been devoted to the description of the laser-matter interaction at intensities around the threshold for an irreversible laser-induced modification. Experimental studies have clarified many aspects related to the relaxation of the electron-hole plasma from the picosecond (defect formation) to the microsecond (heat diffusion) timescales. However, the scenario of the laser-matter interaction remains obscure at shorter timescales. In particular, little is known on the formation of the electron-hole plasma on a sub-cycle timescale and on the respective contributions of the ionization channels. Although the main excitation mechanisms are unequivocally established as strong-field and electron-impact ionization their relative importance still remains undetermined. Thus, a further investigation of the fundamental excitation mechanisms on their natural timescale is indispensable for an optimized energy coupling from the laser field to the material.
Experimentally distinguishing the influence of strong-field and electron-impact ionization is rather challenging since both mechanisms lead to intrapulse dynamics of the plasma density. The partially simultaneous occurrence is impeding the isolation of carrier dynamics caused by one of the two processes. Indirect measurements performed to reveal the relative role of strong-field and electron-impact ionization only allow the identification of the prevailing excitation mechanism [22, 23].
Accordingly, a major part of this thesis is dedicated to unraveling the intrapulse dynamics of plasma formation due to strong-field and electron-impact ionization. Time-resolved absorption measurements have emerged as a reliable tool for the characterization of plasma dynamics in strongly excited solid dielectrics. However, a disentanglement of the plasma formation due to strong-field and electron-impact ionization requires an additional observable. Within this thesis the optical signature of strong-field ionization is exploited to extract the plasma dynamics solely induced by strong-field ionization. The high nonlinearity and phase sensitivity of strong-field ionization leads to the generation of high frequency photons [24]. Thus, the resulting harmonic emission maps attosecond ionization dynamics into the frequency domain [25, 26]. Time-resolved detection of the generated harmonics yields full information on the dynamics of the conduction band electron density produced by strong-field ionization. A measurement of the time-resolved absorption by a laser-induced electron-hole plasma combined

with a simultaneous characterization of the harmonics generated by strong-field ionization therefore promises to reveal the relative role of the two competing ionization mechanisms.
This thesis is organized as follows.
Chapter 2 reviews the basic concepts governing ultrafast laser-matter interaction. In the first section the influence of nonlinear effects on the propagation of ultrashort laser pulses through transparent materials is discussed. The second section provides details on the dynamics of the electron-hole plasma generated by a strong laser field. Since harmonic radiation due to strong-field ionization constitutes the main observable of this thesis, Ch. 3 is dedicated to the fundamental mechanisms of harmonic generation in solids. The different possible mechanisms leading to the emission of harmonics of an intense electromagnetic field from solid targets are presented and compared to atomic high-order harmonic generation. Ch. 4 contains a description of the experimental apparatus constructed to analyze the dynamics of plasma formation in transparent materials. Furthermore, the characterization of the laser pulses used in the experiments is included in Ch. 4. Time-resolved experiments on excitation and relaxation dynamics in laser-excited fused silica are discussed in Ch. 5. The observed intensity dependence of the relaxation time of the generated electron-hole plasma is attributed to a vibrational activation of the medium. Chapter 6 aims at uncovering the underlying mechanism leading to the generation of low-order harmonics in amorphous fused silica excited by a strong laser field. The main result that is reported in Ch. 6 is a novel mechanism for the formation of low-order harmonics that previously had not been considered in the literature. This mechanism is directly related to the nonlinear current associated with the excitation of electrons from the valence to the conduction band. Experiments performed in order to analyze the phase matching condition of the wave mixing process are discussed in Ch.7 indicating that a self-regulating quasi-phase matching mechanism significantly enhances the efficiency of the frequency conversion process. Chapter 8 consists of two parts. In the first section a phase retrieval algorithm is applied on a time-resolved spectrum containing low-order harmonics generated in SiO_2 to retrieve the strong-field ionization dynamics with sub-cycle precision. The second section of Ch. 8 combines results presented in Ch. 5 & Ch. 6 to analyze the relative contribution of strong-field and electron-impact ionization to the total generated electron-hole plasma. Chapter 9 summarizes the main results of this thesis and provides a discussion on possible future developments in the field of ultrafast light-matter interaction and possible implications for laser processing of transparent solids.

Chapter 2

Fundamentals of ultrafast light-matter interaction in solid dielectrics

Every permanent modification of a target irradiated with ultrashort laser pulses is based on the formation of an electron-hole plasma inside the material [27, 28]. The generated plasma serves as an energy reservoir to fuel the subsequent lattice reorganization and therefore mainly determines the resulting modification. Hence, a precise control of the plasma formation is an essential prerequisite towards the optimization of the laser-induced material modification.
The following chapter provides a brief overview of the fundamentals of laser-induced plasma formation in solid dielectrics. Once an ultrashort laser pulse (USP) enters a material, nonlinear effects start to influence the propagation. These nonlinear propagation effects are addressed in Sec. 2.1. If the intensity of the USP exceeds a certain threshold an electron-hole plasma is generated in the irradiated target. A theoretical description of the excitation and relaxation mechanisms together with simplified numerical approximations of the resulting carrier dynamics is given in Sec. 2.2.

2.1 Nonlinear propagation effects

The propagation of an USP in a dielectric material is heavily influenced by the temporal and spatial properties of the incident electric field. Generally, the electric field forces the charges to move. Positively charged ionic cores are driven in the direction of the laser field and negatively charged electrons are moved in the opposite direction. This charge separation induces a polarization in the material. Since the ionic mass is much larger than the mass of the electrons the ionic movement is negligible compared to that of the electrons in high frequency fields. Hence, only considering the electrons is usually sufficient to describe the

response of a material to an intense, pulsed electric field.
The resulting movement of the electrons is determined by the sum of the external force given by the electric field of the laser pulse and the interatomic Coulomb force. If the resulting force is small compared to the force resulting from the interatomic potential the electrons are only slightly displaced and the polarization $\mathbf{P}(t)$ is linearly dependent on the electric field strength $\mathbf{E}(t)$ [29]:

$$\mathbf{P}(t) = \mathbf{P}^{\mathrm{L}}(t) = \epsilon_0 \chi^{(1)} \mathbf{E}(t). \tag{2.1.1}$$

However, if the incident electromagnetic field is sufficiently strong the resulting polarization contains nonzero higher order terms bundled in the so-called nonlinear polarization $\mathbf{P}^{\mathrm{NL}}$. As a consequence $\mathbf{P}^{\mathrm{NL}}$ influences the interaction between the laser pulse and the irradiated target. The total polarization can be expressed as a power series in the strength of the electromagnetic field:

$$\begin{aligned} \mathbf{P}(t) &= \mathbf{P}^{L} + \mathbf{P}^{\mathrm{NL}} \\ &= \mathbf{P}^{(1)}(t) + \mathbf{P}^{(2)}(t) + \mathbf{P}^{(3)}(t) + \dots \\ &= \epsilon_0 \left[\chi^{(1)} \mathbf{E}(t) + \chi^{(2)} \mathbf{E}^2(t) + \chi^{(3)} \mathbf{E}^3(t) + \dots \right], \end{aligned} \tag{2.1.2}$$

where $\chi^{(j)}$ is the j-th order optical susceptibility. The following section discusses the influence of the nonlinear polarization on the light-matter interaction.

2.1.1 Self-focusing

The intensity-dependent refractive index Assuming a linearly polarized, monochromatic laser field of the form

$$E(t) = E(\omega) \exp(-i\omega t) + C.C., \tag{2.1.3}$$

the resulting nonlinear polarization influencing the propagation of a laser beam with the fundamental frequency ω - $P^{\mathrm{NL}}(\omega)$ - reads according to Eq. 2.1.2 [29]:

$$P^{\mathrm{NL}}(\omega) = 3\epsilon_0 \chi^{(3)}(\omega = \omega + \omega - \omega) |E(\omega)|^2 E(\omega). \tag{2.1.4}$$

Due to the linearly polarized laser electric field, the tensor nature of the third-order nonlinear susceptibility $\chi^{(3)}$ is suppressed. Combining the linear and the nonlinear polarization leads to a total polarization given by:

$$\begin{aligned} P^{\mathrm{tot}}(\omega) &= P^{\mathrm{L}}(\omega) + P^{\mathrm{NL}}(\omega) \\ &= \epsilon_0 \chi^{(1)}(\omega) E(\omega) + 3\epsilon_0 \chi^{(3)} |E(\omega)|^2 E(\omega) \\ &\equiv \epsilon_0 \chi_{\mathrm{eff}} E(\omega). \end{aligned} \tag{2.1.5}$$

Here, the effective susceptibility

$$\chi_{\text{eff}} \equiv \chi^{(1)} + 3\chi^{(3)}|E(\omega)|^2, \tag{2.1.6}$$

was introduced. In order to relate the refractive index of the material n to the effective susceptibility the Maxwell relation

$$n^2 = 1 + \chi_{\text{eff}}, \tag{2.1.7}$$

can be exploited. Inserting Eq. 2.1.6 into Eq. 2.1.7 and assuming a modified refractive index of $n = n_0 + \Delta n$ with linear refractive index n_0 and a field-induced refractive index variation Δn yields

$$(n_0 + \Delta n)^2 = 1 + \chi^{(1)} + 3\chi^{(3)}|E(\omega)|^2. \tag{2.1.8}$$

Assuming $\Delta n \ll n_0$ this expression can be simplified to

$$n_0^2 + 2n_0\Delta n \approx \underbrace{1 + \chi^{(1)}}_{=n_0^2} + 3\chi^{(3)}|E(\omega)|^2, \tag{2.1.9}$$

and the remaining field-induced variation of the total refractive index reads

$$\Delta n = \frac{3\chi^{(3)}|E(\omega)|^2}{2n_0}. \tag{2.1.10}$$

Inserting the intensity of the incident laser field given by

$$I = 2n_0\epsilon_0 c|E(\omega)|^2, \tag{2.1.11}$$

enables rewriting Δn as:

$$\Delta n = \frac{3\chi^{(3)}I}{4n_0^2\epsilon_0 c}. \tag{2.1.12}$$

Here, ϵ_0 denotes the dielectric constant and c the speed of light. After defining the nonlinear refractive index n_2 as:

$$n_2 \equiv \frac{3\chi^{(3)}}{4n_0^2\epsilon_0 c}, \tag{2.1.13}$$

Eq. 2.1.8 may be reformulated to emphasize the intensity dependence of n:

$$n = n_0 + n_2 I. \tag{2.1.14}$$

The above relation between the intensity of an electromagnetic field and the refractive index of the irradiated material is known as the optical Kerr-effect. One important effect based on the intensity dependence of the refractive index is self-focusing. Self-focusing describes a process in which an intense light beam

modifies the optical properties of the irradiated medium leading to focusing ($n_2 > 0$) or defocusing ($n_2 < 0$) of the beam [30]. For small laser intensities the index of refraction remains more or less unchanged while for sufficiently high laser intensities the optical path is extended. An optical path difference between different parts of the beam with different intensities leads to a curvature of the wavefront resulting in a focusing of the beam - concave curvature of the phasefront - for a positive n_2. A schematic description of self-focusing is given in Fig. 2.1.1. The drawing shows the self-focusing of a laser beam with a Gaussian spatial profile in a nonlinear medium with positive nonlinear index of refraction n_2. The intensity in the outer parts of the beam is significantly smaller than in the center resulting in a concave curvature of the wavefront. Thus, the propagation in a nonlinear medium effectively reduces the beam diameter - analogous to a focusing lens.

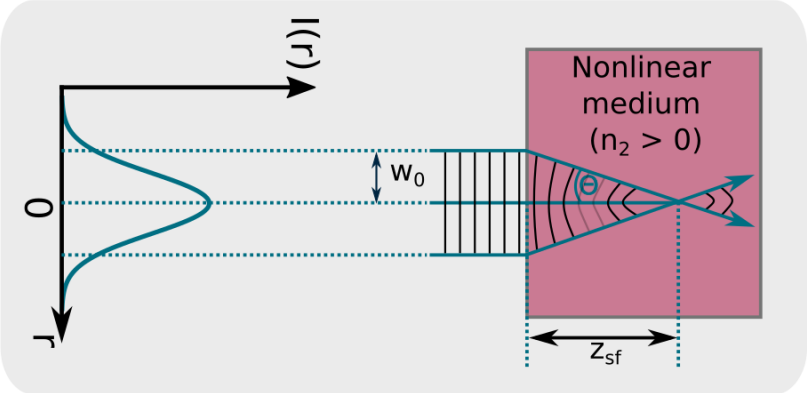

Fig. 2.1.1: Schematic of self-focusing in a nonlinear medium: An initially Gaussian spatial intensity distribution $I(r)$ (with $1/e^2$ radius w_0) is focused with a focal length of z_{sf} (see Eq. 2.1.20) due to the intensity-dependent refractive index in a nonlinear material with a positive nonlinear index of refraction ($n_2 > 0$).

Mathematical description of self-focusing The distance from the input surface to the focus z_{sf} can be calculated by using Fermat's principle for a beam diameter that is significantly larger than the wavelength of the incident electromagnetic field [29]. Based on the assumption that the optical path length of all rays from the input surface to the focus has to be equal it follows that

$$(n_0 + n_2 I) z_{\mathrm{sf}} = \frac{n_0 z_{\mathrm{sf}}}{\cos\theta} \tag{2.1.15}$$

with the focusing angle θ (see Fig. 2.1.1). Using the approximation

$$\cos\theta \approx 1 - \frac{1}{2}\theta^2 \tag{2.1.16}$$

the expression for the focusing angle reads

$$\theta = \sqrt{2n_2 I/n_0}. \tag{2.1.17}$$

θ is related to the beam width via $\theta = w_0/z_{\mathrm{sf}}$. Hence the self-focusing distance z_{sf} can be evaluated to

$$z_{\mathrm{sf}} = w_0\sqrt{\frac{n_0 + n_2 I}{2n_2 I}}. \tag{2.1.18}$$

Self-focusing only occurs if the power inside the laser beam exceeds a critical power P_{crit} that is given by [29]

$$P_{\mathrm{crit}} = \frac{\pi(0.61)^2\lambda_0^2}{8n_0 n_2}. \tag{2.1.19}$$

Inserting this expression into Eq. 2.1.18 the self-focusing distance can be rewritten as

$$z_{\mathrm{sf}} = \frac{2n_0 w_0^2}{\lambda_0}\frac{1}{\sqrt{P/P_{\mathrm{crit}}}} \qquad (\text{for} \quad P \gg P_{\mathrm{crit}}). \tag{2.1.20}$$

Figure 2.1.2 displays the self-focusing distance following from Eq. 2.1.20 as

	Symbol	Description	Value
Fused Silica	E_g	bandgap energy	7.5 eV
	n_0 (@800 nm)	linear refractive index	1.45 [31]
	n_0 (@2100 nm)	linear refractive index	1.43 [32]
	n_2	nonlinear refractive index	$3.2 \times 10^{-16}\,\mathrm{cm^2\,W^{-1}}$
	m^*	effective conduction electron mass	$0.635\,\mathrm{m_e}$
	τ_{rel}	free carrier relaxation time	220 fs
Physical constants	e	elementary charge	$1.602 \times 10^{-19}\,\mathrm{C}$
	m_{e}	electron rest mass	$9.109 \times 10^{-31}\,\mathrm{kg}$
	ϵ_0	vacuum permittivity	$8.854 \times 10^{-12}\,\mathrm{A\,s\,V^{-1}\,m}$
	c	Speed of light in vacuum	$2.99 \times 10^{8}\,\mathrm{m\,s^{-1}}$

Table 2.1.1: Material parameters of fused silica and physical constants used in the numerical simulations.

a function of the laser power expressed in units of P_{crit}. Independent of the initial beam size, z_{sf} decreases for increasing laser power due to the stronger focusing effect for higher field strengths. Since the resulting focal length due to self-focusing z_{sf} is on the order of the thickness of typically used transmissive optical components it is one of the major sources of catastrophic damage in high-power laser systems [33–37].

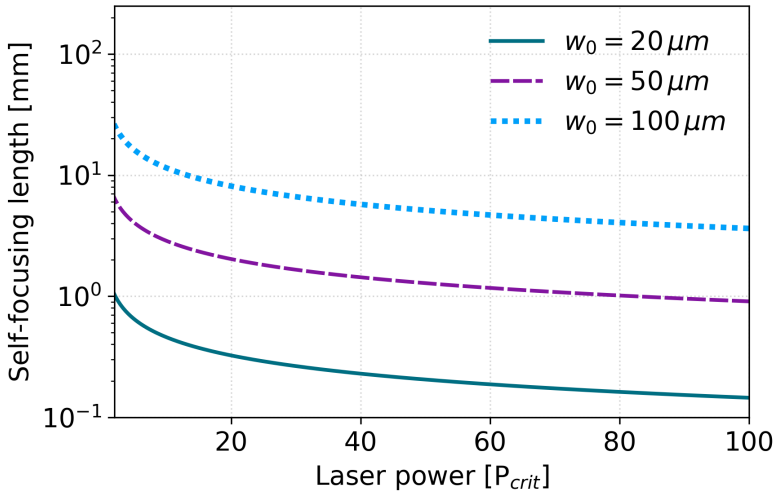

Fig. 2.1.2: Self-focusing length according to Eq. 2.1.20 as a function of the laser power expressed in units of the critical power for self-focusing. Laser wavelength: 800 nm, Material: Fused Silica (Parameters used given in Tab. 2.1.1).

2.1.2 Self-phase modulation

While self-focusing results in an alteration of the wavefront of an optical pulse upon propagation in a nonlinear medium, self-phase modulation (SPM) results in an alteration of the phase of the laser field. Considering a laser pulse of the form

$$E(z,t) = E_0(z,t)\exp[i(kz - \omega_0 t)] + C.C., \tag{2.1.21}$$

that propagates in z-direction through a medium with an intensity-dependent refractive index given by

$$n = n_0 + n_2 I, \tag{2.1.22}$$

a time-dependent refractive index modulation is induced that follows the temporal profile of the incident pulse. Assuming an instantaneous response of the material to the laser pulse and a sufficiently short interaction length L so that other nonlinear propagation effects can be neglected, the accumulated phase of the transmitted pulse is given by [29]

$$\phi_{\mathrm{NL}} = -n_2 I(t)\,\omega_0 \frac{L}{c}. \tag{2.1.23}$$

Since the instantaneous frequency follows from the time derivative of the phase, SPM leads to a temporal variation of the frequency of the laser field. This

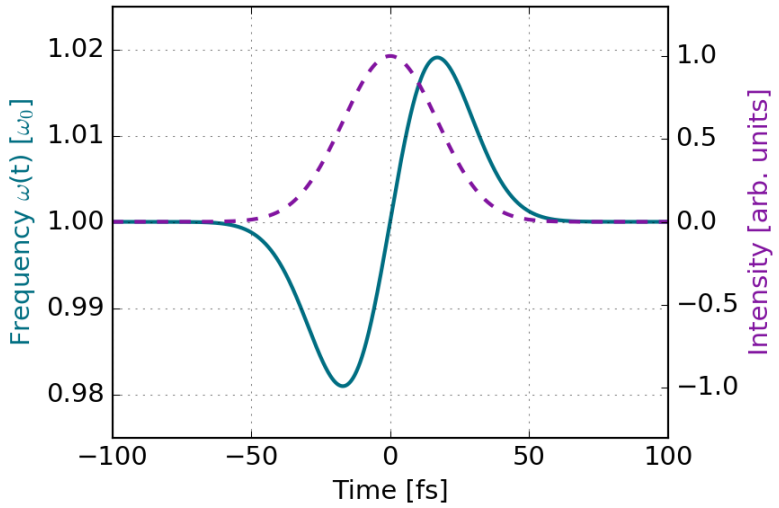

Fig. 2.1.3: Variation of the instantaneous laser frequency $\omega(t)$ (normalized with respect to the initial frequency ω_0) according to Eq. 2.1.24 for a central laser wavelength of $\lambda_0 = 800\,\mathrm{nm}$, a peak intensity of $5\,\mathrm{TW\,cm^{-2}}$ and an interaction length L of $100\,\mu\mathrm{m}$ in fused silica with a nonlinear refractive index of $3.2 \times 10^{-20}\ \mathrm{m^2\,W^{-2}}$ [29].

frequency variation is given by:

$$\omega(t) = \omega_0 + \delta\omega(t). \tag{2.1.24}$$

Here, $\delta\omega(t)$ denotes the SPM-induced instantaneous frequency variation of the laser field given by:

$$\delta\omega(t) = \frac{\partial\phi_{\mathrm{NL}}(t)}{\partial t}. \tag{2.1.25}$$

Figure 2.1.3 depicts the variation of the central frequency during a laser pulse with a Gaussian temporal shape. In the leading edge of the pulse the laser frequency is redshifted while the trailing edge experiences a blueshift. Owing to the properties of the derivative (see Eq. 2.1.25), the magnitude of the SPM-induced frequency variation is symmetric around the carrier frequency.

SPM is responsible for a spectral broadening of the pulse transmitted through a nonlinear medium. This effect is often used for the generation of few-cycle pulses by spectral broadening in gas-filled hollow core fibers [14, 15, 38–40] and subsequent compression (e. g. by chirped mirrors).

In a two-pulse configuration consisting of a strong pump and a weak probe laser pulse, the weak probe pulse can experience variations in the instantaneous frequency caused by the pump-induced refractive index variation. This effect is known as cross-phase modulation (XPM) [41, 42]. Thus, the temporal profile of the pump laser pulse is mapped onto a time-dependent refractive index variation

in the material. This variation can be read out by recording the instantaneous central frequency of the probe laser pulse as a function of the pump-probe delay. A possible application is given by the characterization of the temporal structure of the pump laser pulse assuming that the probe laser pulse has been well characterized beforehand [43, 44].

2.2 Strong-field induced carrier dynamics in solid dielectrics

In solid dielectrics, the electronic processes induced by an intense electromagnetic field lead to the formation of an electron-hole plasma. The generation of this electron-hole plasma holds the key to many subsequent processes in the interaction of ultrashort laser pulses with matter. The excitation of electrons from bound states in the valence to anti-bonding states in the conduction band leads to lattice-softening while the relaxation of the electron-hole plasma provides the energy for a structural modification of the crystal lattice. The formation of the electron-hole plasma mainly relies on two nonlinear excitation mechanisms: strong-field ionization (SFI), including multiphoton and tunneling-ionization, and electron-impact ionization (IMP).
Due to the large number of phenomena based on the formation of an electron-hole plasma in both fundamental research and industrial applications, tremendous theoretical and experimental effort was put into improving the understanding of ultrafast excitation processes in solid targets (see e.g. [12, 31, 45–51]). Especially, the relative importance of the two major excitation mechanisms (SFI and IMP) still remains a topic of intense debate.
The promotion of initially bound electrons from the valence to the conduction band by SFI and IMP will be covered in Sec. 2.2.1 & 2.2.2, respectively. Section 2.2.3 discusses how the optical properties of a solid dielectric are affected by the generation of an electron-hole plasma. The relaxation of the quasi-free electrons generated by either SFI or IMP is reviewed in Sec. 2.2.4. Further, the excitation and relaxation mechanisms are combined into a unified description of the strong-field induced, ultrafast carrier dynamics in Sec. 2.2.5. Finally, a numerical procedure to calculate the field-phase-sensitive ionization rate is presented in Sec. 2.2.6.

2.2.1 Strong-field ionization

When a solid with a bandgap $E_g > 0$ is exposed to electromagnetic radiation of frequency ω_0 such that $\hbar\omega_0 \geq E_g$, a one-photon-absorption process occurs. Every absorbed photon excites one electron from a bound state in the valence band to an excited state in the conduction band, while a positively charged hole remains in the valence band.

If the energy of one photon is smaller than the energy gap between the valence and the conduction band of the material ($E_{\mathrm{ph}} < E_g$), one-photon absorption is no longer possible since it would lead to energy states in the forbidden region between valence and conduction band. Considering a laser wavelength of $\lambda = 800\,\mathrm{nm}$ and a bandgap of $E_g = 7.5\,\mathrm{eV}$ for fused silica, the energy of one photon ($\approx 1.55\,\mathrm{eV}$) is not sufficient to overcome the energy gap between valence and conduction band. However, if the intensity of the applied field is high enough it is still possible to promote electrons from valence to conduction band states by the simultaneous absorption of multiple photons. The strong-field induced generation of quasi-free carriers may then cause strong absorption of the incident field in the irradiated material even though the target is initially transparent to the incoming laser wavelength. Two extreme limits of SFI are commonly described in the literature. In the high frequency, low intensity limit multiphoton ionization (MPI) dominates the plasma formation due to SFI. Conversely, in the low frequency, high intensity limit electrons are primarily excited by tunneling ionization (TI).

Multiphoton Ionization If the energy of one photon from the laser field is not sufficient to transfer one electron into an excited state it is possible that a certain number of photons, whose total energy exceeds the bandgap energy, is absorbed quasi-simultaneously. Let N be the minimal number of photons needed to bridge the bandgap. Then the following condition results:

$$N\hbar\omega_0 \geq E_g. \tag{2.2.1}$$

The process of multiphoton ionization is depicted in Fig. 2.2.1(a). An ultrashort laser pulse interacts with a valence electron. The simultaneous absorption of several photons (indicated by the vertical arrows) energetically excites the electron to the conduction band while a hole is left behind in the valence band. Since the number of photons involved in the MPI process is given by the number N, the influence of MPI on the density of quasi-free electrons in the conduction band ρ is approximately proportional to the N-th power of the intensity of the incident laser field $I(t)$ [28]:

$$\left(\frac{\partial \rho(t)}{\partial t}\right)_{\mathrm{MPI}} \approx \sigma_N I(t)^N. \tag{2.2.2}$$

Here σ_N describes the absorption cross-section for an N-photon absorption. The associated MPI rate decreases strongly with increasing N. The smaller ionization rate for bigger N can be traced back to the probability for the presence of N photons close to the respective atom at a certain time. Figure 2.2.1(b) shows the number of necessary photons - the multiphoton order N - as a function of the excitation wavelength for three different bandgap values. Naturally, for a smaller bandgap or a shorter wavelength, fewer photons are needed. Hence, the larger the bandgap and the longer the excitation wavelength, the higher the nonlinearity of the MPI process. Based on the fact that only an integer number of photons can

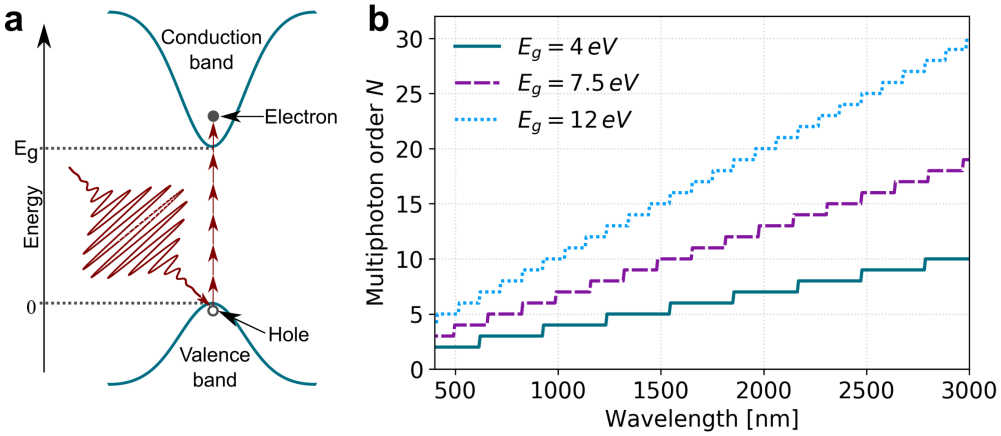

Fig. 2.2.1: **a**. Schematic of Multiphoton Ionization. An intense ultrashort laser pulse interacts with an electron in a bound state. It provides the energy of N photons whose total energy exceeds the bandgap of the irradiated material and results in the excitation of the electron to the conduction band. **b**. Multiphoton order N as a function of the excitation wavelength for different values of the bandgap E_g.

be involved in the ionization process, discrete multiphoton order levels form over a certain range of excitation wavelengths. As can be seen in Fig. 2.2.1(b) these ranges get broader for a smaller value of the bandgap. Experimental evidence for MPI in solid materials has been provided e.g. by wavelength-dependent studies of the laser-induced damage threshold of thin films [22, 52] or the observation of nonlinear absorption due to MPI seeded by self-trapped excitons [53].

Tunneling Ionization During the laser irradiation, the presence of a strong electromagnetic field in the target material results in a distortion of the atomic potential. When the electric field of the laser pulse exceeds a critical value, electrons are promoted from the valence to the conduction band with a significant probability. The migration of the carriers into the conduction band can then also proceed by quantum mechanical tunneling across the distorted Coulomb potential (see Fig. 2.2.2). A large variety of models exist in the literature to simulate tunneling ionization probabilities in atoms, molecules and solids (see e.g. [54–57]). Due to the availability of laser sources providing ever shorter pulses and the birth of attosecond physics, the majority of recent theoretical studies is focused on sub-cycle ionization dynamics resolving excitation dynamics on the attosecond timescale (see e.g. [58–62]). While several compelling experimental studies have proven the sub-cycle nature of tunneling ionization in gases and solids [23, 25, 26, 63, 64] the time it takes for an electron to tunnel through the potential barrier still constitutes an active field of research. Attoclock measurements of tunneling times performed in gases and their interpretations remain a subject of intense discussion [65–68]. Recently, an all-optical method to determine the

tunneling time in solid state systems based on the detection of the zero-order Brunel harmonic[1] has been proposed [69].

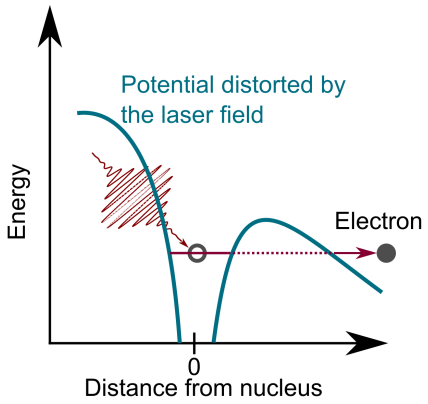

Fig. 2.2.2: Schematic of Tunneling Ionization. The electric field of the laser distorts the Coulomb potential that binds the electron to the atomic core and enables tunneling of an electron through the potential barrier.

The unifying Keldysh Theory In 1965 L. V. Keldysh published a seminal paper on the interaction of near-infrared (NIR) laser fields with matter describing both gases and solids within a unifying theory [55]. He identified the previously described mechanisms of MPI and TI as two extreme limits of the same process - SFI. To distinguish between the two different extreme domains (pure MPI, pure TI) the adiabatic Keldysh parameter γ was introduced as [70]:

$$\begin{aligned} \gamma &= \sqrt{\frac{E_g}{2U_p}} \\ &= \frac{\omega_0}{e}\left(\frac{m^* c n_0 \epsilon_0 E_g}{2I}\right)^{1/2}. \end{aligned} \tag{2.2.3}$$

Here, the ponderomotive energy $U_p = (E_0^2 e^2)/(4\omega_0^2 m^*)$ was used. I denotes the intensity of the laser field. For values $\gamma \gg 1$ MPI dominates while for $\gamma \ll 1$ TI becomes the prevailing ionization mechanism.
The Keldysh-parameter γ as a function of the laser intensity is displayed in Fig. 2.2.3(a) for three different wavelengths together with the regions of dominating MPI and TI separated by the dashed line at $\gamma = 1$. Since the majority of the phenomena based on SFI occurs within the intermediate regime where $\gamma \approx 1$, a pure multiphoton or tunneling approximation is not sufficient to model the corresponding experiments. Figure 2.2.3(b) shows the time dependence of the Keldysh-parameter resulting from an incident pulse with a central wavelength of

[1] for a detailed discussion of Brunel harmonics see Sec. 3.4

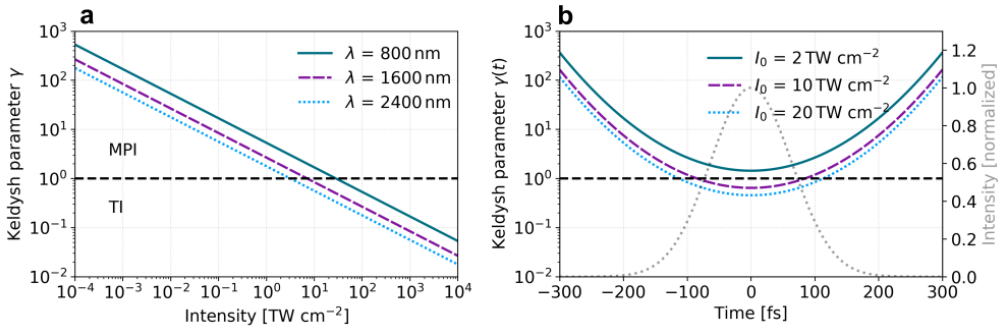

Fig. 2.2.3: Numerical simulation of the Keldysh parameter γ according to Eq. 2.2.3 in SiO_2 (Material parameters are given in Tab. 2.1.1). **a**. Keldysh parameter γ as a function of the peak intensity of the laser field for different excitation wavelengths. **b**. Time dependence of the Keldysh parameter for three different peak intensities of a λ=2100 nm wavelength driving field with a FWHM pulse duration of 150 fs.

2100 nm, a FWHM pulse duration of 150 fs and three different peak intensities in fused silica. For a peak intensity of 2 TW cm^{-2} the resulting Keldysh-parameter constantly stays in the multiphoton domain while for peak intensities of 10 and 20 TW cm^{-2} it enters the tunneling regime around the peak of the pulse.
The total SFI rate, containing both, MPI and TI is given by [55]

$$W_{\mathrm{SFI}} = \frac{2\omega_0}{9\pi}\left(\frac{\omega_0 m^*}{\hbar\sqrt{\Gamma}}\right)^{3/2} Q(\gamma, x)\exp\left\{-\pi\frac{K(\sqrt{\Gamma})-E(\sqrt{\Gamma})}{E(\sqrt{\zeta})}]x+1[\right\}. \quad (2.2.4)$$

Here, $Q(\gamma, x)$ describes the infinite sum

$$Q(\gamma, x) = \sqrt{\frac{\pi}{2K(\sqrt{\zeta})}}\sum_{n=0}^{\infty}\left(\exp\left\{-n\pi\frac{K(\sqrt{\Gamma})-E(\sqrt{\Gamma})}{E(\sqrt{\zeta})}\right\}\Phi(\sqrt{\eta(n+2\mu)})\right). \quad (2.2.5)$$

Further abbreviations read:

$$\Gamma = \frac{\gamma^2}{\gamma^2+1}, \quad \zeta = \frac{1}{\gamma^2+1}, \quad \eta = \frac{\pi^2}{2K(\sqrt{\zeta})E(\sqrt{\zeta})},$$
$$x = \frac{2}{\pi}\frac{E_g}{\hbar\omega_0}\frac{1}{\sqrt{\Gamma}}E(\sqrt{\zeta}), \qquad \mu =]x+1[-x. \quad (2.2.6)$$

$K(k)$ and $E(k)$ are the elliptical integrals of first and second kind

$$\begin{aligned} K(k) &= \int_0^{\pi/2} \frac{1}{\sqrt{1-k^2\sin^2(\phi)}} d\phi, \\ E(k) &= \int_0^{\pi/2} \sqrt{1-k^2\sin^2(\phi)} d\phi, \end{aligned} \tag{2.2.7}$$

$]y[$ denotes the integer part of y and $\Phi(u)$ is the Dawson-function:

$$\Phi(u) = \int_0^u e^{y^2-u^2} dy. \tag{2.2.8}$$

Furthermore, Keldysh provides approximation formulas for the limiting cases of pure MPI and pure TI. The ionization rate for an intensity region completely dominated by TI reads:

$$W_{\mathrm{TI}} = \frac{2E_g}{9\pi^2\hbar}\left(\frac{m^* E_g}{\hbar^2}\right)^{3/2}\left(\frac{\hbar\omega_0}{\gamma E_g}\right)^{5/2} \exp\left(-\frac{\pi\gamma E_g}{2\hbar\omega_0}\left\{1-\frac{1}{8}\gamma^2\right\}\right). \tag{2.2.9}$$

For the opposite case of MPI governing the excitation process of the material the approximation given by Keldysh is

$$W_{\mathrm{MPI}} = \frac{2\omega_0}{9\pi}\left(\frac{\omega_0 m^*}{\hbar}\right)^{3/2} (4\gamma)^{-2k} \Phi\left(\sqrt{2\left\{k-\frac{\Delta}{\hbar\omega_0}\right\}}\right) \exp\left(2k\left\{1-\frac{1}{4\gamma^2}\right\}\right), \tag{2.2.10}$$

with effective bandgap Δ and effective multiphoton order k defined by

$$k = \left]1+\frac{\Delta}{\hbar\omega_0}\right[\qquad \text{and} \qquad \Delta = E_g\left(1+\frac{1}{2\gamma^2}\right). \tag{2.2.11}$$

A comparison of the approximations for dominating TI and MPI to the full rate according to Eq. 2.2.4 is given in Fig. 2.2.4. As expected, the total SFI rate is well approximated by the solution of Eq. 2.2.10 at low laser intensities while the tunneling approximation coincides with the SFI rate at high laser intensities where TI becomes the prevailing excitation mechanism. Numerical results for the total SFI rate according to Eq. 2.2.4 are given in Fig. 2.2.5. The intensity dependence of W_{PI} for three different wavelengths in fused silica (parameters taken from Tab. 2.1.1) is shown in Fig. 2.2.5(a) indicating strongly diverging ionization rates for the different wavelengths in the low intensity range (MPI-domain). Conversely in the high intensity range where TI becomes the prevailing SFI mechanism, the rates converge towards a constant rate. The discontinuities that are well pronounced in the low intensity region are the result of multiphoton order transitions already discussed in the previous section on MPI [see e.g. Fig. 2.2.1(b)]. These multiphoton order transitions vanish in the tunneling regime. This behavior is reproduced by Fig. 2.2.5(b), where the

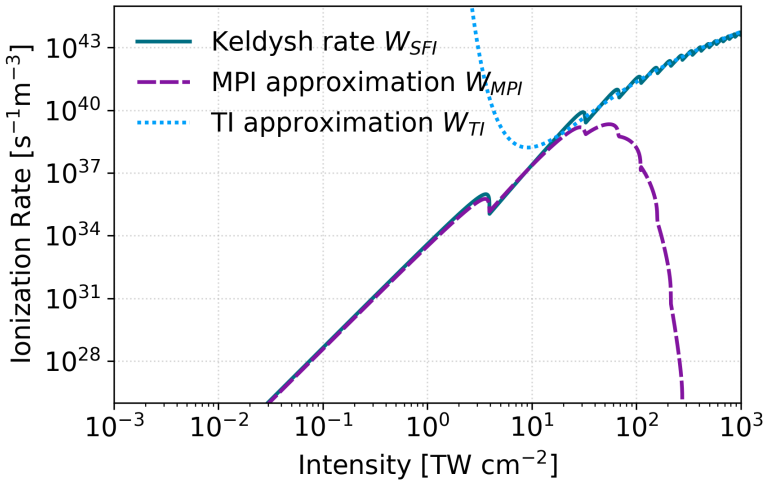

Fig. 2.2.4: Comparison of the MPI (Eq. 2.2.10) and the TI (Eq. 2.2.9) approximations to the total SFI rate (Eq. 2.2.4) for fused silica (parameters taken from Tab. 2.1.1) and a laser wavelength of 800 nm.

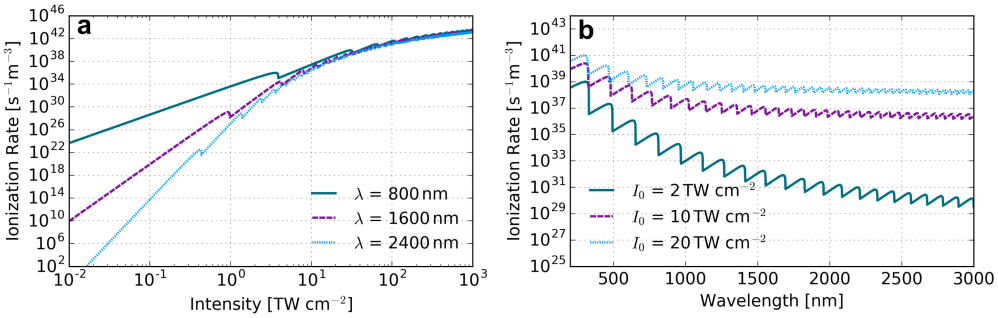

Fig. 2.2.5: **a**. Keldysh ionization rate as a function of the laser intensity for three different excitation wavelengths. **b**. Keldysh ionization rate depending on the excitation wavelength for three different peak intensities in a-SiO_2.

SFI rate is shown for different peak intensities as a function of the excitation wavelength. Here the MPI order transitions tend to display a weaker signature for longer driving wavelengths. Since for longer driving wavelengths the Keldysh parameter γ is generally smaller as shown in Fig. 2.2.3 TI starts to dominate over MPI already at smaller peak intensities. Figure 2.2.6 displays the intensity and

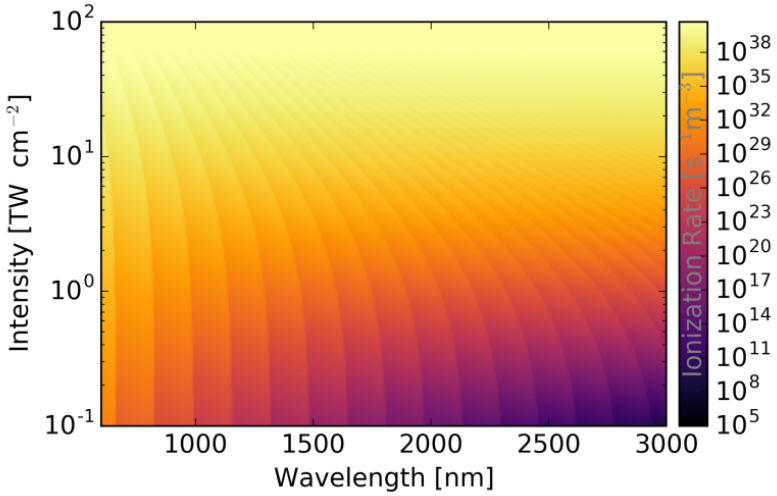

Fig. 2.2.6: SFI rate as a function of laser intensity and excitation wavelength in fused silica.

wavelength dependence of the SFI rate in a two-dimensional representation. The strong wavelength dependence of the Keldysh rate associated with MPI (MPI order transitions) vanishes in the high intensity, long wavelength regime.
In conclusion, TI tends to dominate over MPI in the mid-infrared (MIR) spectral region according to the Keldysh theory. One major drawback of using the ionization rate according to Keldysh is the monochromatic, cycle-averaged form of the equations. Hence, the Keldysh theory is not capable of describing sub-cycle features in the ionization dynamics. Therefore, a field-phase-sensitive version of the Keldysh ionization theory is added in Sec. 2.2.6. Furthermore, due to the monochromatic character of the Keldysh rate it is not well-suited to describe the excitation of solids induced by broadband few-cycle laser fields. Thus, several strategies for SFI models accounting for the polychromatic nature of few-cycle pulses have been developed [12, 71–73].

2.2.2 Electron-impact ionization

The second major excitation process contributing to the formation of the electron-hole plasma in solid dielectrics exposed to intense, ultrafast laser radiation is electron-impact ionization (IMP). In contrast to SFI the generation of quasi-free carriers due to IMP requires seed electrons already present in the conduction

band. If an electron is promoted to the conduction band (e.g. by SFI) this electron can gain further energy by the absorption of photons from the laser field. As a result of this process - commonly referred to as inverse bremsstrahlung - the electron is excited to higher lying states within the conduction band. One-photon absorption events might repeat until a critical energy level E_{crit} (see Eq. 2.2.20) is reached. The excited electron can then relax energetically to the conduction band edge while at the same time exciting a further electron from the valence to the conduction band by collisional ionization. This process, depicted in Fig. 2.2.7, can be repeated numerous times and since the number of available seed carriers doubles in every iteration IMP can potentially lead to an avalanche effect. Due to the exponential growth of the conduction band electron density IMP is often called avalanche ionization.

To analyze electron-impact ionization quantitatively, numerous models exist in

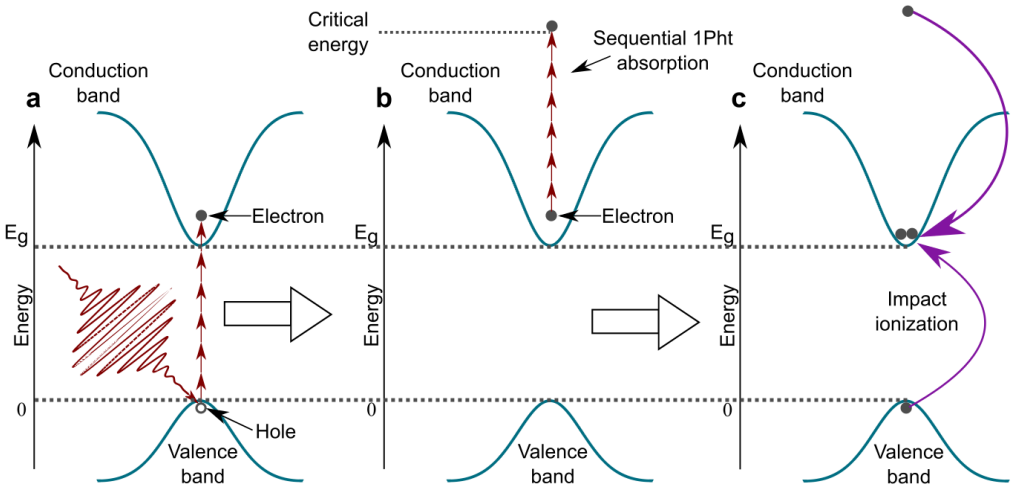

Fig. 2.2.7: Scheme of electron-impact ionization. **a**. Generation of seed electron population by MPI. **b**. Sequential single-photon absorption of the conduction band electrons until reaching a critical energy. **c**. Excitation of a further electron from the valence to the conduction band by an electron-electron collision.

the literature (see e.g. [74–77]). The most commonly used description is based on the Drude-Model [78, 79], initially developed to describe conduction phenomena in metals. However, it has been shown that it is suited to also describe electron dynamics in the conduction band of dielectric materials. The model is based on the solution of the one-dimensional equation of motion for a free electron in an oscillating electromagnetic field given by [80]:

$$m^* \frac{\partial^2 z}{\partial t^2} + \frac{m^*}{\tau_c} \frac{\partial z}{\partial t} = -eE_0 \exp(-i\omega_0 t), \tag{2.2.12}$$

with the characteristic collision time τ_c and the amplitude of the electric field E_0. z describes the displacement of the electron with respect to its initial position. Solving this differential equation yields the time-dependent position of the electron $z(t)$

$$z(t) = \frac{e}{m^*} \frac{1}{\omega_0(\omega_0 + i/\tau_c)} E_0 \exp(-i\omega_0 t). \tag{2.2.13}$$

Moving the excited electrons away from their initial position and away from the positively charged ionic cores creates a macroscopic polarization $P_{\text{fe}}(t)$ that is proportional to the displacement of the free carriers z, their density ρ and the elementary charge ($P_{\text{fe}}(t) = -z(t)\rho(t)e$). Thus, the resulting polarization generated by the conduction band electrons reads

$$P_{\text{fe}}(t) = -\frac{e^2}{m^*} \frac{\rho(t)}{\omega_0(\omega_0 + i/\tau_c)} E_0 \exp(-i\omega_0 t). \tag{2.2.14}$$

Furthermore the free electron contribution to the total susceptibility follows from the relation $P = \epsilon_0 \chi E$ to

$$\begin{aligned} \chi_{\text{fe}}(\omega) &= \frac{P_{\text{fe}}}{\epsilon_0 E} \\ &= -\frac{e^2}{\epsilon_0 m^*} \frac{\rho}{\omega_0(\omega_0 + i/\tau_c)}. \end{aligned} \tag{2.2.15}$$

In order to obtain an expression for the total dielectric function $\epsilon(\omega)$ the sum of the free - ϵ_{fe} - and the bound electron contribution - ϵ_{be} - has to be considered.

$$\begin{aligned} \epsilon(\omega) &= 1 + \chi_{\text{be}}(\omega) + \chi_{\text{fe}}(\omega) \\ &= \epsilon_{\text{be}}(\omega) + \chi_{\text{fe}}(\omega) \\ &= \epsilon_{\text{be}}(\omega) \left(1 - \frac{\rho e^2}{\epsilon_0 \epsilon_{\text{be}} m^*} \frac{1}{\omega_0(\omega_0 + i/\tau_c)}\right) \\ &= \epsilon_{\text{be}}(\omega) \left(1 - \omega_p^2 \tau_c^2 \frac{1 - i/\omega\tau_c}{1 + \omega_0^2 \tau_c^2}\right). \end{aligned} \tag{2.2.16}$$

In the last step the plasma frequency

$$\omega_p = \sqrt{\frac{\rho e^2}{\epsilon_0 \epsilon_{\text{be}} m^*}}, \tag{2.2.17}$$

was inserted. Splitting the above expression into its real and imaginary component gives

$$\begin{aligned}\Re(\epsilon(\omega)) &= \epsilon_{\mathrm{be}}(\omega)\left(1-\frac{\omega_p^2}{\omega_0^2}\frac{\omega_0^2\tau_c^2}{1+\omega_0^2\tau_c^2}\right),\\ \Im(\epsilon(\omega)) &= \epsilon_{\mathrm{be}}(\omega)\left(\frac{\omega_p^2}{\omega_0^2}\frac{\omega_0\tau_c}{1+\omega_0^2\tau_c^2}\right).\end{aligned} \tag{2.2.18}$$

The imaginary part leads to the absorption of incident electromagnetic radiation, accelerating the conduction band electrons. This inverse bremsstrahlung [81] is a necessary condition for subsequent interband excitation of electrons from the valence band by electron-electron collisions. Since absorption is generally directly related to the complex part of the refractive index, the real (n_{fe}) and imaginary (κ_{fe}) components of the total refractive index $n = n_{\mathrm{be}} + n_{\mathrm{fe}} + i\kappa_{\mathrm{fe}} = \sqrt{\epsilon}$ need to be computed. Assuming $n^2 \approx n_{\mathrm{be}}^2 + 2n_{\mathrm{be}}n_{\mathrm{fe}} + i2n_{\mathrm{be}}\kappa_{\mathrm{fe}}$ it follows:

$$\begin{aligned}n_{\mathrm{fe}}(\omega) &= \frac{-n_{\mathrm{be}}(\omega)}{2}\frac{\omega_p^2\tau_c^2}{\omega_0^2\tau_c^2+1},\\ \kappa_{\mathrm{fe}}(\omega) &= \frac{n_{\mathrm{be}}(\omega)}{2}\frac{\omega_p^2\tau_c}{\omega_0(\omega_0^2\tau_c^2+1)}.\end{aligned} \tag{2.2.19}$$

To ionize a further electron from the valence band by collisional ionization the already excited electron needs to gain at least the amount of energy that matches the potential barrier of the bound electron. In this work the effective bandgap $\Delta(t)$ (see Eq. 2.2.11) is employed as a critical energy:

$$\Delta(t) = E_{\mathrm{crit}}(t) = E_g\left[1+\left(\frac{1}{2\gamma(t)^2}\right)\right], \tag{2.2.20}$$

with Keldysh-parameter $\gamma(t)$. Analyzing Eq. 2.2.20 by inserting Eq. 2.2.3 reveals that the above expression can be rewritten as the sum of the intrinsic material bandgap and the ponderomotive quiver energy:

$$\begin{aligned}\Delta &= E_g\left(1+\frac{2U_p}{2E_g}\right)\\ &= E_g + U_p\end{aligned} \tag{2.2.21}$$

A second commonly used definition of the critical energy [82, 83] given by

$$\mathcal{E} = \frac{1+2\mu}{1+\mu}(E_g + U_p), \tag{2.2.22}$$

only differs in the prefactor. Here, $\mu = m^*/m_{\mathrm{VB}}^*$ where m_{VB}^* denotes the effective valence band electron mass. Assuming the same masses for electrons in the

valence and conduction band the only difference that remains between the two concepts is a prefactor of 3/2. Generally, it is worth mentioning that the majority of the existing models to compute the critical energy oversimplify the actual situation. In order to not only account for the conservation of energy but also for the conservation of momentum in the description of IMP the dispersion of the energy bands in solid crystals has to be considered. Hence, the energy gap between the valence and the conduction band that has to be bridged in collisional ionization is generally much larger than the initial gap for the direct transition induced by SFI. However, in the case of oxide glasses the given approximation is acceptable since the effective valence electron mass is much bigger than the effective mass of conduction band electrons. Hence, the valence band can be considered as being flat compared to the conduction band.
The ionization probability induced by electron-impact ionization thus follows as

$$\begin{aligned}\left(\frac{\partial\rho(t)}{\partial t}\right)_{\mathrm{IMP}} &= -\frac{\partial_z I(t)}{\partial z}\\ \left(\frac{\partial\rho(t)}{\partial t}\right)_{\mathrm{IMP}} E_{\mathrm{crit}}(t) &= -\frac{2\omega_0\kappa_{\mathrm{fe}}}{c} I(t)\\ \left(\frac{\partial\rho(t)}{\partial t}\right)_{\mathrm{IMP}} &= \frac{1}{cE_{\mathrm{crit}}(t)}\frac{n_{\mathrm{be}}(\omega_0)\omega_p^2\tau_c}{\tau_c^2\omega_0^2+1} I(t) \equiv \frac{\sigma_{\mathrm{IMP}}}{E_{\mathrm{crit}}(t)}\rho(t)I(t).\end{aligned} \tag{2.2.23}$$

The electron-impact ionization cross-section σ_{IMP} is given by [31]:

$$\sigma_{\mathrm{IMP}} = \frac{e^2}{n_{\mathrm{be}}(\omega_0)m^* c\epsilon_0}\frac{\tau_c}{1+\omega_0^2\tau_c^2}. \tag{2.2.24}$$

As an alternative model for electron-impact ionization the Multiple-Rate-Equation (MRE) Model developed by Rethfeld [77] recently gained prominence [52, 84, 85]. Within the MRE model the excited states within the conduction bands are discretized. The excitation of electrons in the conduction band happens by sequential single-photon absorption until the absorbed energy exceeds the critical energy E_{crit}. When the excited electron relaxes back to the conduction band edge it ionizes a further electron from the valence band only with a certain probability ($p \leq 1$). The main difference between the Drude and the MRE model thus lies in the consideration of the sequential one-photon absorption by a linear system of differential equations leading to discrete energy levels in the conduction band.

A numerical analysis of the dependence of the impact ionization cross-section σ_{IMP} on the collision time τ_c is displayed in Fig. 2.2.8(a). A strong dependence of the IMP cross-section on τ_c with a clear single peak at a particular value of the collision time (around ≈ 1 fs) can be observed independent on the excitation wavelength. The extracted collision time at which the ionization cross-section peaks is shown in Fig. 2.2.8(b) as a function of the laser wavelength. The two-dimensional representation of the collision time and wavelength dependence of the IMP cross-section (see Fig. 2.2.9) points out the monotonous increase for an

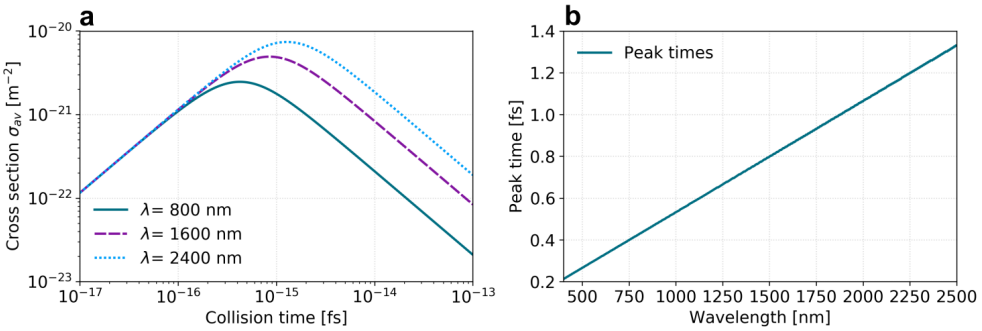

Fig. 2.2.8: Numerical results on electron-impact ionization. **a**. Electron-impact ionization cross-section according to Eq. 2.2.24 as a function of the electron-electron collision time for three different excitation wavelengths in SiO_2 (parameters taken from Tab. 2.1.1). **b**. Extracted collision time that maximizes σ_{IMP} as a function of the laser wavelength.

increasing excitation wavelength together with the already discussed structure of the collision time dependence. Based on these observations it becomes apparent that the choice of the collision time in the IMP cross-section plays a crucial role for modeling the ionization of solid dielectrics. Therefore, a numerical model for a variable collision time will be introduced in the following section.

Collision Time As shown in the previous section, the generation of quasi-free carriers by IMP depends critically on the value of the collision time (see Fig. 2.2.8). Usually a fixed value for the electron-electron collision time τ_c is used for numerical simulations of plasma formation in solid dielectrics [46, 49, 83, 86–96]. However, the usage of a fixed collision time that does not depend on parameters such as the actual carrier density in the conduction band is rather counterintuitive. While Christensen et al. [84] employed a model based on a classical gas collision rate, a Debye-screened electron-electron collision rate is calculated in Refs. [97, 98]. In what follows, an alternative model developed by Tikhonravov and Starke [22] is used. This model is based on the average velocity of an electron $\langle v \rangle$ and the cross-section for an electron-atom collision σ_c. The average electron velocity can be approximated from the kinetic energy via

$$\langle v \rangle = \sqrt{2E_{\mathrm{kin}}/m^*}. \tag{2.2.25}$$

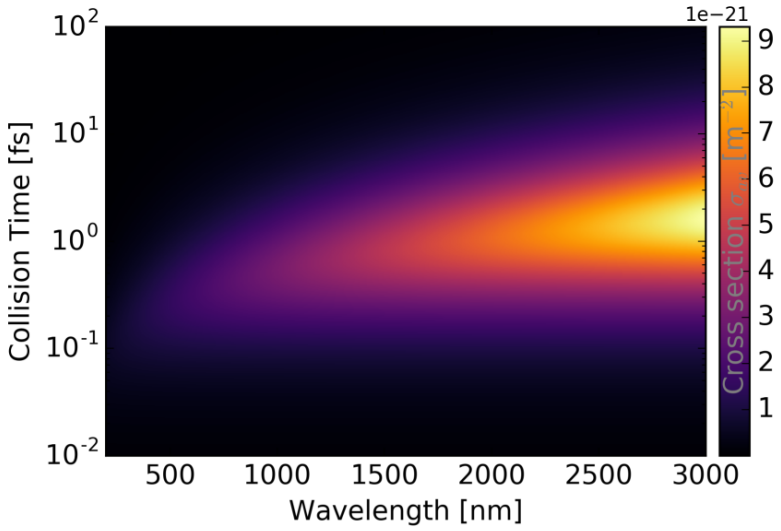

Fig. 2.2.9: Impact ionization cross-section σ_{IMP} according to Eq. 2.2.24, as a function of the collision time τ_c and the excitation wavelength in fused silica.

The cross-section σ_c then follows from the ion radius R_{ion} that can be approximated by equating the coulombic energy and the kinetic energy:

$$\begin{aligned} E_{\mathrm{kin}} = \frac{1}{4\pi\epsilon_0}\frac{e^2}{R_{\mathrm{ion}}} \quad &\Rightarrow \quad R_{\mathrm{ion}}^2 = \left(\frac{1}{4\pi\epsilon_0}\frac{e^2}{E_{\mathrm{kin}}}\right)^2 \\ &\Rightarrow \quad \sigma_c = \pi R_{\mathrm{ion}}^2 = \frac{1}{16\pi\epsilon_0^2}\frac{e^4}{E_{\mathrm{kin}}^2} \end{aligned} \tag{2.2.26}$$

Approximating the collision rate τ_c^{-1} by the average rate for an electron to enter the volume of the ion yields:

$$\begin{aligned} \tau_c^{-1} &= \rho\langle v\sigma_c\rangle \approx \rho\langle v\rangle\langle\sigma_c\rangle \\ &= \rho\sqrt{\frac{2E_{\mathrm{kin}}}{m^*}}\frac{1}{16\pi\epsilon_0^2}\frac{e^4}{E_{\mathrm{kin}}^2} \\ &= \rho\sqrt{\frac{2}{m^* E_{\mathrm{kin}}^3}}\frac{e^4}{16\pi\epsilon_0^2}. \end{aligned} \tag{2.2.27}$$

Thus, the collision time reads

$$\tau_c = \frac{16\pi\epsilon_0^2}{\rho e^4}\sqrt{\frac{E_{\mathrm{kin}}^3 m^*}{2}}. \tag{2.2.28}$$

The average kinetic energy of the electrons can be approximated by $E_{\text{kin}} =$

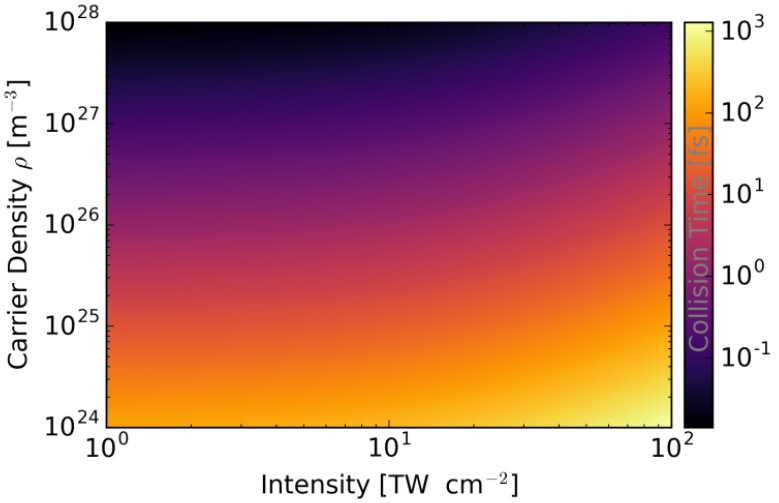

Fig. 2.2.10: Collision time τ_c as a function of the density of conduction band electrons ρ and the peak intensity of the incident field ($\lambda = 1600\,\text{nm}$) obtained by Eq. 2.2.28 for the case of fused silica (simulation parameters taken from Tab. 2.1.1).

$0.1\,E_{\text{crit}}$ and is thereby correlated to the bandgap of the material [22]. The resulting collision time as a function of the carrier density ρ and the laser peak intensity is presented in Fig. 2.2.10. The numerical results illustrate how an increased plasma density reduces the resulting collision time while for a fixed carrier density an increase of the intensity leads to an increase of the collision time due to the ponderomotive shift of the bandgap energy implicitly included in E_{kin}.
In summary, the Drude-Model for electron-impact ionization provides a theoretical description, that, besides well-known physical constants, uses intrinsic material parameters that are hard to access experimentally. It is noteworthy that the Drude-model commonly overestimates the actual ionization probability since it is assumed that every electron that reaches the critical energy ionizes a further electron from the valence band. The model includes no alternative way to dispense the electronic energy by e.g. collisions with the lattice or further loss mechanisms.

2.2.3 The optical properties of a plasma

Above a certain laser intensity, bound electrons may be injected into the conduction band to form an electron-hole plasma. The presence of quasi-free electrons in the conduction band of the irradiated target results in an alteration of the local

polarization and therefore the local dielectric constant. This section discusses how the modified dielectric function affects the optical properties of a laser-excited solid dielectrics.

Plasma defocusing The modified dielectric function accounting for the influence of quasi-free electrons was already derived in Sec. 2.2.2. The contribution of the electron-hole plasma to the real part of the total refractive index was given in Eq. 2.2.19 as

$$\begin{aligned} n_{\mathrm{fe}}(\omega) &= \frac{-n_{\mathrm{be}}(\omega)}{2} \frac{\omega_p^2 \tau_c^2}{\omega_0(\omega_0^2 \tau_c^2 + 1)} \\ &= \frac{-\rho e^2 \tau_c^2}{2\epsilon_0 n_0 m^* (\omega_0^2 \tau_c^2 + 1)}. \end{aligned} \tag{2.2.29}$$

Here, Eq. 2.2.17 was inserted. Combining Eqns. 2.1.14 and 2.2.29 yields the variation of the real part of the index of refraction induced by the optical Kerr-effect and the electron-hole plasma:

$$n_0 \Delta n = n_0 n_2 I - \frac{\rho e^2 \tau_c^2}{2\epsilon_0 m^* (\omega_0^2 \tau_c^2 + 1)}. \tag{2.2.30}$$

Equation 2.2.30 shows that the optical Kerr-effect increases the index of refraction (for a positive n_2) while the plasma contribution decreases the effective refractive index. As discussed in Sec. 2.1.1 an increased refractive index leads to a focusing of the laser beam during propagation. In contrast, the quasi-free carriers in the conduction band lead to a defocusing of the propagating laser beam which is called plasma-defocusing. The defocusing of a laser beam due to the formation of an electron-hole plasma together with self-focusing leads to a complex interplay of the two counteracting propagation mechanisms. As a consequence, self-guiding effects caused by a repeated focusing due to the intensity-dependent refractive index and subsequent defocusing due to generated plasma density appear [99].

Ionization-induced blueshift The analogy between the intensity-dependent refractive index due to a third order nonlinearity of the material and the counteracting effect of the plasma can also be transferred to the effect of cross-phase modulation (see Sec. 2.1.2). A weak time-delayed probe laser field that propagates through a region where a strong pump laser field ionizes the material accumulates a phase shift due to the reduced index of refraction. Hence, it experiences a frequency shift with opposite sign compared to the self-phase modulation based on the optical Kerr-effect.
Assuming a homogeneous plasma density ρ that is much smaller than the critical density[2] the frequency shift of a monochromatic laser pulse due to the generation

[2] for a discussion of the critical plasma density see the following paragraph

of the plasma is given by

$$\Delta\omega = \frac{e^2 L}{2c\epsilon_0 m^* \omega} \frac{\partial \rho(t)}{\partial t}, \tag{2.2.31}$$

with finite interaction length L [100, 101].

Optical breakdown The laser-induced damage threshold (LIDT), being an important indicator for the resistance of optical components to optical damage, is often connected to the surpassing of a critical conduction band electron density. This critical plasma density is regularly approximated by a single value ($\rho_{\mathrm{crit}} \approx 10^{21}\,\mathrm{cm}^{-3}$ [49, 51]). Nevertheless, a more exact value can be derived from the dielectric function associated with the conduction band population as given in Eq. 2.2.18:

$$\begin{aligned} \Re(\epsilon(\omega)) &= \epsilon_{\mathrm{be}}(\omega)\left(1 - \frac{\omega_p^2}{\omega_0^2}\frac{\omega_0^2\tau_c^2}{1+\omega_0^2\tau_c^2}\right), \\ \Im(\epsilon(\omega)) &= \epsilon_{\mathrm{be}}(\omega)\left(\frac{\omega_p^2}{\omega_0^2}\frac{\omega_0\tau_c}{1+\omega_0^2\tau_c^2}\right). \end{aligned} \tag{2.2.32}$$

For large collision times ($\omega_0\tau_c \gg 0$) the imaginary part of the dielectric function can be neglected. Thus, the real part of the dielectric function reduces to:

$$\epsilon = \epsilon_{\mathrm{be}}\left(1 - \frac{\omega_p^2}{\omega_0^2}\right), \tag{2.2.33}$$

Once the plasma frequency reaches the value of the optical frequency ω_0 a so-called critical plasma is reached. The dielectric function is then zero. This leads to the definition of the critical plasma density

$$\rho_{\mathrm{crit}} = \frac{\epsilon_0 m^*}{e^2}\omega_0^2. \tag{2.2.34}$$

For fused silica (material parameters given in Tab. 2.1.1) and a typical wavelength for ultrafast lasers of $\lambda_0 = 800\,\mathrm{nm}$ this leads to a critical density of $1.1 \times 10^{21}\,\mathrm{cm}^{-3}$ which is slightly higher than the fixed value ($10^{21}\,\mathrm{cm}^{-3}$) but justifies the simplification of a fixed critical density at least for this particular wavelength. Nevertheless, Fig. 2.2.11 shows a clear deviation from this fixed value especially for smaller wavelengths. Here, it is worth mentioning that the critical plasma density that follows from equating the plasma frequency to the optical frequency of the excitation field is not a direct indicator for laser-induced damage. Rather, due to the significant absorption associated with a conduction band electron density comparable to ρ_{crit} the amount of energy coupled into the material leads to a permanent modification of the target. As a consequence, the presented

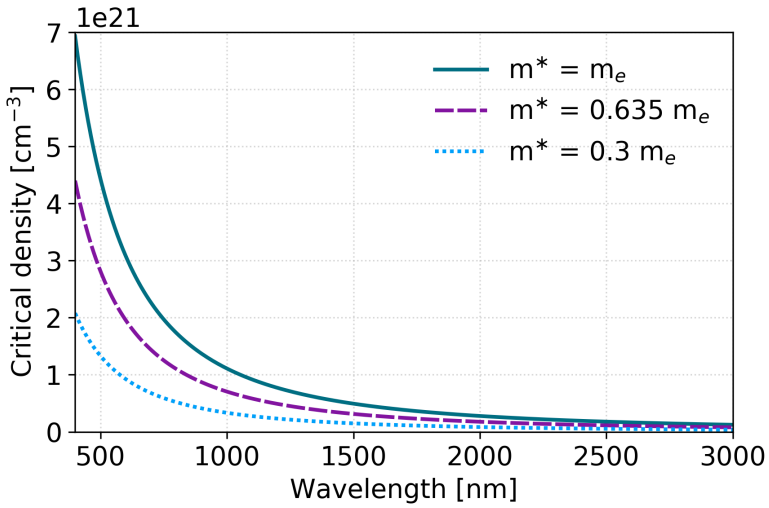

Fig. 2.2.11: Critical plasma density in fused silica according to Eq. 2.2.34 for different effective conduction band electron masses as a function of the laser wavelength (material parameters taken from Tab. 2.1.1).

damage criterion is not applicable in the case of few-cycle excitation pulses. Even if the density of free carriers generated by the few-cycle pulse reaches the critical density no subsequent absorption of the free carriers can occur simply because the laser pulse is too short. Therefore, alternative criteria have to be developed for few-cycle pulse laser-induced damage [12].

2.2.4 Ultrafast relaxation mechanisms of a laser-induced plasma

In the previous sections the energy coupling from the intense laser field to the material was analyzed. After transferring energy from the electromagnetic field into the electron-hole plasma the energy is redistributed inside the material, potentially leading to a modification of the solid target. In solid dielectrics the formation and subsequent relaxation of self-trapped excitons has been identified as an important relaxation channel of the electron-hole plasma besides radiative recombination and vibrational coupling [45, 47, 102]. An exciton consists of an optically-generated, weakly-bound, electron-hole pair. Since the energy associated with a localized exciton is smaller than that of a delocalized electron-hole pair, the exciton is localized on a particular position of the crystal lattice. Due to a stabilization of the quasiparticle caused by the localization, the resulting electron-hole pair is called a self-trapped exciton (STE). STEs are formed on an ultrafast timescale ($\approx 150\,\mathrm{fs}$ [45]). Hence, states in the initially forbidden region of the bandgap between valence and conduction band are created [see Fig. 2.2.12(a) & (b)]. Different microscopic mechanisms for the generation of STEs exist. If

a weakly bound electron-hole pair forms an exciton prior to self-trapping and then gets self-trapped, the resulting trapping rate shows no dependence on the present density of quasi-free carriers. Such a constant trapping rate has been observed in fused silica [47]. If electrons and holes exhibit different coupling strengths to the lattice, one of the carriers will be trapped first and subsequently recombine with the other carrier to form a STE. Experiments performed in NaCl have revealed a bi-molecular decay law as a result of this STE formation process [47]. Furthermore, STEs can be formed by direct resonant multiphoton absorption of valence band electrons to quasi-free states in the conduction band. After generation of a STE, the resulting quasiparticle is unstable with respect to recombination. In the case of wide bandgap dielectrics a localized trapping mechanism is more likely than a delocalized, scattering recombination [50]. Hence,

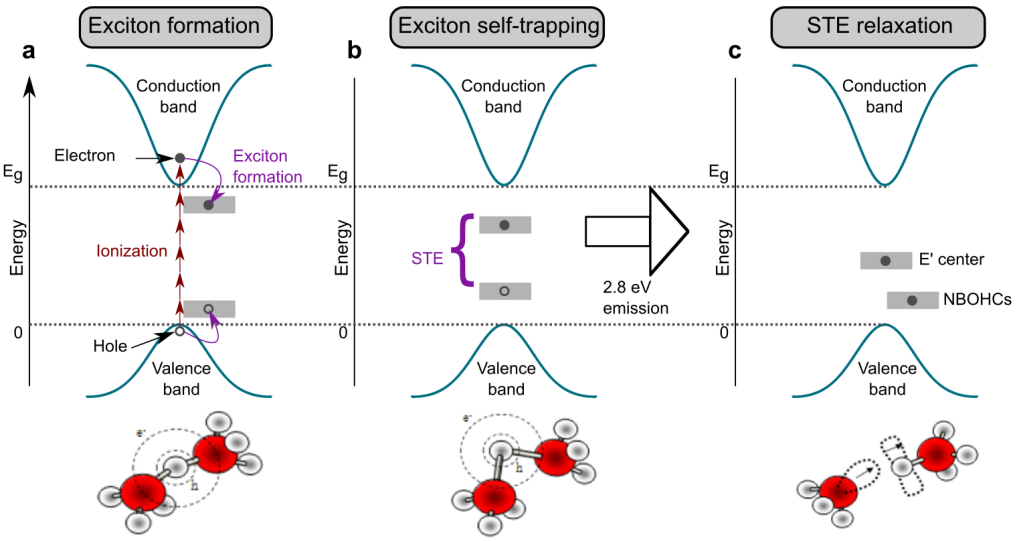

Fig. 2.2.12: Sketch of laser-induced defect formation in fused silica and the corresponding SiO_2 structure (adapted from [103]). **a**.Exciton formation after generation of an electron-hole pair. **b**. Exciton self-trapping. **c**. STE-relaxation and defect formation.

the energy that was coupled into the material by excitation of conduction band electrons is localized by the creation of STEs. In SiO_2 self-trapping of charge carriers leads to strong distortions of the crystal lattice [104]. Recombination of STEs leads to the emission of a characteristic luminescence signal. The energetic position of the STE level within the bandgap can thus be identified by time-resolved spectroscopy [105–107]. Experiments performed by Itoh et al. revealed two optical absorption bands at 4.2 and 5.2 eV and two luminescence bands at 2.5 and 2.8 eV in SiO_2 [108]. Due to the formation of energy levels in the bandgap STEs lead to a significantly stronger absorption of photons from an incident laser field, strongly contributing to cumulative effects.

Relaxation of the STEs leads to the formation of point defects, in fused silica mainly E-prime centers (oxygen vacancies) and non-bridging oxygen hole centers (NBOHCs) [109] [see Fig. 2.2.12(c), illustration of the fused silica structure adapted from [103]]. The formation of electronic defects resulting from the decay of STEs may lead to the formation of defect clusters. These defect clusters can potentially cause a macroscopic structural damage of the crystal lattice. Additionally, the increased volume associated with exciton self-trapping [50] can create a perturbation of the lattice by a shockwave, permanently modifying the structure of the crystal lattice.

For the implementation of free electron decay into self-trapped excitons in numerical simulations of plasma dynamics in solids usually a single relaxation term is implemented. The variation of the plasma density is approximated to be linearly dependent on the carrier density $\rho(t)$ with a proportionality factor $1/\tau_{\mathrm{rel}}$. The relaxation rate, counteracting SFI and IMP thus reads:

τ_{rel}	Reference
150 fs	Martin [47]
150 fs	Audebert [45]
220 fs	Mero [110]
50 fs	Pan [111]
179 fs	Grojo [53]
170 fs	Sun [91]

Table 2.2.1: Experimentally determined relaxation times in fused silica from time-resolved studies.

$$\left(\frac{\partial \rho(t)}{\partial t}\right)_{\mathrm{rel}} = -\frac{\rho(t)}{\tau_{\mathrm{rel}}}. \tag{2.2.35}$$

Table 2.2.1 summarizes relaxation times for fused silica that were experimentally obtained from time-resolved experiments. The wide range of the obtained values for the plasma decay time indicates that relaxation of an excited electron-hole plasma in fused silica strongly depends on the exact type of material used in the experiment. Furthermore, experimental parameters such as the laser wavelength, pulse duration and focusing conditions may influence the observed relaxation behavior.

2.2.5 Ultrafast carrier dynamics in solid dielectrics

After introducing the most relevant excitation and relaxation mechanisms for the interaction of solid dielectrics with ultrashort laser pulses (see Secs. 2.2.1 to

2.2.4) the different phenomena can be combined into a single rate equation (SRE) describing the dynamics of the conduction band population [51, 76, 112] by

$$\begin{aligned}\frac{\partial \rho(t)}{\partial t} &= W_{\mathrm{SFI}} + W_{\mathrm{IMP}} - W_{\mathrm{rel}} \\ &= W_{\mathrm{SFI}} + \frac{\sigma_{\mathrm{IMP}}}{E_{\mathrm{crit}}(t)}\rho(t)I(t) - \frac{\rho(t)}{\tau_{\mathrm{rel}}}.\end{aligned} \tag{2.2.36}$$

Here, W_{SFI} is the SFI rate introduced in Eq. 2.2.4 and W_{IMP} the ionization probability due to electron-impact ionization (see Eq. 2.2.23). Relaxation and self-trapping of the excited electrons are both accounted for in the single term W_{rel} as discussed in Sec. 2.2.4.
Since their first introduction the approximation of carrier dynamics in solids interacting with ultrashort laser pulses by employing a SRE has gained a lot of popularity due to the simplicity of its implementation. Numerical results based on the solution of this rate equation have provided excellent agreement with a wide variety of experimental studies (see e.g. [22, 52, 113–117]). Especially the modeling of ultrafast laser-induced damage and ablation thresholds of dielectric materials often relies on the solution of the given rate equation.
Nevertheless, the presented rate equation for the description of strong-field induced carrier dynamics constitutes a considerable simplification of the plasma dynamics in all its complexity. The complete neglect of the band structure of the irradiated solid results in a deficient description of both SFI and IMP especially for crystalline materials. Therefore, several extensions of the presented SRE include the band structure (or a simplified approximation of the band structure) into the calculation of the ionization probabilities (see e.g. [118, 119]). Furthermore, several extensions of the SRE accounting for the population of the laser-induced defect states and the ionization from these intergap states have been developed [47, 120–122].

2.2.6 Phase-sensitive Keldysh model

Due to the generation of ever shorter pulse durations down to the few and single-cycle limit [123–126] it is nowadays feasible to investigate the sub-cycle structure of ionization processes not only in gases [25, 63, 127] but also in solids [23, 26]. Furthermore, it is now possible to trace electron dynamics on their natural timescale [64, 128–132]. Hence, compelling theoretical and experimental work has been attributed to sub-cycle ionization dynamics in solids [23, 26, 59, 62, 133]. This was the main motivation for the implementation of a field-phase-sensitive ionization rate in our calculations, based on the traditionally cycle-averaged ionization rate developed by Keldysh (see Sec. 2.2.1).
The traditional Keldysh theory [55] as described in Sec. 2.2.1 only considers the cycle-averaged intensity of the ultrashort laser pulses incident on the material of interest. A wide variety of different approaches have been taken to develop

theories accurately describing ionization dynamics on sub-optical cycle timescales [58–62]. In this work a very generic ansatz, first proposed in [26] will be adapted to account for the sub-cycle nature of SFI.
The only correction that is made to the traditional Keldysh ionization rate (see Eq. 2.2.4) is the replacement of the cycle-averaged intensity, representing the envelope of the ultrashort pulse, by the instantaneous intensity. Due to the high nonlinearity of the SFI rate the ionization probability oscillates at twice the optical frequency of the driving field as shown in Fig. 2.2.13(a). At every minimum or maximum of the electric field the ionization probability increases in sharp peaks. This oscillatory behavior results in a significant difference of the integrated ionization over the total pulse compared to the traditional, cycle-averaged calculation. To account for this difference a single normalization constant $\mathcal{N}$ is added in front of the tunneling exponential of the Keldysh rate. $\mathcal{N}$ is chosen in way to minimize the difference between the integrated cycle-averaged and field-phase-sensitive ionization probabilities. Actual values that are used in the numerical simulation of the field-phase-sensitive ionization rate are shown in the inset in Fig. 2.2.13(b). Figure 2.2.13(b) shows a comparison between the

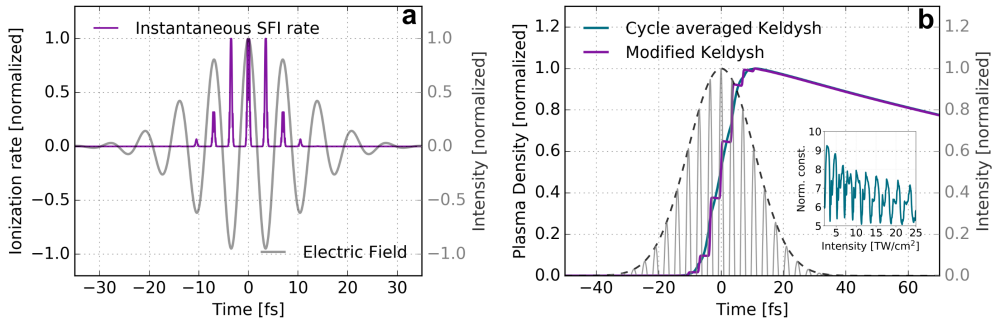

Fig. 2.2.13: Field-phase-sensitive calculations of SFI. **a**. Strong-field ionization rate computed by the modified Keldysh model together with the electric field of the excitation pulse. **b**. Resulting plasma density buildup displaying a nearly stepwise behavior compared to the result of a cycle-averaged calculation. Laser parameters: $\lambda = 2100\,\mathrm{nm}$, $\tau_p = 25\,\mathrm{fs}$, $I_0 = 14\,\mathrm{TW\,cm^{-2}}$. The inset shows numerical values of the normalization constant $\mathcal{N}$ as a function of the laser intensity.

dynamics of the plasma density obtained with the cycle averaged model and the modified phase-sensitive Keldysh model for a 25 fs pulse of 2100 nm central wavelength in fused silica (peak intensity $14\,\mathrm{TW\,cm^{-2}}$). The strong nonlinear dependence of the field-phase-sensitive SFI rate on the instantaneous intensity results in a nearly stepwise increase of the conduction band population twice per optical cycle.

Chapter 3

Harmonic generation in solids - state of the art

In the previous chapter strong-field driven interband transitions of electrons from valence states to quasi-free states in the conduction band have been discussed. In the following sections the mechanisms leading to the formation of high-order harmonics of the driving field in solid targets are reviewed and compared to the semi-classical model of harmonic generation in the gas phase.
High-order harmonic generation (HHG) in gases / atoms is commonly described within the framework of the well-accepted semi-classical three-step model [134–136]. Figure 3.0.1 depicts this model by sketching the three steps:

1. Ionization of an initially bound electron through the potential barrier by SFI.

2. Acceleration of the electron by the strong laser field.

3. Recollision of the accelerated electron with its parent ion, emitting a high energy photon with an energy that equals the gained kinetic energy plus the ionization potential of the atom.

Recollision-type HHG in gases has led to the generation of attosecond pulses [124, 137, 138] and the production of coherent radiation in the XUV spectral domain [139–141]. Based on these accomplishments time-resolved spectroscopy techniques have been developed enabling measurements with attosecond time resolution [63, 67, 127] and allowing real-time observation of electron dynamics.
As first proposed by Brunel in his seminal work [24] harmonics can already be produced by vertical transitions from the ground state to the continuum due to SFI near the peak of the electric field of the incident laser pulse (indicated by (1) in Fig.3.0.1). In contrast to harmonics generated by coherent recollision, the so-called Brunel harmonics do not exhibit a plateau-like behavior but instead the generation efficiency strongly decreases with increasing harmonic order. While

these ionization-induced harmonics do not allow the efficient generation of attosecond pulses, they provide very intimate insights into the sub-cycle structure of the strong-field ionization process as shown by pioneering experimental and theoretical work [25, 69, 142].
In condensed matter, nonlinear optical phenomena are often based on the nonlinear polarization associated with Kerr-type nonlinearities that are responsible for the generation of low-order, perturbative harmonics of the incident field [143]. Multiples of an intense electromagnetic field formed due to the nonlinearity of bound electrons are reviewed in 3.1.
Recently, HHG in solids has gained a lot of attention both theoretically [69, 144–182, 182–186] and experimentally [26, 187–224]. Although the underlying mechanisms and the relative role of the different HHG mechanisms are not fully understood on a microscopic level, HHG in solids opens up a promising route to investigate ultrafast nonlinear dynamics in solid targets. Furthermore, based on the higher density of solids compared to gases, solid state systems are considered as a serious candidate for the production of high photon flux, tabletop sources of coherent XUV radiation [207, 216, 221, 223, 225]. The main difference between atoms and solids regarding the HHG mechanisms results from the presence of a conduction band (or multiple conduction bands) in solids. Hence, the description of the laser-driven electrons in k-space differs from the atomic case. As discussed in this chapter, the shape of the conduction band can significantly influence the mechanism leading to HHG.
Figure 3.0.1 compares the mechanisms for HHG that are based on the presence of quasi-free electrons in the conduction band to the semiclassical three-step model for atomic HHG. The first process leading to the generation of harmonics in both, solids and gases, is SFI. Harmonics generated by the ionization step have been utilized to prove the existence of attosecond ionization bursts [25, 26, 226, 227]. Multiples of the driving field that are generated by the ionization step will be discussed in detail in Sec. 3.4.
While in the atomic picture excited electrons can be treated as free particles that are accelerated by the laser field, the quasi-free carriers in the case of a crystalline solid are accelerated within a given band structure (indicated by (2)). Due to the anharmonicity of the band structure in a solid the acceleration step is sufficient to produce harmonics of the incident field known as intraband harmonics. Intraband harmonics enable e.g. the direct reconstruction of the crystal band structure as shown in [198]. Generation of high-order harmonics due to the intraband acceleration of quasi-free carriers is described in Sec. 3.3.
Once the electric field changes sign the carriers are accelerated backwards and may recollide with their parent ion leading to the generation of photons with photon energies that are odd multiples of the photon energy of the driver laser (see (3)). Since during this process the initially excited electron energetically relaxes back to the valence band (ground state), this is known as the interband mechanism. This solid state analog of the recollision-type harmonics known from

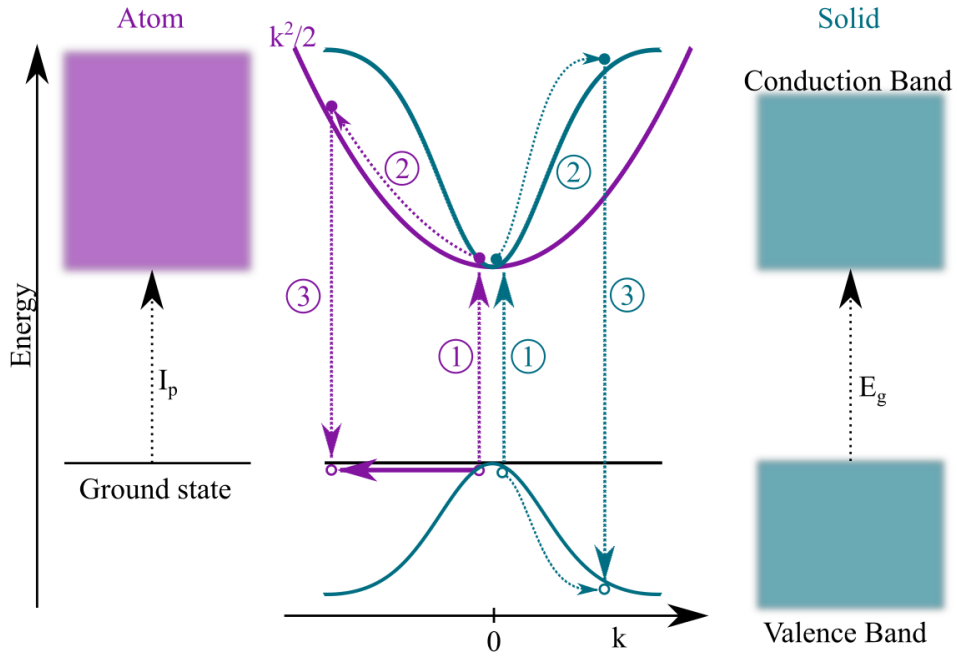

Fig. 3.0.1: Mechanisms of high-order harmonic generation in atoms and solids. **1**. Vertical transitions from the valence (ground state) to the conduction band (continuum). **2**. (Intraband) acceleration of the excited electrons by the laser field. **3**. Recombination of the excited, accelerated carriers.

the gas phase is treated in Sec. 3.2.
Note that in the following sections only the single-atom response of the target to the incident electromagnetic field will be discussed. The measured quantity in any harmonic generation experiment is the result of this microscopic response and the macroscopic response (i.e. the phase matching condition [1]) that is determined by the optical properties of the material and the irradiation conditions.

3.1 Perturbative harmonic generation

If an ultrashort laser pulse propagates through a dielectric medium the charges in the medium are accelerated by the electromagnetic wave. Hence, a dipole moment is generated. In a macroscopic picture this can be described by the polarization $\mathbf{P}(t)$ already introduced in Sec. 2.1. Microscopically, the generation of a nonlinear polarization can be explained by looking at the behavior of a charge that - in a one-dimensional description - is accelerated within a binding potential $V(x)$. The resulting displacement of the charge - and hence the polarization $P(x)$ - depends on the strength of the restoring force $F(x)$, given by

$$F(x) = -\frac{\partial V(x)}{\partial x}. \tag{3.1.1}$$

For a purely parabolic potential $V(x)$ this leads to a linear relationship between the field strength of the electromagnetic wave and the polarization. If the potential contains anharmonic terms, higher orders appear in the polarization. Figure 3.1.1 demonstrates how a nonparabolic one-dimensional potential leads to the generation of contributions to the polarization oscillating at multiples of the driving field. A cubic term in the potential, which leads to an asymmetry between the $+x$ and $-x$ direction, leads to the generation of a term oscillating at twice the fundamental frequency, while a fourth order term in the potential results in a contribution oscillating at 3ω. Based on this simple description it is obvious that crystals with a centrosymmetric crystal structure only generate odd orders of the fundamental frequency since their inversion-symmetric binding potential only contains even order terms. Generally the nonlinear polarization based on the displacement of bound electrons is only responsible for low-order harmonic generation. It is commonly used for frequency conversion, such as second harmonic generation (SHG) in crystals to generate radiation at wavelengths that are not directly accessible.
In a two-color scheme the bound electron nonlinearity can lead to the formation of low-order harmonics via a coupling of the two beams through the nonlinear optical susceptibility. Assuming the combination of a strong pump laser pulse of frequency ω_{pump} and a weak probe laser pulse of frequency ω_{probe} and only considering nonlinearities driven by the strong pump pulse, two-color harmonics

[1] for an introduction to phase matching see Sec. 7.1

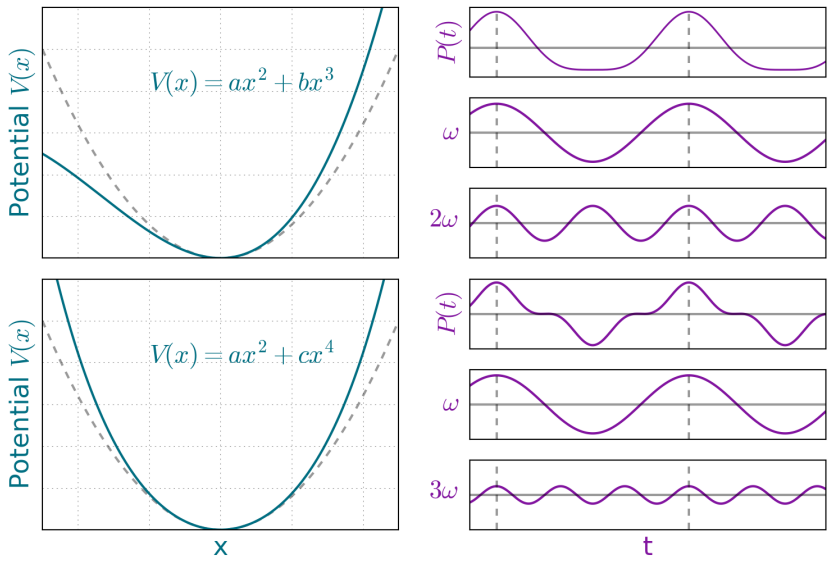

Fig. 3.1.1: Schematic of harmonic generation due to a nonparabolic binding potential of bound electrons. A purely parabolic potential is indicated by the dashed lines.

are generated at frequencies given by

$$\omega_n = 2\,n\,\omega_{\text{pump}} + \omega_{\text{probe}}, \tag{3.1.2}$$

with n being an integer. For $n = 1$ this describes a four-wave mixing process based on the third-order susceptibility $\chi^{(3)}$ of the target which is well characterized for many materials. Due to the significantly smaller values of higher order susceptibilities, higher order wave mixing will generally lead to a smaller harmonic yield. Furthermore, no plateau-like behavior - as known from recollision type harmonics in gases - is expected for Kerr-type harmonic generation in solids. The intensity scaling of harmonics generated by Kerr-type nonlinearities follows a simple perturbative scaling law. The order of the nonlinear dependence of the harmonic yield on the laser intensity is dictated by the number of photons involved in the frequency conversion process.

3.2 Interband HHG

In a crystalline solid, the electrons are initially present in bound states in the valence band which is energetically separated from higher-lying conduction bands. The energy gap between valence and conduction band E_g is the equivalent of the ionization potential U_p in the atomic case. As discussed in Sec. 2.2.1 electrons are excited from bonding states in the valence band to anti-bonding states in the conduction band close to the peaks of an incident laser field while leaving a hole in the valence band behind. After the promotion of an electron to the conduction band the electron-hole pair is accelerated by the laser field. The resulting motion in momentum space is thereby fundamentally different from that in the atomic case. Due to the fixed distribution of atoms in the crystal lattice particular energy bands are formed [228]. The exact shape of the bands in which the carriers are accelerated determines the relation of energy and momentum of the electron-hole pairs. Generally, a given crystal structure results in nonparabolic bands in momentum space. As can be seen from Fig. 3.0.1 the electronic energy also increases with increasing momentum. After a half cycle of the driving field the accelerating laser field changes sign. Subsequently, the excited carriers (electrons and holes) are driven in the opposite direction. Hence, the electron can recollide with the hole both having non-zero momentum. Note that Fig. 3.0.1 shows a representation of the energy levels in momentum space. Here the electron follows a trajectory that would be described by a particular form of $k(t)$ with k being the momentum. There is an accompanying picture (not shown) in real space where the electron follows a trajectory $x(t)$. It is along this trajectory that the electron can re-encounter the hole in the valence band. During this recollision process a high energy photon with energy

$$\hbar\omega = E_g(k), \tag{3.2.1}$$

can be produced. Here $E_g(k)$ denotes the energy gap between the valence and conduction band at a given momentum k (see Fig. 3.0.1). The time of electron-hole recollision also critically depends on the dispersion of the energy bands. The velocity $v_m(k)$ of a carrier in a given band m is given by [178]

$$v_m(k) = \nabla_k E_m(k), \tag{3.2.2}$$

where $E_m(k)$ represents the shape of the energy band and ∇ the nabla operator. Electrons and holes will reach different velocities due to the different curvatures of the valence and conduction band. In order to estimate the time of recollision the real space trajectories of electrons and holes have to be calculated by solving

$$x_e(t) = \int_{t_0}^{t} \nabla E_c(k(\tau))d\tau, \qquad x_h(t) = \int_{t_0}^{t} \nabla E_v(k(\tau))d\tau, \tag{3.2.3}$$

with conduction and valence band E_c and E_v and t_0 denoting the time of the interband excitation of the electron. Only when these trajectories cross, electron-hole recollision and the accompanying generation of high energy photons is possible.
In solid state systems the recollision of conduction band electrons with their associated holes has been validated by experimental studies using terahertz (THz) fields to accelerate and recollide the quasiparticles [196]. Experiments performed in photoexcited ZnO crystals have identified the interband recollision mechanism as the dominant source of high-order harmonics generated by a mid-infrared laser field [214]. Furthermore, recollision-type harmonics were used to reconstruct the band structure of ZnO [209].

3.3 Intraband HHG

The nonparabolic energy landscape of conduction and valence bands along which the laser field drives electrons and holes constitutes a further source of nonlinearity. After interband excitation of an electron to the conduction band it is further accelerated within the band by the laser field. Once the electric field changes sign, the direction of acceleration changes accordingly. If the driving field strength is strong enough the electron is accelerated across the entire Brillouin zone and undergoes a Bloch oscillation [154, 229]. Therefore intraband harmonics are often referred to as Bloch harmonics. Harmonic generation due to Bloch oscillations of excited electrons in the band structure of a crystal has been studied both theoretically [157] and experimentally [188, 194, 200, 205].
However, it is not necessary that the electrons explore the full Brillouin zone to generate high frequency photons. Instead, harmonics can already be generated as a result of the nonparabolic shape of $E(k)$, as illustrated in Fig. 3.0.1 [211]. The independent motion of the quasi-free carriers in the valence and conduction

bands results in an nonlinear intraband current density given by [198]:

$$j(t) = \rho(t)v(t)e. \tag{3.3.1}$$

Here, $v(t)$ denotes the velocity of the electron (or hole) wavepacket

$$v(t) = \hbar^{-1}\frac{\partial E(k)}{\partial k}|_{k(t)}. \tag{3.3.2}$$

Hence, the nonlinear dispersion of the energy bands enters via the acceleration of the free carriers by the laser field. The high-harmonic spectrum resulting from the intraband current can be computed by [150]:

$$\mathrm{HHG}(\omega) = \left| \int \left(\frac{\partial j(t)}{\partial t} \right) \exp(-i\omega t) \right|^2. \tag{3.3.3}$$

Hence, high-order harmonic generation due to nonlinear charge oscillations within the valence and conduction bands of a crystalline solid can be used to retrieve information on the nonlinear dispersion of these bands. While Schubert et al. demonstrated the existence of dynamical Bloch oscillations in GaSe [205], Lanin et al. retrieved the anharmonic band structure of ZnSe by analyzing the intensity dependence of the high-harmonic yield generated by a few-cycle MIR laser pulse [198]. Similarly, Luu et al. revealed fine details of the energy dispersion profile of the conduction band of SiO_2 by analyzing high-order harmonics generated with the help of few-cycle waveforms [194]. Theoretical investigations even predict the possibility of two-dimensional imaging of energy bands in a h-BN crystal relying on the polarization dependence of the high-order harmonic yield [230].

3.4 Brunel harmonics

While the nonlinearity of bound electrons leading to Kerr-type harmonics as well as inter- and intraband harmonics have been extensively considered in the literature in recent years, a prominent source of nonlinearity has been almost fully neglected up to now, namely the nonlinearity of strong-field ionization. As discussed in Sec. 2.2.1, SFI is a highly nonlinear process. Thus, it also constitutes a source of harmonic generation. Even though the nonlinearity of SFI has been mostly overlooked in the discussion of HHG in solids in recent years, the potential of sub-cycle ionization dynamics for the formation of harmonics was already predicted by F. Brunel in his seminal work in 1990 [24].
The sub-cycle dynamics of the plasma density due to the oscillatory behavior of a field-phase-sensitive ionization rate as discussed in Sec. 2.2.6, lead to a periodic modulation of the resulting intraband current density. As derived in [24, 231, 232] assuming zero velocity for new-born electrons ($\mathbf{v}(0) = 0$) and neglecting collisions, the time derivative of the macroscopic plasma current

density (as given in Eq. 3.3.1) follows as

$$\frac{\partial j(t)}{\partial t} = \frac{q_e^2}{m_e} E(t)\rho(t). \tag{3.4.1}$$

The periodic and nearly stepwise increase of the plasma density at every half cycle of the optical field leads to the formation of odd harmonics of the driving field according to the mechanism illustrated in Fig. 3.4.1.

In the left panel of Fig. 3.4.1 the stepwise increase of the plasma density due to SFI is sketched with sharp steps appearing close to the peaks of the laser electric field. The total plasma formation due to SFI - $\rho_{\mathrm{SFI}}(t)$ - can therefore be decomposed into the sum of a smooth, cycle-averaged contribution $\rho_{\mathrm{caSFI}}(t)$ (see upper right panel of Fig. 3.4.1) and an oscillating component $\rho_{sub}(t)$ (bottom right panel of Fig. 3.4.1). Thus, $\rho_{\mathrm{sub}}(t)$ contains the fast, high-frequency component of the plasma density buildup. A high-frequency signal in the temporal domain naturally carries a signature in the frequency domain at nonzero frequencies. Hence, $\rho_{\mathrm{sub}}(t)$ maps sub-cycle, attosecond ionization dynamics into the frequency domain.

According to the previous description of the inter- and intraband mechanisms

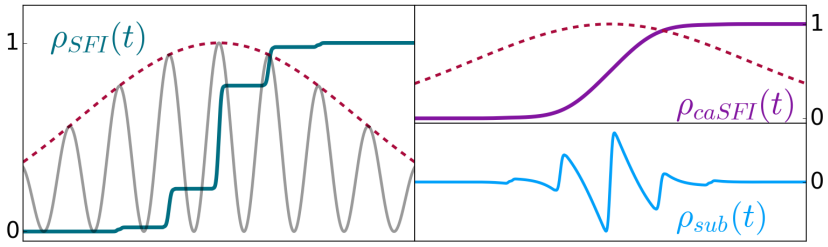

Fig. 3.4.1: Decomposition of the plasma formation due to SFI into a cycle-averaged, low-frequency [$\rho_{\mathrm{caSFI}}(t)$] and a sub-cycle, high-frequency component [$\rho_{\mathrm{sub}}(t)$].

Brunel harmonics can be understood as an intraband mechanism due to SFI. Vampa et al. even include the Brunel mechanism into their description of intraband HHG in solids [211]. In strong analogy with Eq. 3.3.3, the optical signature of the transverse macroscopic plasma current density is given by the squared modulus of the Fourier transform of $\partial j(t)/\partial t$:

$$I_{\mathrm{Br}}(\omega) = \left| \int \rho(t) E(t) \exp(-i\omega t) dt \right|^2 . \tag{3.4.2}$$

Within our work, these equations have to be adapted for the two-color pump-probe scenario that was already discussed in Sec. 3.1. The strong pump laser pulse of frequency ω_{pump} drives the valence to conduction band excitation. Besides

the pump laser pulse, a weak, time-delayed probe laser field $E_{\mathrm{probe}}(t-\tau)$ of frequency ω_{probe} also interacts with the quasi-free electrons generated by the pump laser pulse. This results in a total plasma current density given by

$$\frac{\partial j(t,\tau)}{\partial t} \propto E_{\mathrm{pump}}(t)\rho(t) + E_{\mathrm{probe}}(t-\tau)\rho(t). \tag{3.4.3}$$

Neglecting the delay-independent contribution due to the interaction of the pump laser field with the pump-induced plasma density and once again deriving the optical signature as described above, leads to the following expression for the delay-dependent Brunel harmonics from a two-color laser field:

$$I_{\mathrm{Br}}(\omega,\tau) = \left| \int \rho(t) E_{\mathrm{probe}}(t-\tau)\exp(-i\omega t)dt \right|^2 . \tag{3.4.4}$$

Time-resolved detection of Brunel harmonics was initially performed in gases [25, 227] before the technique was adapted to solids in an experimental configuration limiting the observation to the first harmonic order [26]. Within this work, time-resolved experiments on two-color wave mixing in fused silica will be presented in Ch. 6. Using a long wavelength excitation pulse allows the detection of higher harmonic orders potentially enabling the reconstruction of the plasma dynamics due to strong-field ionization by Fourier analysis of the delay-dependent harmonic spectra.

Chapter 4

Experimental Setup

In this chapter a detailed description of the experimental apparatus used in the experiments discussed in chapters 5-8 is provided. The laser source is described in Sec. 4.1, the experimental setup is detailed in Sec. 4.2 and a comprehensive characterization of the spatio-temporal properties of the pump and probe laser beams is presented in Sec. 4.3.

4.1 Radiation Source

A commercial Ti:Sapphire laser system (Spectra Physics Spitfire) based on a regenerative amplifier serves as the laser radiation source. The system delivers pulses with an energy of $E_p \approx 3.3\,\mathrm{mJ}$ and a duration of $\tau \approx 40\,\mathrm{fs}$ [full width half maximum (FWHM)] around a central wavelength of $\lambda \approx 800\,\mathrm{nm}$ at a repetition rate of $f_{\mathrm{rep}} = 1\,\mathrm{kHz}$. A fraction of the pulse energy ($\approx 1.1\,\mathrm{mJ}$) is used to pump a commercial optical parametric amplifier (OPA, Light Conversion, model TOPAS C).
The OPA consists of two stages. In the first stage a minor part of the input energy is employed to generate a white light continuum in a sapphire plate. This coherent continuum is temporally and spatially overlapped with a part of the 800 nm pulse inside a nonlinear crystal using a non-collinear focusing geometry. The generated signal that is very weak (typically on the nJ level) is afterwards combined with the leftover part of the fundamental 800 nm pulse carrying the major part of the input energy in a second nonlinear crystal. Thereby, the wave mixing signal generated in the first nonlinear crystal is amplified. Due to the collinear geometry in the second nonlinear crystal the generated signal and idler beams are emitted collinearly from the OPA. In the presented experiments only the idler of the OPA is used. The central wavelength of the idler can be tuned from $\approx 1950\,\mathrm{nm} - 2450\,\mathrm{nm}$ with a pulse energy of up to $\approx 100\,\mu\mathrm{J}$ and a FWHM pulse duration of $\leq 150\,\mathrm{fs}$.

4.2 Design and implementation of the experimental apparatus

The full experimental apparatus, sketched in Fig. 4.2.1, combines a fraction ($\leq 250\,\mathrm{nJ}$) of the near-infrared output of the Ti:Sapphire laser and the idler of the OPA in a close-to-collinear pump-probe experiment.
Since the direct output of the Ti:Sapphire with a central wavelength of $\approx 800\,\mathrm{nm}$ will be used as a probe laser pulse in the experiments it is attenuated by multiple reflections on glass wedges (Thorlabs PS810). Reflection on wedges is chosen instead of transmissive attenuator options like ND-filters or the combination of a half-waveplate and a polarizer to avoid additional dispersion effects. Hence, the original pulse duration can be maintained at the position of the actual experiment.
The idler generated in the OPA is used as a MIR pump laser pulse. Separation

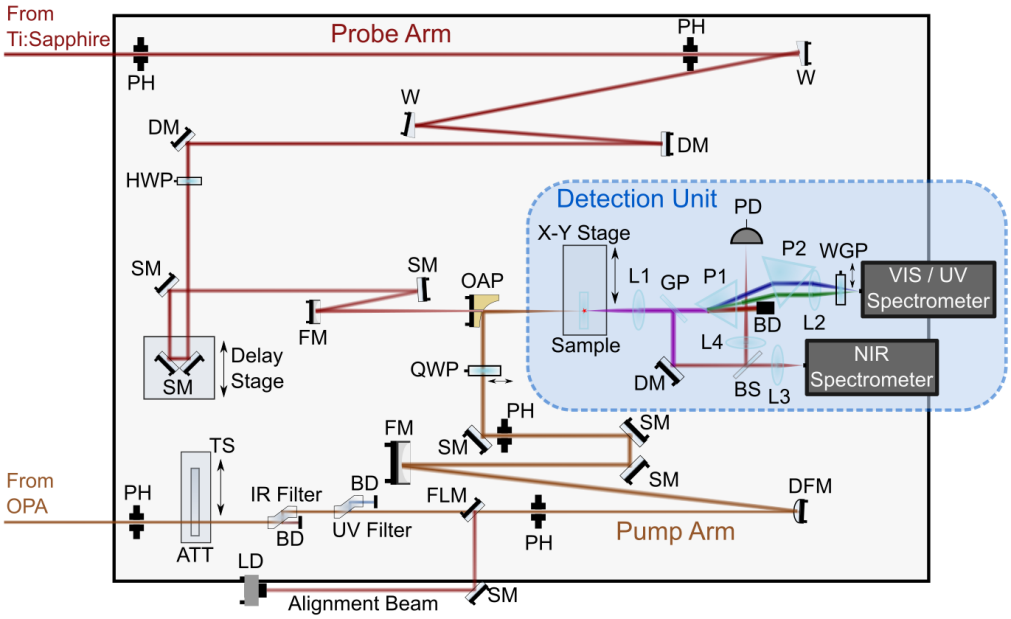

Fig. 4.2.1: Overview of the experimental setup for the pump-probe experiments. P: Pinhole, PER: Periscope, W: Wedge, DM: Dielectric mirror (HR 800 nm), HWP: Zero-order half-waveplate, SM: Silver mirror, FM: Focusing mirror, ATT: Attenuator, TS: Translation stage, BD: Beamdump, LD: Laser diode, FLM: Flip mirror, DFM: Defocusing mirror, QWP: Zero-order quarter-waveplate, OAP: Off-axis parabolic mirror, L1 - L4: Lenses, GP: Glass plate, BS: Beam splitter, P1 & P2: Prisms, PD: Photodiode, WGP: Wire grid polarizer.

of the collinearly emitted signal and idler beams is carried out with the help

of a wavelength separator consisting of dichroic mirrors. The mirrors utilized in the wavelength separator are highly reflective in a wavelength range from 1900 nm to 2600 nm. In order to vary the intensity of the pump laser pulses in the measurements a linear neutral density (ND) filter is mounted on a computer-controlled translation stage (Physik Instrumente M-126.DG). Furthermore, a zero-order tunable quarter-wave phase retardation plate (Alphalas) can be inserted into the beam path to circularly or elliptically polarize the pump laser pulse. Prior to focusing, the pump laser beam is magnified by a factor of four using a reflective telescope consisting of a silver-coated defocusing mirror and a silver-coated focusing mirror. After magnification the MIR pump beam is focused into the fused silica sample using a gold-coated off-axis parabolic mirror (OAP) with a reflected focal length of ≈ 50 mm and a central hole.
In the probe arm the weak NIR laser beam is guided to a roof mirror mounted on a motorized, computer-controlled delay stage (Physik Instrumente M-110.DG). A zero-order half-wave phase retardation plate (HWP, Thorlabs WPH10M-808) is used to manipulate the polarization of the 800 nm probe laser pulse. It is mounted on an automated rotation stage (Physik Instrumente M-060.DG). Afterwards, the NIR pulse is focused through the central hole of the OAP into the fused silica sample by using a silver-coated spherical mirror ($f = 300$ mm). The a-SiO_2 sample (UV Grade fused silica, Corning 7980) of 500 µm thickness is mounted on two computer-controlled linear stages (Physik Instrumente M-126.DG) to enable scanning of the sample in the horizontal and vertical direction perpendicular to the propagation direction of the pump laser pulse. While there is a small angle between the MIR pump and the NIR probe laser pulse ($\alpha_{\text{pu-pr}} < 5°$) the fused silica sample is always aligned orthogonally to the intense MIR pump laser pulse. Normal incidence is ensured by an additional laser diode providing light in the visible spectral range around 630 nm. The beampath of the laser diode is parallel to that of the MIR pulse (see Alignment Beam in Fig. 4.2.1). Thus, the back reflection of the visible radiation from the fused silica substrate can be used for a precise alignment of the sample. Back reflection into the laser diode is avoided due to the central hole in the OAP.
After interaction with the sample the radiation escaping from the target is collected by a CaF_2 lens. A thin (500 µm) UV-grade fused silica plate is used to separate a small fraction of the radiation for analyzing the NIR probe pulse, while the major part is transmitted. The detection unit that follows behind the SiO_2 plate (indicated by the colored area in Fig. 4.2.1) consists of two parts. A detailed overview of the detection unit is provided in Fig. 4.2.2.

Harmonics Analysis The transmitted part of the radiation is directed to a CaF_2 prism (P1 in Fig 4.2.2). During propagation through prism P1 the light is dispersed so that the fundamental pump and probe wavelengths can be spatially blocked by a beam dump (BD). The remaining frequencies are recollimated using a UV-grade fused silica prism (P2). After propagating through prism P2

all the frequencies are parallel to each other and can be focused onto the fiber input of a VIS/UV spectrometer (Avantes AvaSpec-HS1024x58/TEC) using a single CaF_2 lens (focal length: 50 mm). Before focusing the ultraviolet (UV) and visible (VIS) radiation into the spectrometer, a broadband wire grid polarizer (Thorlabs WP25M-VIS) on a manual rotation stage can be inserted into the beam path to analyze the polarization state of the remaining frequencies. The VIS/UV spectrometer detects higher energy photons that are generated during the interaction of the pump and probe laser pulses in the fused silica sample. Since the pump and probe laser pulses are overlapped using a close-to-collinear focusing geometry with a small angle between the two, the propagation direction of the newly generated frequencies will be dictated by the respective phase matching condition (introduction to phase matching given in Sec. 7.1). Hence, the generated frequencies that are to be detected by the spectrometer are escaping from the target under different angles. To enable a simultaneous detection of generated frequencies spanning the full detection range of the spectrometer ($\approx$ 160 nm to 550 nm) a precise alignment of the two prisms is necessary. Especially, the relative angle of the second prism with respect to the first prism heavily determines the frequency range that falls on the detector. In order to simplify the alignment and the injection of a broad frequency spectrum into the optical fiber, the input of the fiber is fixed within a kinematic mount. This mount is attached to three manual translation stages allowing a precise positioning of the fiber input in the x, y and z direction. To avoid losses that are typically non-negligible in fused silica optical fibers especially in the UV range of the spectrum, a short fiber of 5 cm length is used in the experiments.
While the major part of the radiation escaping the fused silica sample is utilized to analyze the generated UV and VIS frequencies, the minor part that was split off by the fused silica plate (GP in Figs. 4.2.1 & 4.2.2) is guided towards the probe analysis part of the detection unit.

Probe Analysis The light that is reflected from the SiO_2 plate is directed onto a dielectric mirror that is high reflective for 800 nm. This mirror acts as a spectral filter on the polychromatic beam and isolates the fundamental probe wavelength. Subsequently, the beam is split into two equally intense parts. One part is focused onto the fiber input of a NIR spectrometer (Avantes AvaSpec-LS2048) by an AR-coated lens of 250 mm focal length, in order to analyze the probe spectrum after the interaction with the a-SiO_2 sample. The second part is focused onto a photodiode (Ophir PD-10) in order to analyze the time-resolved transmission of the NIR probe laser pulse, again using an AR-coated lens of 250 mm focal length.

All three detectors used in this setup (the VIS/UV spectrometer, NIR spectrometer and photodiode) together with the five motorized stages (pump attenuator stage, probe delay stage, sample x-y stage and HWP rotation stage) are computer-controlled via a homemade software system programmed in Python. Hence, fully

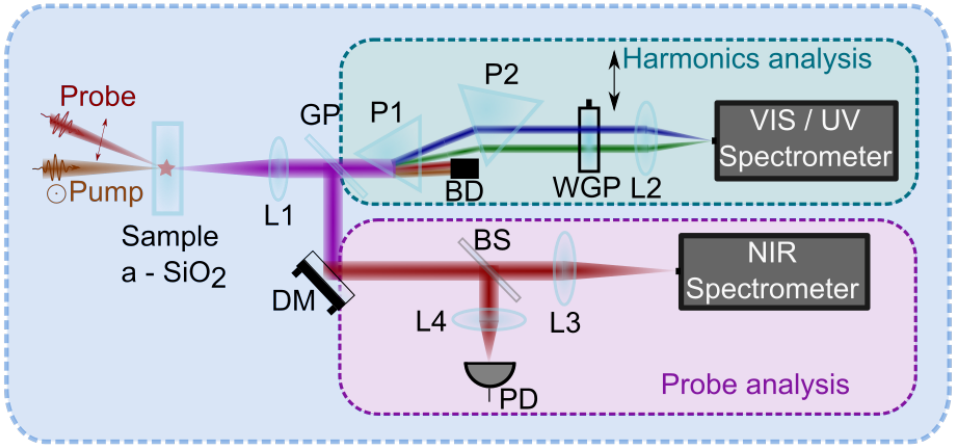

Fig. 4.2.2: Detailed drawing of the detection unit of the experimental setup. L1 - L4: Lenses, GP: Glass plate, P1 & P2: Prisms, BD: Beam dump, DM: Dielectric mirror (HR 800 nm), BS: Beam splitter, PD: Photodiode, WGP: Wire grid polarizer.

automated time-and intensity-resolved measurements can be performed. Using the computer-controlled HWP in the probe beam path it is furthermore feasible to change the polarization geometry from perpendicular to parallel pump and probe laser polarizations.

4.3 Characterization

In the following sections results on the characterization of the pump and probe laser pulse parameters are presented. First, the characterization of the spatial beam profiles in the focal plane by the knife-edge technique is discussed. Furthermore, both the idler of the OPA and the direct Ti:Sapphire output are characterized temporally and spectrally.

4.3.1 Spatial characterization

Prior to the characterization of the spatial beam profile of the focused MIR pump laser pulse the off-axis parabolic mirror needs to be aligned. Therefore the beam profile of the visible laser diode that is mainly used for the alignment of the SiO_2 sample is monitored in the far field. Due to the central hole in the OAP a slight misalignment of the focusing mirror leads to strong distortions of the beam profile in the focal plane. Hence, adjustment of the OAP alignment while monitoring the spatial beam profile of the laser diode in the far field drastically improves the beam profile in the focal plane. In a second step the intense MIR pump pulse is used to induce modifications on the surface of a fused silica sample.

The resulting modifications are investigated with the help of a microscope. For the final alignment the OAP is adjusted in order to optimize the shape of the laser-induced damage morphologies as illustrated in Fig. 4.3.1. Following this alignment procedure the beam profile of pump and probe laser pulses can be characterized in the focal plane.

Spatial characterization of the laser beam profiles is achieved with the help

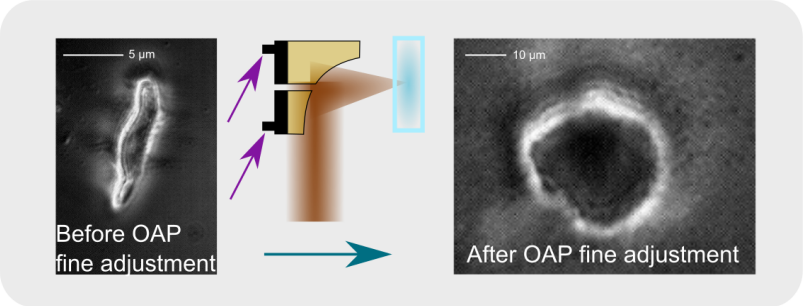

Fig. 4.3.1: Damage tracks at different levels of fine adjustment of the OAP. By optimizing the alignment of the focusing mirror the shape of the laser-induced modification in a fused silica sample can be converted from strongly elliptical to round.

of the knife-edge method [233–235]. Since commercially available beam-profiler cameras do not provide sufficient resolution especially for wavelengths in the MIR spectral region [236] the conventional knife-edge measurement offers a simple and well-proven technique. Especially for MIR laser pulses knife-edge measurements are often used to characterize the spatial beam profile [190, 198, 199].

A knife-edge measurement requires a sharp edge (e.g. a razor edge) mounted on

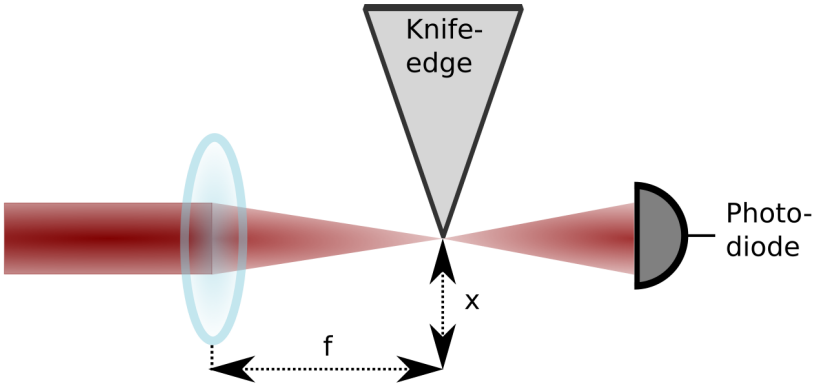

Fig. 4.3.2: Schematic visualization of a knife-edge measurement. The knife-edge is located at distance f from the focusing objective. It is mounted on a translation stage allowing a measurement of the transmitted laser power as a function of the knife-edge position x in the focal plane.

a horizontal and/or vertical translation stage in the position of the focal plane. The transmitted energy is measured by a photodiode or a powermeter while the sharp edge is moved perpendicular to the propagation direction of the laser, partially blocking the beam as sketched in Fig. 4.3.2.
A radially symmetric Gaussian laser beam profile can be described by

$$I(x,y) = I_0 \exp\left\{-\frac{(x-x_0)^2+(y-y_0)^2}{w^2}\right\}. \tag{4.3.1}$$

Here x_0 and y_0 denote the coordinates of the center of the beam and w describes the radius of the beam at the position where the intensity is decreased to $1/e$ times the peak value I_0. The resulting normalized transmitted power as a function of the knife-edge position in the x-direction is given by [235]

$$P_N = \frac{1}{2}\left\{1 + \mathrm{erf}\left(\frac{x-x_0}{w}\right)\right\}, \tag{4.3.2}$$

with erf the error function.
Knife-edge measurement results for the pump and probe laser beams are shown in Fig. 4.3.3. The experimentally obtained transmitted intensity as a function of the knife-edge position in both horizontal and vertical direction is fitted to Eq. 4.3.2. The resulting reconstructed beam profiles in the focal plane are displayed in Fig. 4.3.3(c) & (f). Note that for the presented analysis an elliptical beam profile with long and short axes defined by the measurement is assumed. Furthermore the spatial beam profile in both directions is approximated by a Gaussian. Especially in the case of the MIR pump laser pulse the obtained beam diameters in the horizontal and vertical direction differ. Possible reasons for this result are the nonlinear generation process of the idler pulse in the OPA leading to significantly higher instability in the pointing, energy and duration of the generated pulses. Furthermore, the reflective telescope used to magnify the pump beam profile prior to focusing constitutes a source for aberrations and distortions of the beam profile. Finally, due to the central hole in the OAP used to focus the MIR laser beam, a perfect Gaussian intensity distribution in the focal plane is not expected. To compensate for the difference between the beam radii obtained for the vertical and horizontal direction an effective beam radius w_{eff} is defined by

$$w_{\mathrm{eff}} \equiv \frac{w_x + w_y}{2}. \tag{4.3.3}$$

The resulting effective $1/e^2$ beam radii are 72.3 µm for the NIR probe laser pulse and 32.9 µm for the MIR pump laser pulse. Estimating the ellipticity $\mathcal{E}$ of the beam profiles in the focal plane using the relation

$$\mathcal{E} = 1 - \frac{w_{\mathrm{min}}}{w_{\mathrm{maj}}}, \tag{4.3.4}$$

where w_{maj} and w_{min} denote the major and minor axes of the ellipse yields an ellipticity of $\mathcal{E}_{\mathrm{NIR}} = 0.15$ for the NIR pulse and $\mathcal{E}_{\mathrm{MIR}} = 0.31$ for the MIR pulse.

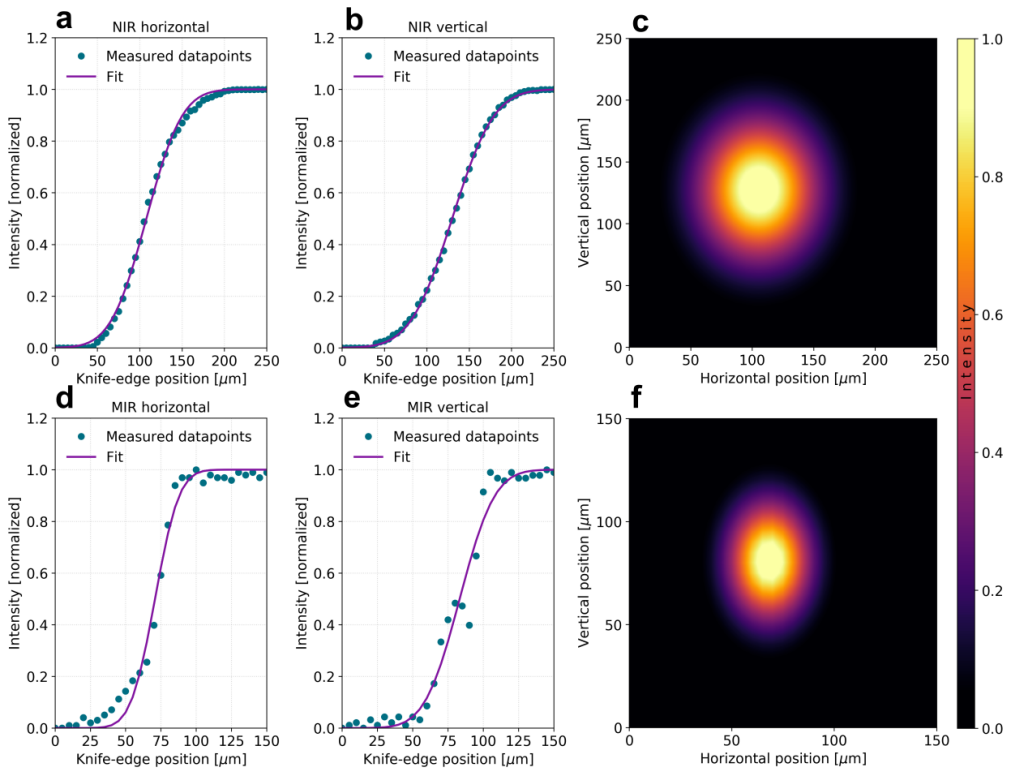

Fig. 4.3.3: Spatial characterization of the pump and probe laser pulses. **a** & **b**. Knife-edge measurements obtained for the NIR probe laser pulse by scanning the knife-edge in the horizontal and vertical direction. **c**. Reconstructed beam profile of the 800 nm pulse. **d** & **e**. same as **a** & **b** for the MIR pump laser pulse. **f**. Same as in **c** for the MIR pump laser pulse.

4.3.2 Temporal & spectral characterization

Temporal characterization of the 800 nm pulse is achieved with the help of a commercial SPIDER (Spectral Phase Interferometry for Direct Electric-field Reconstruction [237]) system (APE LX SPIDER). An experimental result for the temporal characterization of the NIR laser pulse is given in Fig. 4.3.4(a). The measured temporal envelope of the laser pulse intensity, exhibiting a FWHM pulse duration of 46.5 fs, is compared to the 36.9 fs Fourier limit that represents the shortest pulse possible according to the measured spectral bandwidth . The spectral phase that is reconstructed by the SPIDER algorithm is also included in Fig. 4.3.4(a). By optimization of the compressor gratings inside the regenerative

amplifier of the Ti:Sapphire system it is possible to compress the pulses to a FWHM pulse duration below 40 fs. However, in the experiments the position of the gratings is adjusted to maximize the performance of the OPA. Hence, the presented temporal characterization of the probe pulse shows a pulse that is slightly stretched compared to the shortest pulse available with the used laser system.

The idler of the OPA is temporally characterized by a cross-correlation technique.

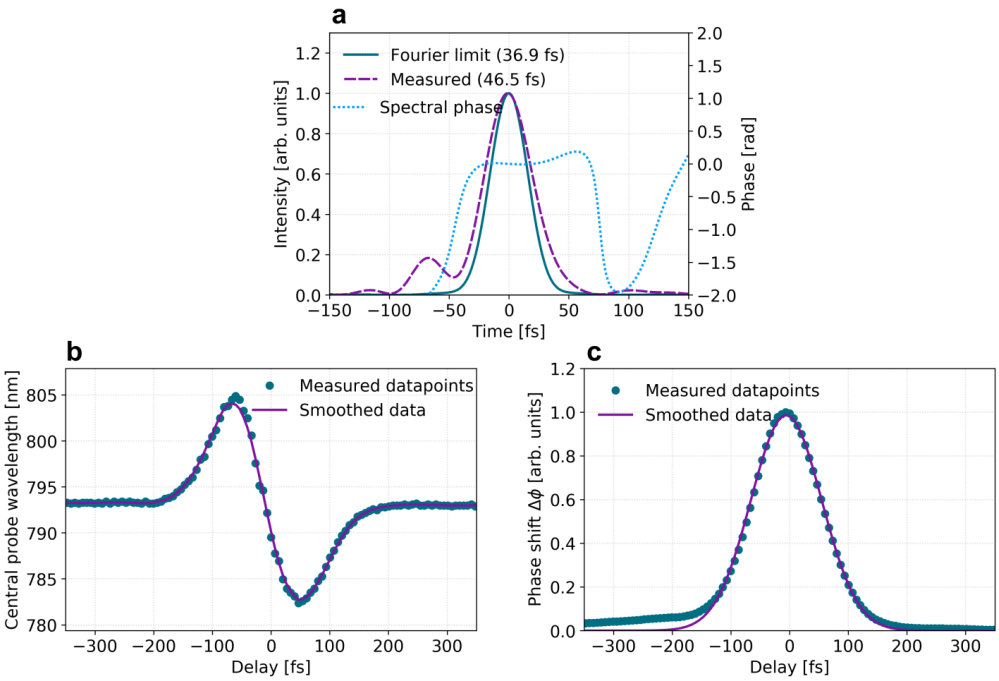

Fig. 4.3.4: Temporal characterization of the pump and probe laser pulse. **a**. SPIDER measurement of the NIR probe laser pulse. **b**. Central probe wavelength shift as a function of the pump-probe delay due to XPM. **c**. Resulting phase shift induced by the strong MIR pulse in fused silica and probed by the NIR probe laser pulse in order to characterize the temporal structure of the pump laser pulse.

By focusing the strong MIR pump pulse into a bulk fused silica sample a refractive index variation according to Eq. 2.1.14 is generated. When the weak probe pulse is overlapped temporally and spatially with the pump laser pulse it experiences a phase shift and reads out the pump-induced refractive index variation. This cross-phase modulation (XPM, see Sec. 2.1.2) signal encodes the amplitude of the pump pulse as a pump-probe delay-dependent frequency variation of the probe laser pulse. Hence, after determining the wavelength shift and numerically deconvoluting the result by the well-characterized probe pulse envelope, the temporal shape of the MIR pulse is obtained.

Figures 4.3.4(b) & (c) show experimental results obtained by following the

described method. The variation of the central probe wavelength as a function of the pump-probe delay τ is displayed in Fig. 4.3.4(a). Figure 4.3.4(b) displays the accumulated phase shift $\Delta\phi$ due to the pump-induced refractive index variation in the interaction region as a function of the pump-probe delay (prior to deconvolution). Since the pump-induced phase shift $\Delta\phi$ is proportional to the intensity of the pump laser pulse the measurement provides the temporal envelope of the MIR pump pulse. The resulting FWHM pulse duration is evaluated to $\approx 140\,\mathrm{fs}$ at a pump wavelength of 2100 nm.
Spectral characterization of the laser pulses used in the experiments is performed with the help of commercial fiber spectrometers. The spectrum of the Ti:Sapphire pulse as shown in Fig. 4.3.5(a) is characterized using a NIR spectrometer (Avantes AvaSpec-LS2048) revealing a central wavelength of 796 nm and a FWHM spectral width of 32 nm. For the spectral characterization of the MIR pump laser pulse an infrared fiber spectrometer (Ocean Optics NIRQuest) is utilized. The measured

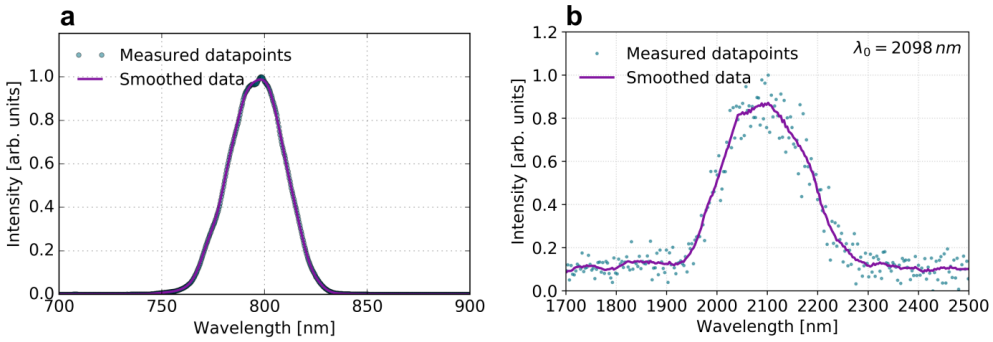

Fig. 4.3.5: **a**. Measured spectrum of the fundamental probe spectrum with a central wavelength of 796 nm. **b**. Spectrum of the MIR pump laser pulse with a central wavelength of 2098 nm.

spectrum of the idler of the OPA is shown in Fig. 4.3.5(b). Analyzing the center of gravity of the smoothed datapoints yields a central wavelength of 2098 nm and a FWHM spectral width of 205 nm.

Chapter 5

Ultrafast plasma formation and relaxation dynamics in solid dielectrics exposed to MIR femtosecond pulses

Historically, time-resolved studies of excitation and relaxation dynamics in transparent dielectrics have proven to significantly improve the understanding of fundamental light-matter interaction down to the femtosecond timescale. A majority of these studies uses the time-resolved transmission [47, 85, 111, 117, 238–241] (and reflection [117, 120, 240]) of a weak probe laser pulse through an interaction region that is influenced by a strong pump laser pulse to deduce information on the dynamics of plasma formation and relaxation. Often, this method is combined with interferometric phase shift measurements to obtain simultaneous information on the variation of the refractive index [45, 47, 48, 117, 242, 243]. Together with well-approved simulation procedures these time-resolved measurements are nowadays considered as a reliable tool to study the dynamics of laser-matter interaction on ultrafast timescales.

Due to the availability of ultrashort pulsed laser sources the wavelengths used in these experiments significantly changed over the past decades. While early studies utilized dye lasers [45, 244, 245] emitting at central wavelengths around 600 nm the prevalence of Ti:Sapphire systems based on chirped pulse amplification (CPA [246]) led to numerous experiments performed at 800 and 400 nm central wavelengths [47, 85, 117, 240]. The current trend towards more flexible radiation sources based on optical parametric chirped pulse amplification (OPCPA) providing ultrashort pulses in the MIR spectral region [247–249] calls for further investigations of transparent solids exposed to long wavelength driving fields. Furthermore, few-cycle MIR pulses are often employed for the generation of high order harmonics from solids [188, 190, 198, 209, 214]. Hence, a better

understanding of the occurring interaction mechanisms is crucial for a microscopic understanding of the HHG processes. Still, up to date only very few experimental data exist for the interaction of MIR pulses with transparent solids [250–252]. In order to elucidate the dynamics of excitation and relaxation of amorphous fused silica irradiated by intense, femtosecond MIR pulses, time-resolved transmission and cross-phase modulation (XPM) studies are presented in this chapter. First, the experimental approach of relying on the transmission of a weak probe laser field to study the dynamics of plasma formation and relaxation is discussed based on theoretical considerations (Sec. 5.1). In what follows the experimental setup and the measurement routine is described before the experimental results are presented in Sec. 5.2. After describing the data processing procedure in Sec. 5.3 the results are summarized and discussed in Sec. 5.4.

5.1 Absorption of radiation through free carriers

Once an intense laser pulse generates an electron-hole plasma in a solid dielectric the optical properties of the material are severely modified (see also Sec. 2.2.3). One important quantity that is directly affected by the excitation of a dielectric is the absorptivity. According to Eq. 2.2.24 the absorption cross-section of an ensemble of quasi-free electrons is given by:

$$\sigma = \frac{e^2}{n_{\mathrm{be}}(\omega_0) m^* c \epsilon_0} \frac{\tau_c}{1+\omega_0^2 \tau_c^2}, \tag{5.1.1}$$

with plasma density-dependent collision time, previously given as Eq. 2.2.28

$$\tau_c = \frac{16\pi\epsilon_0^2}{\rho e^4} \sqrt{\frac{E_{\mathrm{kin}}^3 m^*}{2}}. \tag{5.1.2}$$

The absorption coefficient $\alpha(t)$ is connected to the absorption cross-section as defined in Eq. 5.1.1 through the instantaneous density of conduction band electrons $\rho(t)$:

$$\alpha(t) = \sigma \rho(t). \tag{5.1.3}$$

Assuming a constant value of $\alpha(t)$ over the propagation length L in an irradiated target, the absorption $A(t)$ can be evaluated using the Lambert-Beer law [253]:

$$A(t) = 1 - \exp(-\alpha(t) L). \tag{5.1.4}$$

A numerical calculation of the temporal evolution of the plasma density obtained by solving the rate equation Eq. 2.2.36 for a central laser wavelength of 2100 nm, a pulse duration of 150 fs and a peak intensity of 15 TW cm^{-2} is shown in Fig. 5.1.1(a). The simulation parameters are chosen to reflect the experimental

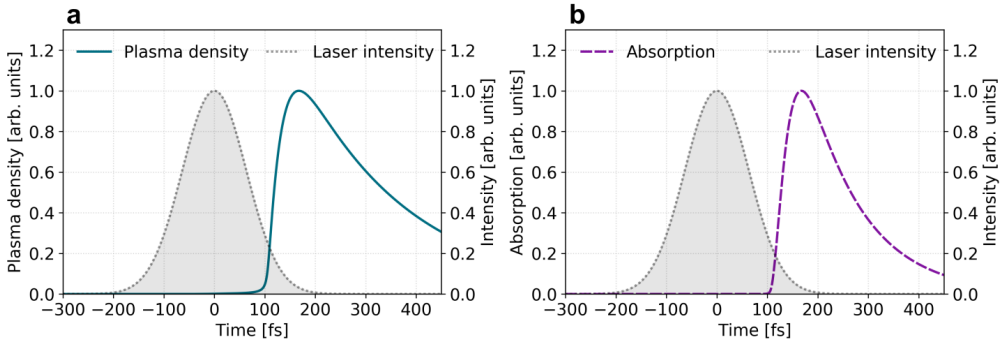

Fig. 5.1.1: **a**. Numerical simulation of the conduction band electron density $\rho(t)$ according to Eq. 2.2.36. **b**. Calculation of the absorption during propagation through 100 µm of fused silica (parameters taken from Tab. 2.1.1). Laser parameters: $\lambda = 2100\,\mathrm{nm}$, $\tau_p = 150\,\mathrm{fs}$, $I_0 = 15\,\mathrm{TW\,cm^{-2}}$.

conditions. The resulting absorption according to Eq. 5.1.4 after propagation through 100 µm of fused silica are presented in Fig. 5.1.1(b). Due to the explicit linear relationship between the absorption coefficient and the plasma density, the temporal profile of $A(t)$ is similar to that of the plasma formation. Differences in the temporal signature result from the implicit dependence of the collision time τ_c on the conduction band electron density. Neglecting the relationship between the collision time and the density of quasi-free carriers and instead using a fixed collision time leads to identical temporal profiles of $\rho(t)$ and $\alpha(t)$. Therefore, the absorption of a weak probe laser pulse propagating through an electron-hole plasma generated by a second strong pump laser pulse has been widely used to study plasma formation dynamics in transparent materials [45, 47, 48, 111, 117, 238–240].

5.2 Experimental results

Only the probe analysis part of the experimental apparatus described in Sec. 4.2 is used for the time-resolved transmission and XPM measurements presented in this chapter. While the transmission of the probe laser pulse through the zone affected by the pump pulse is characterized by the photodiode, the probe spectrum is analyzed by the NIR spectrometer. Thus, the harmonics analysis part of the detection unit is not considered in the experiments discussed in this chapter.

During the measurement, the pump-probe delay is varied using the computer-controlled translation stage in the probe beam path. The intensity of the MIR pump laser pulse can be varied with the help of the linear ND filter. Since the fused silica samples are mounted on a computer-controlled x-y stage they are continuously scanned to provide a fresh spot for every laser shot. Experimentally

obtained data for the time-resolved transmission of the NIR probe laser pulse through the excited fused silica sample are presented in Fig. 5.2.1. The MIR intensity causing the displayed transmission behavior was $9.5\,\mathrm{TW\,cm^{-2}}$. The transmission of the probe laser pulse exhibits a double peak structure. A first peak is observed close to the pump-probe overlap ($\tau = 0$). The second minimum of the transmission follows at a delay of $\approx 100\,\mathrm{fs}$. After the second minimum the transmission slowly recovers and converges towards its initial value for long pump-probe delays.

Simultaneously acquired results recorded by the NIR spectrometer are displayed

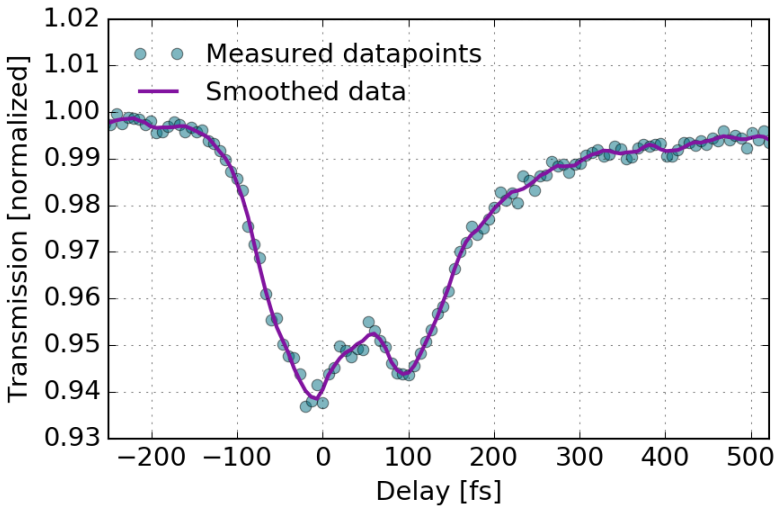

Fig. 5.2.1: Transmission of the NIR probe laser pulse through the fused silica sample as a function of the pump-probe delay as measured by the photodiode (PD) in the probe analysis arm of the experimental setup (see Figs. 4.2.1 & 4.2.2). The MIR pump laser intensity was $9.5\,\mathrm{TW\,cm^{-2}}$.

in Fig. 5.2.2. Figure 5.2.2(a) displays the probe spectrum after interaction with the sample as a function of the pump-probe delay. Strong distortions around pump-probe overlap can be observed. Analyzing the center of gravity of the probe spectrum at each delay yields the result shown in Fig. 5.2.2(b). For negative delays a redshift of the central probe wavelength is observed. Conversely, for positive delays a symmetric blueshift is found. The symmetric variation of the central probe wavelength as a function of the pump-probe delay is identified as a signature of a refractive index variation induced by the strong MIR pump laser pulse inside the SiO_2 sample. According to the theoretical considerations presented in Sec. 2.1.2 an intense pump laser pulse propagating through a nonlinear material leads to a refractive index variation due to the optical Kerr-

effect described by (see also Eq. 2.1.14):

$$n = n_0 + n_2 I. \tag{5.2.1}$$

The weak, time-delayed probe laser pulse experiences this intensity-dependent refractive index of the sample and hence accumulates a phase (see Eq. 2.1.23). This accumulated phase is reflected in the delay-dependent alteration of the central probe wavelength $\Delta\lambda(\tau)$. The phase shift $\Delta\phi$ induced by the intense pump laser pulse can be retrieved by direct integration of the time-resolved variation of the central probe wavelength [see Fig. 5.2.2(b)]:

$$\Delta\phi(\tau) \propto \int_{-\infty}^{\tau} \Delta\lambda(t)dt. \tag{5.2.2}$$

We recall that this technique was already employed to temporally characterize the MIR pump pulse in Sec. 4.3. Here it is noteworthy that no signature of ionization (i.e. ionization-induced blueshift, discussed in Sec. 2.2.3) was observed in the spectrum of the probe laser pulse even at pump intensities surpassing the laser-induced damage threshold of the used samples.

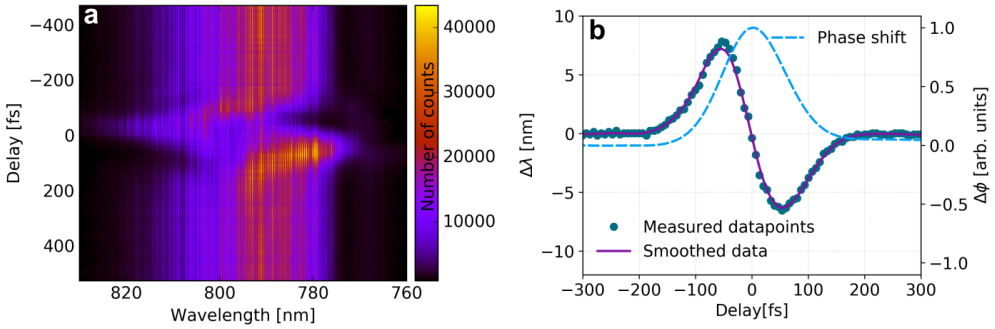

Fig. 5.2.2: **a**. Spectrum of the 800 nm probe laser pulse as a function of the pump-probe delay containing strong distortions due to XPM around the pump-probe overlap. **b**. Extracted time-resolved variation of the central probe wavelength $\Delta\lambda$ and the corresponding normalized phase shift $\Delta\phi$ due to the optical Kerr-effect.

5.3 Data processing

As described above a two-peak structure is observed in the time-resolved transmission of the probe laser pulse. In order to study the dynamics of the electron-hole plasma generated in the sample, the plasma response needs to be extracted from the total loss of transmission. The first maximum of the loss of transmission as shown in Fig. 5.3.1(a) is attributed to reversible processes such as

frequency-mixing between the pump and probe laser pulses (also referred to as two-beam coupling in Ref. [238]). A Gaussian fit function is applied to the first peak, approximating the temporal signature of the reversible processes [see dashed line in Fig. 5.3.1(a)]. Assuming that the remaining loss of transmission is solely due to the generated electron-hole plasma, subtraction of the reversible processes from the total loss of transmission reveals the isolated plasma response [see Fig. 5.3.1(b)]. As discussed in Sec. 5.1 the loss of transmission that the probe laser pulse experiences is attributed to linear absorption of the free carriers generated by the intense pump laser pulse. Hence, the isolated plasma response shown in Fig. 5.3.1(b) is expected to represent the temporal evolution of the conduction band electron density.
In agreement with the numerical results presented in Fig. 5.1.1 the plasma density exhibits a sharp increase until reaching its maximum value. Afterwards, a rather slow decay of the absorption follows and the absorption induced by the electron-hole plasma converges towards the initially observed value. Following the discussion of relaxation phenomena (see Sec. 2.2.4) a single exponential decay time is used to approximate the relaxation of the plasma. As shown in Fig. 5.3.1(b) a decay time of $\tau_{\mathrm{rel}} = 110\,\mathrm{fs}$ is found by applying an exponential fit function to the extracted plasma density relaxation. Though this is a much shorter relaxation time than usually reported (for comparison see Tab. 2.2.1) relaxation times down to 50 fs have previously been measured in fused silica [111].
While the results discussed up to here were acquired for pump intensities below

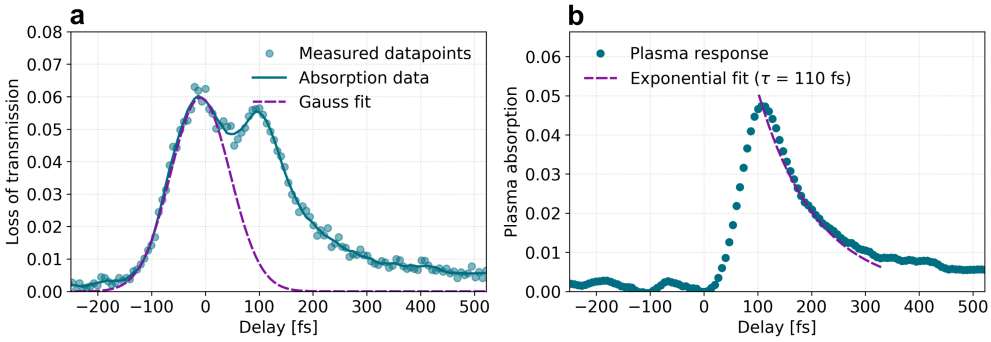

Fig. 5.3.1: Isolation of the plasma response at a pump intensity of $9.5\,\mathrm{TW\,cm^{-2}}$. **a**. Total loss of transmission together with the result of a Gaussian fit to the first peak of the experimental data. **b**. Remaining loss of transmission due to the pump laser-induced plasma formation, and obtained from the experiment by subtracting the result of the Gaussian fit from the total loss of transmission. A fit function with a single exponential decay is used to approximate the relaxation time of the electron-hole plasma.

the laser-induced damage threshold of the fused silica samples the characteristics of the observed time-resolved transmission significantly change for intensities above the threshold. As can bee seen in Fig. 5.3.2(a) the two peaks that were

previously well separated now merge into one plateau-like region from $\approx -50\,\mathrm{fs}$ to 100 fs. Furthermore, the absorption does not recover its initial value anymore. Instead it converges towards a long-lasting non-zero absorption value (≈ 0.025 in Fig. 5.3.2).
Since no distinct two peaks can be identified anymore, the previously described procedure relying on a Gaussian fit to the first peak can no longer be applied. Instead, the leading edge of the extracted time-resolved absorption is compared to the simultaneously acquired normalized phase shift [see dashed line in Fig. 5.3.2(a)]. Due to the identical temporal footprint of the reversible component of the loss of transmission and the phase shift, the plasma contribution to the total probe absorption can still be isolated by subtracting the temporal profile of the phase shift from the total loss of transmission [(see Fig. 5.3.2(b)]. Both strategies to isolate the plasma response from the total loss of transmission are presented here since at low intensities the low signal-to-noise ratio of the XPM measurement impedes the extraction of the phase shift. Conversely, at high intensities the two peaks observed in the time-resolved absorption measurement merge, hence complicating the approximation of the leading edge by a Gaussian function. Therefore, the presented processing strategies enable the characterization of the plasma and relaxation dynamics over a wide range of pump laser pulse intensities.
Experimental results obtained for varying intensities of the MIR pump laser pulse

Fig. 5.3.2: Isolation of the plasma response at a pump intensity of $16\,\mathrm{TW\,cm^{-2}}$. **a**. Time-resolved loss of transmission as a function of the pump-probe delay together with the resulting phase shift obtained from the XPM measurement. **b**. Resulting plasma response isolated by subtracting the signature of XPM from the total loss of transmission.

are presented in Fig. 5.3.3. The maximum plasma absorption as a function of the pump intensity is displayed in Fig. 5.3.3(a). Due to the nonlinear dependence of the excitation mechanisms leading to the formation of an electron-hole plasma on the laser intensity (see Secs. 2.2.1 & 2.2.2) the maximum value of the absorption increases monotonously in a nonlinear fashion up to the damage threshold of the

SiO_2 samples. The error of the displayed experimental results is estimated as the sum of the uncertainty of the detector (≈ 0.005) and the experimental error due to instabilities of the laser source (10 %). Surprisingly, a similar behavior is observed for the extracted relaxation times shown in Fig. 5.3.3(b). In contrast to intensity-independent relaxation times previously reported for fused silica [47] a strong increase of the decay time as a function of the excitation intensity is found. Here, the experimental uncertainty directly follows from the numerical fit.

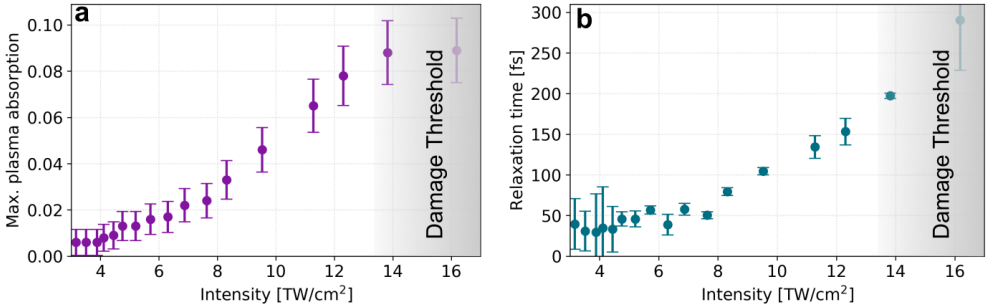

Fig. 5.3.3: Experimentally determined plasma absorption and relaxation time of the electron-hole plasma as a function of the pump laser intensity. **a**. Maximum absorption change of the probe laser pulse induced by the electron-hole plasma. **b**. Relaxation time of the electron-hole plasma obtained by applying exponential fit functions to the decay of the plasma absorption.

5.4 Discussion

The observation of a time-resolved transmission not converging towards its initial value as presented in Fig. 5.3.2 has been reported previously and is usually associated with a permanent structural modification of the irradiated target [241]. Since a non-zero absorption at large positive pump-probe delays is only observed at pump intensities above the threshold for laser-induced damage the presented results support this interpretation. Conversely, the observation of an intensity-dependent relaxation time of the electron-hole plasma in SiO_2 conflicts with previously reported experimental findings.

A large number of experimental studies have identified the formation of self-trapped excitons (STEs) as an important channel for plasma relaxation in fused silica [45, 47, 102]. According to the discussion of STEs in Sec. 2.2.4 an excited electron always traps with its parent hole in SiO_2. This leads to a trapping rate that is independent on the laser intensity, at variance with the results shown in Fig. 5.3.3(b). On the contrary, intensity-dependent trapping rates have been reported for other materials such as NaCl [254] indicating a trapping rate pro-

portional to the density of electron-hole pairs.
The outcome of the presented experiment displayed in Fig. 5.3.3(b) shows a clear increase of the relaxation time as a function of the excitation intensity. Although a full theoretical description rationalizing the observed behavior is still lacking, the discrepancy between the presented results and the current literature might be explained by a detrapping mechanism caused by vibrational activation of the medium.
Once the electron and the paired hole form an exciton and before self-trapping takes place, they occupy an energy state close to the conduction band of the material (see Fig. 2.2.12). After relaxation, the excitation energy level of the STE is approximately 2.8 eV [255]. Thus, the STE is energetically significantly closer to the edge of the conduction band than an unexcited carrier in the valence band. As a consequence, it is possible to excite carriers from STE states to the conduction band. The mechanism of exciton seeded multiphoton ionization in solid dielectrics has been observed by Grojo et al. [53]. Furthermore, the field-induced detrapping of electrons by electron-impact ionization has been demonstrated in semiconductors [122, 256]. Here, the observation of an intensity-dependent relaxation time is attributed to vibrational activation of the irradiated material caused by the energy that is stored in the quasi-free electron-hole plasma. The interaction of the accelerated conduction band electrons with the lattice leads to the generation of phonons. Thereby, energy is coupled from the laser-induced electron-hole plasma into vibrations of the lattice. The collective excitation of the crystal lattice might lead to an energy concentration in the vicinity of the laser-induced defect states and can potentially induce charge detrapping [257]. The liberation of trapped carriers by lattice vibrations hence also leads to a repopulation of the conduction band. Since the lattice vibrations survive even when the laser field is gone, vibrational detrapping can still occur without the presence of an electric field, thus effectively prolonging the measurable relaxation time. Concomitantly, the vibrational energy affects the probability for self-trapping of free carriers by changing the deformation potential. Since these two effects are correlated and a result of the same physical process they are experimentally indistinguishable with the presented method. As heating of the electron-hole plasma is predominantly governed by inverse Bremsstrahlung the mechanism of vibrational activation is considerably pronounced at longer excitation wavelengths. Therefore, the presented results do not contradict previously reported constant relaxation times that were found when using shorter wavelength laser pulses in the NIR and VIS spectral range for the generation of the electron-hole plasma.

Chapter 6

Origin of low-order harmonic generation in solid dielectrics

Since the first experimental realization in 2011 [188], HHG in solids has gained a tremendous amount of attention due to the promising strategies for probing attosecond carrier dynamics in solid state systems. Additionally, the high density of solid crystals compared to rare earth gases commonly used for HHG is expected to provide compact, ultrashort XUV and soft x-ray sources [207, 216, 221, 223, 225]. Hence, most of the experimental studies have recently focused on the generation of high-order harmonics in the UV and XUV spectral range [194, 201–203]. In these experiments, HHG in solids is mainly associated with interband transitions or oscillations of quasi-free carriers inside the energy bands of the crystal (intraband mechanism, see Secs. 3.2 and 3.3).
However, a pivotal mechanism governing the nonlinear response of solid dielectrics to intense ultrashort laser radiation has only received little attention in the past. This mechanism is associated with sub-cycle, i.e. attosecond dynamics of the promotion of electrons from the valence to the conduction band. Since strong-field ionization occurs on a timescale shorter than an optical cycle of the laser field it naturally leads to a nonlinear response. While the importance of sub-cycle ionization dynamics for harmonic generation has been described theoretically already in 1990 by F. Brunel [24] it has only been partially considered in the gas phase [25, 227] and almost completely overlooked in the context of solid state HHG [26].
In this chapter time-resolved experiments on two-color wave mixing in solid dielectrics are presented (Sec. 6.1). The contribution of the different HHG mechanisms - as described in Ch. 3 - is analyzed experimentally in Secs. 6.2 and 6.3. Furthermore, the order of the harmonic generation process leading to the detected emission is identified by exploiting the concept of the effective nonlinearity developed in a collaboration with researchers from the University of Rostock (Sec. 6.2). The experimental and numerical results are extensively

discussed in Sec. 6.4 and the main findings are summarized in Sec. 6.5.

6.1 Experimental results

Time-resolved detection of low-order harmonics To investigate the origin of low-order harmonics generated by a two-color field in bulk fused silica samples only the harmonics analysis part of the detection unit as presented in Fig. 4.2.2 (Harmonics analysis) is used. The intense MIR pump laser pulse generated by the OPA ($\lambda = 2.1\,\mu m$) is overlapped with the weak, time-delayed, cross-polarized NIR probe laser pulse ($\lambda = 796\,nm$) inside an a-SiO_2 sample. Low-order harmonic spectra generated by the two-color field are recorded with the UV/VIS spectrometer (wavelength range: 160 nm to 600 nm) as a function of the pump-probe delay τ, and using a delay interval of $\Delta\tau = 6.66\,fs$. Figure 6.1.1(a) shows a spectrogram obtained at a pump intensity of $12\,TW\,cm^{-2}$ and a probe intensity of $0.015\,TW\,cm^{-2}$ in the focal volume. An intense harmonic emission at frequencies given by

$$\omega_n = 2n \times \omega_{\text{pump}} + \omega_{\text{probe}}, \tag{6.1.1}$$

with $n = 1, 2, 3, 4$ is observed close to pump-probe overlap. Here, the overlap ($\tau = 0$) is defined by the maximum yield of the $n = 1$ harmonic. The expected central wavelengths of the harmonic orders according to Eq. 6.1.1 are indicated by the vertical dashed lines in Fig. 6.1.1(a).
Projecting the time-resolved spectrum on the wavelength axis [see Fig.6.1.1(b)] illustrates the strong decrease of the conversion efficiency with increasing harmonic order. A detection range of more than two orders of magnitude is necessary to clearly resolve the orders $n = 3$ & $n = 4$. Figure 6.1.1(c) shows the integrated signal of the time-frequency map shown in Fig. 6.1.1(a) on the delay axis. All four observed harmonic orders display an identical temporal signature that is significantly more confined in time than the linear convolution of the pump and the probe laser pulses. The rapid decrease of the conversion efficiency with harmonic order n qualitatively matches the expectations for a harmonic signal dominated by Kerr-type nonlinearities (see Sec. 3.1). On the contrary, the observed signal cannot result from a low-order perturbative process. Assuming a Kerr-type nonlinearity of the order $2\mathcal{N} + 1$, the temporal signature of the harmonic emission in a pump-probe configuration $I_{\text{exp}}(\tau)$ follows from

$$I_{\text{exp}}(\tau) = I_{\text{pump}}(t)^{2\mathcal{N}} \otimes I_{\text{probe}}(t - \tau). \tag{6.1.2}$$

Here $\otimes$ denotes the linear convolution operator. Approximating the observed temporal structure of the harmonics by the above equation using the pulse durations given in Sec. 4.3 and only allowing integer values of $\mathcal{N}$ reveals a nonlinearity of $2\mathcal{N} + 1 = 11$. Thus, the temporal signature of the observed harmonics indicates a much higher nonlinearity than the conventional Kerr-type

nonlinearity as a source of the detected emission. However, due to the fluctuations of the MIR pump laser pulse caused by the highly nonlinear mechanisms in the parametric generation and amplification process and the limited time-resolution in the experiment, this method only allows a rough estimate of the underlying nonlinearity.

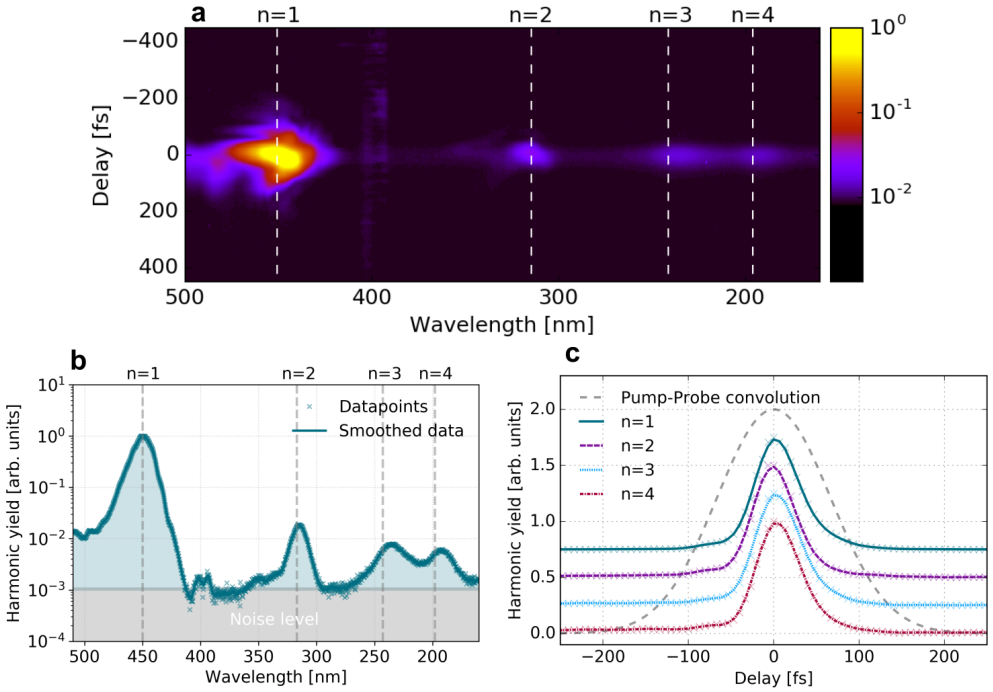

Fig. 6.1.1: Time-resolved measurement of two-color low-order wave mixing in amorphous fused silica. **a** Time- and spectrally-resolved low-order harmonic emission from the 0.5 mm thick fused silica sample excited by a strong 2.1 µm pump laser pulse ($I_{\mathrm{pump}} = 12\,\mathrm{TW\,cm^{-2}}$) and a weak 0.8 µm probe laser pulse ($I_{\mathrm{probe}} = 0.015\,\mathrm{TW\,cm^{-2}}$). **b**. Temporally integrated harmonic signal. **b** Spectrally integrated harmonic signal (experimental data for different harmonic orders are offset vertically for clarity) compared to the pump-probe convolution calculated with the help of the pump and probe pulse durations obtained in Sec. 4.3.

Pump intensity scans To further investigate the nonlinear generation process leading to the observed low-order harmonic emission, pump intensity scans are performed on the first harmonic order. By rotating the HWP in the probe beampath the polarization configuration is changed from perpendicular to parallel between two consecutive measurements. As a result, two individual pump intensity scans for the respective polarization schemes are presented in Fig. 6.1.2.

In both cases the pump intensity is increased to values above the critical intensity for irreversible modification of the fused silica sample indicated by the colored area on the right. The laser-induced damage threshold is identified by the observation of a strong scattering signal from the irradiated spot and subsequent visual inspection of the sample under a microscope. Each marker in Fig. 6.1.2 represents an individual datapoint obtained by acquiring a time-resolved spectrum at a particular pump intensity and a subsequent Gaussian fit to the resulting delay dependence of the $n = 1$ harmonic signal. The final harmonic yield is given by the peak value of the Gaussian fit function. In both (parallel and perpendicular) polarization configurations the resulting intensity dependence follows a quadratic behavior at low pump intensities as expected for a third order Kerr-type nonlinearity (corresponding to $\mathcal{N} = 1$ in Eq. 6.1.2). At $\approx 10\,\mathrm{TW\,cm^{-2}}$ the measured harmonic yield obtained with parallel polarizations significantly deviates from this scaling and displays a much higher nonlinear increase of the harmonic signal. In the case of the perpendicular pump and probe polarizations this departure from a perturbative, quadratic intensity scaling takes place only at pump intensities approaching the damage threshold of the target. Nevertheless, a threshold intensity for the departure from the quadratic scaling can still be determined as $\approx 11.5\,\mathrm{TW\,cm^{-2}}$. Hence, the presented pump intensity scans of the $n = 1$ harmonic yield suggest that at least in an intensity regime close to the damage threshold of the material a mechanism that is different from the optical Kerr-effect dominates the generation of low-order harmonics.

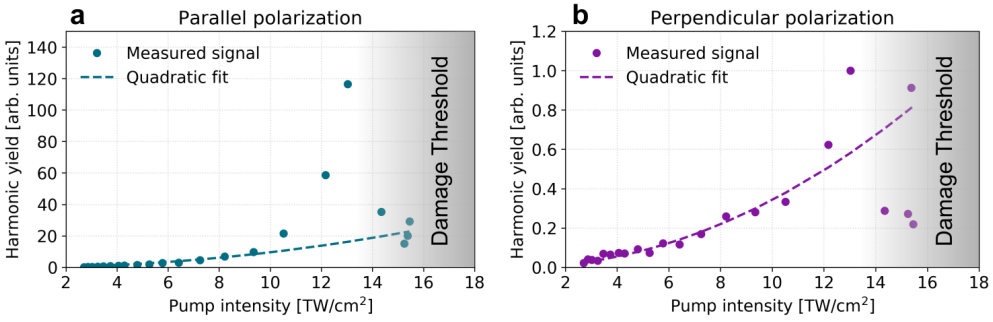

Fig. 6.1.2: Pump intensity scan of the n=1 harmonic in parallel (**a**) and perpendicular (**b**) polarization configuration, compared to numerical fits with a quadratic dependence on the intensity of the MIR pump laser pulse. Beyond approximately $10\,\mathrm{TW\,cm^{-2}}$ (parallel case) and $11.5\,\mathrm{TW\,cm^{-2}}$ (perpendicular case) the intensity dependence significantly deviates from the quadratic dependence that is expected for a Kerr-type process, suggesting a different origin for the observed harmonic.

Probe intensity scans While the dependence of the harmonic yield on the pump intensity is expected to reveal information on the number of pump photons involved in the generation process, a variation of the probe intensity while keeping the pump energy constant carries the same information for the weak NIR probe laser pulse. Results obtained by scanning the probe intensity and measuring the harmonic yield of the first four harmonic orders are presented in Fig. 6.1.3. All four measurements, performed simultaneously, display a linear dependence of the harmonic yield on the probe intensity. The linear scaling of the signal with the intensity of the probe laser pulse is elucidated by the included linear fits. The linear relationship between the harmonic yield and the probe intensity proves that only one probe photon is involved in the frequency mixing process as expected from Eq. 6.1.1.

Naturally, at higher probe intensities the situation becomes more complex.

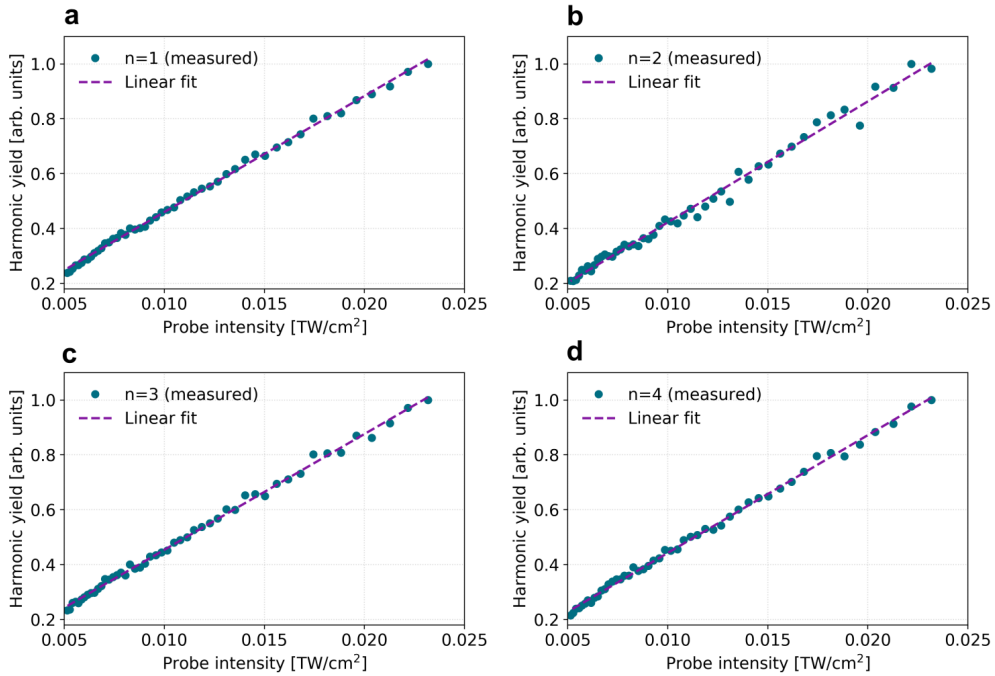

Fig. 6.1.3: Probe intensity scan of the first four harmonic orders at a fixed pump intensity of 12 TW cm^{-2} performed in a parallel polarization configuration.

Once the probe intensity is strong enough to induce nonlinear effects, harmonic emission at the frequency $\omega_{\mathrm{fwm}} = 2 \times \omega_{\mathrm{probe}} + \omega_{\mathrm{pump}}$ is observed [indicated by the orange line in Fig. 6.1.4(a)]. Thus, a further delay-dependent signal is generated close to the original $n = 2$ harmonic. Since two probe photons participate in the generation of this frequency a quadratic relationship between the strength of the harmonic emission and the intensity of the NIR probe laser pulse is observed, as displayed in Fig. 6.1.4(b). This scenario already becomes

relevant for probe intensities of 0.03 TW cm^{-2}. Since the pump intensity scan of the first harmonic order presented in Fig. 6.1.2 was performed at a probe intensity of 0.05 TW cm^{-2} the validity of this measurement needs to be confirmed by an additional measurement [1]. Figure 6.1.5 displays the $n = 1$ harmonic yield as a function of the probe laser intensity. Here the intensity of the probe laser pulse enters a regime where harmonic emission due to nonlinearities driven by the 800 nm pulse are observed (indicated by the colored area on the right side of Fig. 6.1.5). Still, an excellent agreement between the experimental data and a linear fit function is retained. Accordingly, the $n = 1$ harmonic yield still scales linearly with the probe intensity even in a range where frequency mixing involving more than one probe photon takes place. This additional investigation explicitly validates the results presented in Fig. 6.1.2.

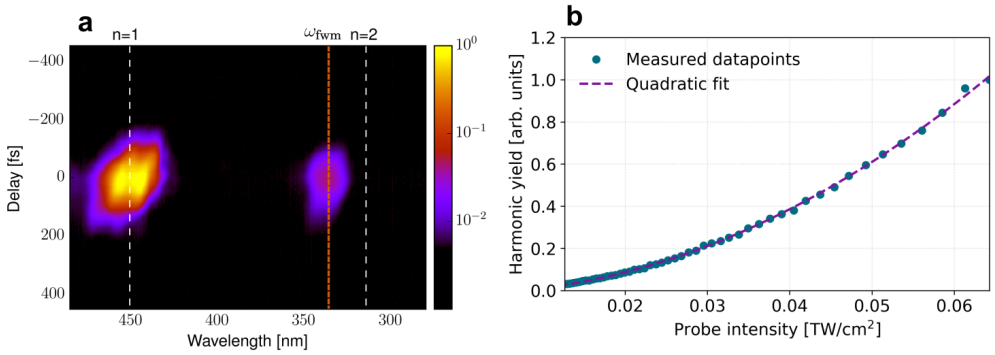

Fig. 6.1.4: Harmonic emission due to nonlinearities driven by the probe laser pulse. **a**. Time-resolved spectrum in the wavelength range where the original $n = 1$ and $n = 2$ harmonics are expected (see dashed lines). Due to frequency conversion containing two probe photons an additional harmonic peak is observed at a wavelength of $\approx$ 335 nm (see orange line). **b**. Harmonic yield of the signal detected at 335 nm as a function of the probe laser intensity.

Polarization studies In order to characterize the resulting polarization state of the generated harmonic radiation a polarization filter can be inserted in front of the VIS/UV spectrometer (see Fig. 4.2.2). Figure 6.1.6 shows the transmission of the pump and probe laser pulses and the $n = 1$ harmonic through a linear polarization filter as a function of the polarizer angle. The polarization of the $n = 1$ harmonic clearly follows the polarization of the probe laser pulse and is to a very good approximation perpendicular to the pump laser polarization.

In their work on time-resolved detection of ionization-induced low-order wave

[1] Due to the tedious procedure of the full pump intensity scan measurement (measurement time of $\geq$ 30 hrs. with the above parameters) it was not possible to repeat the whole measurement at a lower probe intensity.

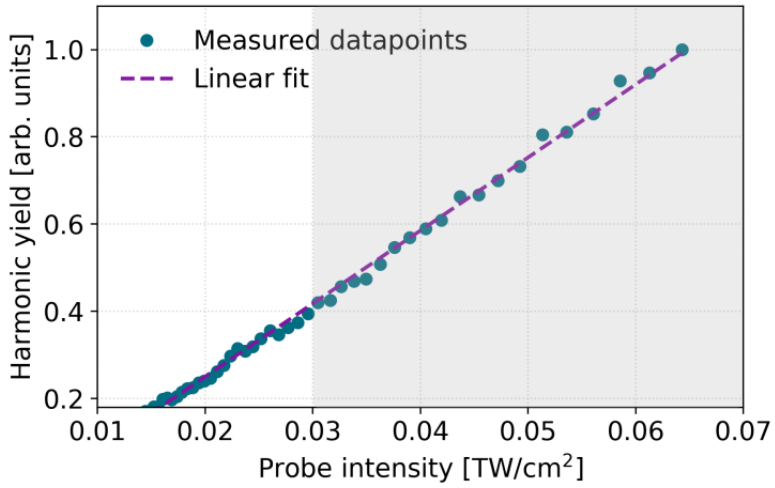

Fig. 6.1.5: Probe intensity scan of the first harmonic order detected at ≈450 nm at a fixed pump intensity of 12 TW cm^{-2} performed in a parallel polarization configuration.

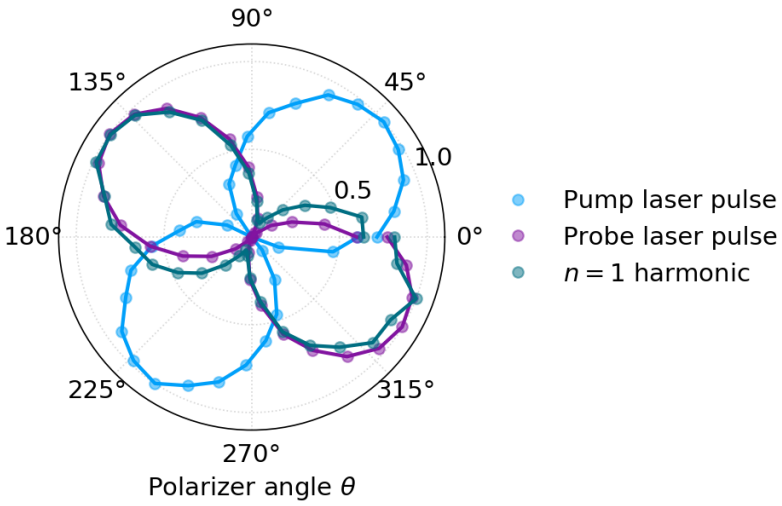

Fig. 6.1.6: Transmission of the pump and probe laser pulses and of the first harmonic order through a linear polarization filter as a function of the polarizer angle θ.

mixing in fused silica, Mitrofanov and coworkers used a circularly polarized pump laser pulse in order to demonstrate the dependence of the harmonic emission on the presence of attosecond ionization dynamics [26]. For a circularly polarized excitation pulse, the stepwise increase of the plasma density is converted into a smooth increase of the conduction band population that lacks any sub-cycle dependence. Since harmonic generation due to the nonlinearity of SFI relies on the sub-cycle variations of the plasma density (see Fig. 3.4.1) no SFI-induced harmonics are produced when using circularly polarized excitation pulses. Experimental results obtained with circularly polarized pump laser pulses are presented in Fig. 6.1.7. Circular polarization of the MIR pump laser pulse is achieved by inserting a tunable zero-order quarter-waveplate ($\lambda/4$ plate) in front of the off-axis parabolic mirror. The obtained ellipticity of $\mathcal{E} = 0.98$ is characterized by measuring the transmission through a polarization filter as a function of the polarizer angle θ [see Fig. 6.1.7(b)]. Subsequently, the yield of the $n = 1$ harmonic is compared for linear and circular pump polarization (here, linear polarization denotes perpendicular pump and probe polarizations) as a function of the MIR pump laser pulse intensity. Strikingly, a strong attenuation of the harmonic emission is only observed for rather high peak intensities (e. g. $I_0 \geq 7.5\,\mathrm{TW\,cm^{-2}}$ for $Y_{\mathrm{circ}}/Y_{\mathrm{lin}} \leq 0.1$). Conversely, at intensities below this threshold, the harmonic yield obtained with circularly polarized pump laser pulses reaches comparable values to the linear polarized case. A strong attenuation of the generated harmonics is only expected if SFI governs the generation of the detected emission. Hence, the dominance of SFI is only indicated for pump intensities $\gtrsim 7.5\,\mathrm{TW\,cm^{-2}}$.

However, a clear identification of the nonlinearity dominating the low-order

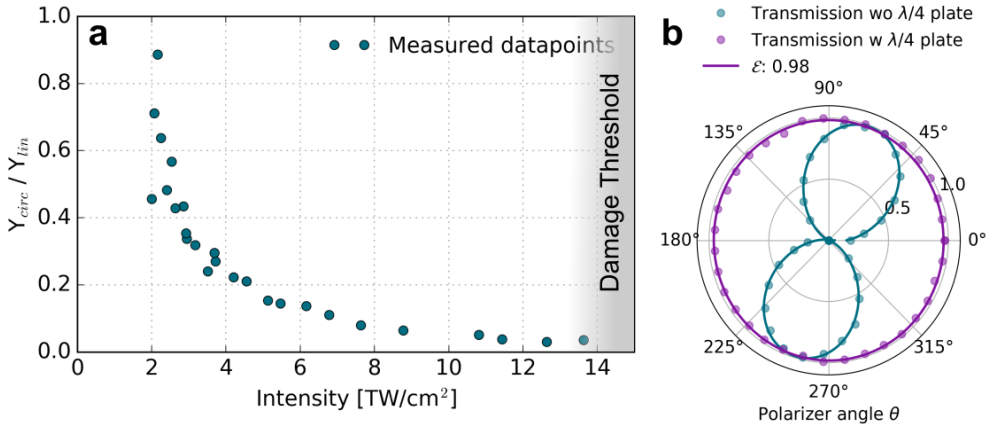

Fig. 6.1.7: **a**. Ratio of the $n = 1$ harmonic yield obtained with circular (Y_{circ}) and linear (Y_{lin}) polarized MIR pump laser pulses. **b**. Linear and circular polarization of the pump laser pulse characterized by the angle-resolved transmission through a polarization filter.

harmonic emission at intensities close to the damage threshold of the irradiated

samples is still lacking. Therefore, a procedure based on the concept of the effective nonlinearity is introduced in the following section. The effective nonlinearity enables the unambiguous determination of the nonlinearity leading to the observed harmonic emission.

6.2 The effective nonlinearity

A reliable and precise method to determine the effective nonlinearity of the mechanism underlying the harmonic generation was developed in a collaboration with researchers from the University of Rostock[2]. Results of this collaboration are also presented in [258]. According to this formalism the leading term of an m^{th} order nonlinear process in an isotropic medium is of the general form

$$\mathbf{P} \propto (\mathbf{E} \cdot \mathbf{E})^{\mu} \mathbf{E}. \tag{6.2.1}$$

The order of the nonlinear process is given by $m = 2\mu + 1$. The key idea, proven in Ref. [258], is that the nonlinearity order can be directly measured experimentally by comparing the signal observed in parallel and perpendicular polarization configurations in a pump-probe experiment using linearly polarized pump and probe laser pulses. Assuming a strong pump laser pulse that excites the nonlinearity in the target and a weak probe laser pulse, the effective nonlinearity of the process generating the detected signal can be obtained via

$$\sqrt{\frac{Y_{||}}{Y_{\perp}}} = 2\mu + 1 = m. \tag{6.2.2}$$

Generally, any harmonic emission process can be characterized in terms of the order of a corresponding perturbative process using the proposed method.

Following this procedure the effective nonlinearity of the generation process can be obtained by measuring the ratio of the $n = 1$ harmonic yield in parallel and perpendicular polarization configuration. Results from such an analysis using the experimental results that were already shown in Fig. 6.1.2 are compared to numerical simulations[3] for an assumed bandgap of 7.5 eV and 7.7 eV[4] in Fig. 6.2.1. The relative error of 20 % on the experimental determination of the effective nonlinearity is determined by a 10-fold repetition of the time-resolved measurement under identical experimental conditions. Generally, the theoretical prediction is in good qualitative agreement with the experimentally acquired data and shows that experiment and theory agree about the fact that from about 9 TW cm^{-2} onwards the effective nonlinearity is substantially higher than the

[2] Prof. Dr. T. Fennel, Dr. C. Peltz, B. Liewehr, B. Kruse.

[3] Simulations performed by T. F., C. P., B. L. and B. K.

[4] DUV/VUV spectralphotometric measurements of the bandgap of the used SiO_2 samples performed by Dr. M. Jupé at the Laser Zentrum Hannover e.V. led to a determination of bandgap values of 7.7 eV for the samples used in these experiments.

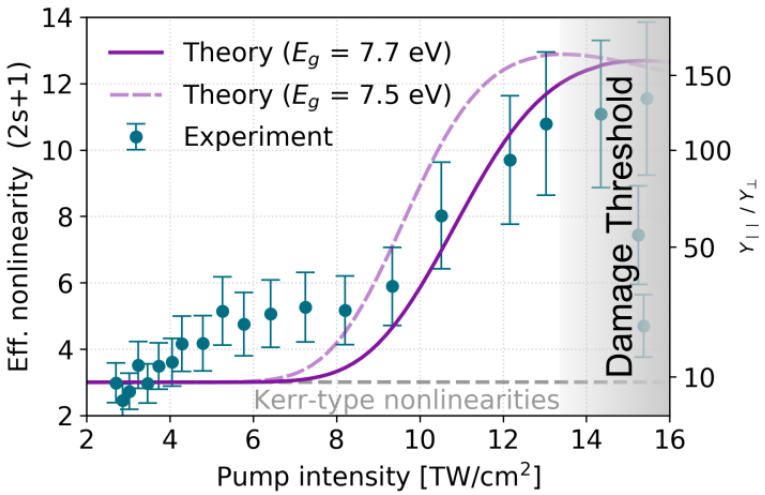

Fig. 6.2.1: Ratio of the $n = 1$ harmonic yield obtained in parallel and perpendicular polarization configuration as a function of the pump laser pulse intensity together with the resulting effective nonlinearity according to Eq. 6.2.2.

effective nonlinearity that would be predicted for a Kerr-type process. The earlier departure from the ratio corresponding to Kerr-type nonlinearities (indicated by the horizontal dashed line) in the experimental case possibly results from the onset of self-focusing (see Sec. 2.1.1) leading to a higher effective intensity in the focal plane caused by nonlinear propagation effects that are currently not implemented in the numerical simulation or may indicate contributions from higher order (i.e. 5th order) Kerr-type nonlinearities to the experiment in this intensity range up to 8 TW cm^{-2}. Nevertheless, the slope of the intensity-dependent increase of the effective nonlinearity as well as the maximum effective nonlinearity reached are comparable in both experiment and theory. Due to the time-consuming experimental procedure to obtain the effective nonlinearity of a given harmonic order as a function of the pump intensity, the measurement is only carried out at a single pump intensity for the $n = 2$ harmonic. Figure 6.2.2 displays an effective nonlinearity of 10.9 for the $n = 2$ harmonic obtained at a pump intensity of 11.5 TW cm^{-2}. Considering the relative error of 20 % no significant difference between the $n = 1$ and the $n = 2$ harmonic is found.

Based on the presented experimental results in combination with the determination of the effective nonlinearity it can be concluded that Kerr-type nonlinearities are not the dominant source of the observed low-order harmonic generation in fused silica at excitation intensities close to the damage threshold of the samples. Instead, a further mechanism of significantly higher nonlinear order governs the harmonic emission in this particular intensity regime.

The second source of HHG in solids described in Ch. 3 is based on the recollision

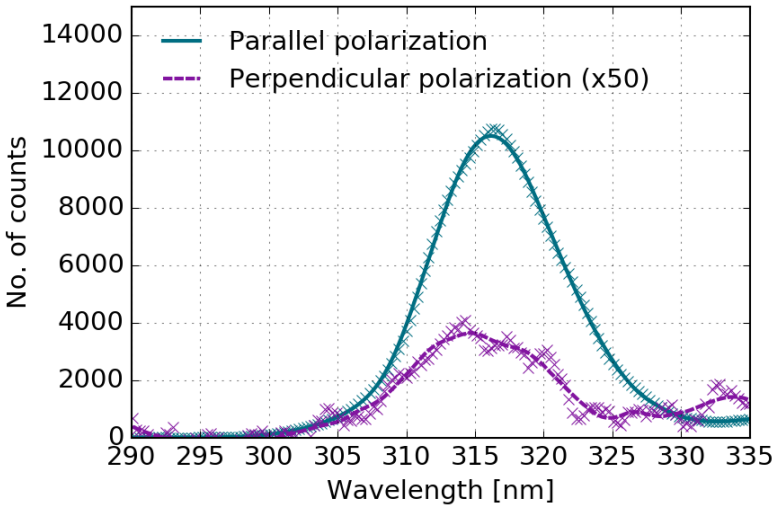

Fig. 6.2.2: $n = 2$ harmonic spectrum obtained in parallel and perpendicular polarization configurations at a pump intensity of $11.5\,\mathrm{TW\,cm^{-2}}$. The spectrum detected for perpendicular polarizations is multiplied by a factor of 50 for readability, i.e. the actual measured intensity ratio between the two spectra is ≈ 119 ($m = 10.9$).

of excited electrons with their accompanying holes in strong analogy with the three-step model for gaseous and atomic-like HHG. In the presented experiments only low-order harmonics with a maximum photon energy of approximately 6.8 eV are detected. Since the bandgap of the a-SiO_2 samples is measured to be 7.7 eV, only below-the-bandgap harmonics are detected. In the case of recollision type harmonics excited electrons are driven away from the point of their initial interband transition (SFI) and recollide at higher k-values which is generally associated with a larger energy gap (see Sec. 3.2). Hence, only above-the-bandgap harmonics are generated by the interband mechanism and recollision type harmonics can be excluded as the dominant source of the detected harmonics in the presented experiment.
Therefore, only the intraband mechanism (see Sec. 3.3) remains - apart from SFI - as a possible source of the observed harmonic emission.

6.3 Experiments in crystalline samples - on the intraband contribution to low-order harmonic generation

In order to study the possible contribution of intraband harmonic generation and thus, the influence of an anharmonic band structure on the detected harmonics,

experiments are performed in Y-cut crystalline quartz samples (CrysTec SiO_2 (10-10)K). Since the intraband mechanism relies on the oscillation of quasi-free carriers in nonparabolic energy bands (see Sec. 3.3) the orientation dependence of the harmonic yield is expected to reflect the structural anisotropy of the crystal [188, 190, 195, 201, 215]. Therefore, the $n = 1$ harmonic yield is shown as a function of the relative orientation between the optical axis of the crystal and the polarization axis of the MIR pump laser pulse for an excitation intensity of $4\,\mathrm{TW\,cm^{-2}}$ in Fig. 6.3.1(a) and for $12\,\mathrm{TW\,cm^{-2}}$ in Fig. 6.3.1(b). To characterize the crystal orientation, the second harmonic of the probe laser pulse (centered around $\approx 400\,\mathrm{nm}$) is acquired simultaneously which exhibits the pronounced dependence on crystal orientation that is characteristic for a Y-cut crystal. A transition from an orientation-dependent signal at $4\,\mathrm{TW\,cm^{-2}}$ to an isotropic response at $12\,\mathrm{TW\,cm^{-2}}$ is observed. A comparison with the results presented in Fig. 6.2.1 indicates that at a MIR intensity of $4\,\mathrm{TW\,cm^{-2}}$ the wave mixing process is dominated by the Kerr-type nonlinearity. Therefore, a dependence of the conversion efficiency on the crystal orientation reflecting the anisotropy of the nonlinear optical susceptibility is expected. At an intensity of $12\,\mathrm{TW\,cm^{-2}}$ this orientation dependence is no longer observed. Instead, the detected harmonic yield shows no dependence on the orientation of the crystalline sample with respect to the polarization of the incident laser pulse. Hence, the acceleration of free carriers within their respective anharmonic bands can be excluded as a dominant source of the observed harmonic radiation.

Based on the chain of reasoning presented above all possible mechanisms for the generation of the observed low-order harmonic emission except for the ionization related nonlinearity have been excluded. Thus, it can be concluded that the detected radiation is indeed a direct optical signature of strong-field ionization, transferring attosecond, sub-cycle ionization dynamics into the frequency domain.

6.4 Discussion

According to Ch. 3 the only remaining nonlinearity leading to the formation of harmonic radiation is based on the sub-cycle modulations of the intraband current density first predicted by F. Brunel in 1990 [24]. The generation of Brunel harmonics has already been described in detail in Sec. 3.4. However, theoretical work performed by our collaborators identified three contributions to the locally induced plasma current density (see also [258]). The time-derivative of the total plasma current density reads:

$$\frac{\partial j(t)}{\partial t} = q_e \left(\frac{q_e}{m_e} E(t)\rho(t) + v_0 \frac{\partial \rho(t)}{\partial t} + \frac{\partial}{\partial t} \left\{ x_0 \frac{\partial \rho(t)}{\partial t} \right\} \right). \tag{6.4.1}$$

Here, v_0 denotes the carrier birth velocity and x_0 the spatial coordinate of the tunneling exit. Equation 6.4.1 shows that besides the well-known Brunel

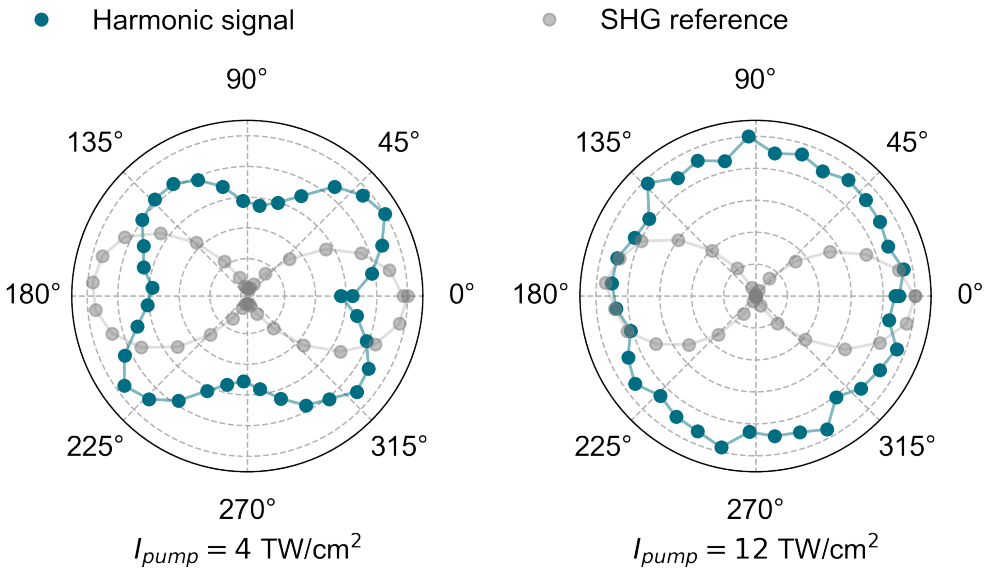

Fig. 6.3.1: $n = 1$ harmonic yield depending on the orientation of a Y-cut α-quartz crystal. The simultaneously measured second harmonic signal of the 800 nm probe laser pulse is added as a reference that indicates the crystal orientation. The results are obtained for perpendicular pump and probe polarizations and a pump intensity of **a** 4 TW cm^{-2} and **b** 12 TW cm^{-2}.

contribution (corresponding to the first of the three terms that are shown in brackets) two further terms have to be considered. The second term depends on the birth velocity of the electrons in the conduction band and can be neglected due to the modest photon energies used in the experiments. The last term of Eq. 6.4.1 describes a current density variation resulting from the transport of the electrons across the bandgap (i.e. direct SFI). This ionization current is directly related to the conservation of energy during the excitation process. It corresponds to the energy extracted from the laser field to fuel the interband transition of an electron. The energy conservation is furthermore associated with a spatial displacement of the electron wavepacket x_0 given by

$$x_0 = \frac{E_g}{q_e E}. \tag{6.4.2}$$

While the ionization current has been routinely considered to fulfill the conservation of energy it has so far been neglected in the context of HHG in solids. Figure 6.4.1 once again summarizes the different mechanisms of harmonic generation in solids and links the experimental results presented in this chapter to the considerations presented in Sec. 3. Apart from harmonic generation due to Kerr-type nonlinearities (Sec. 3.1), harmonics can be generated by the interband (see Sec. 3.2) and the intraband mechanism (see Sec. 3.3). While the Brunel harmonics as a result of the stepwise increase of the plasma density have been discussed in Sec. 3.4 a second mechanism for the generation of low-order harmonics that is also associated with sub-cycle ionization dynamics - namely the ionization current - has been identified.

An experimental discrimination between harmonic radiation generated by the

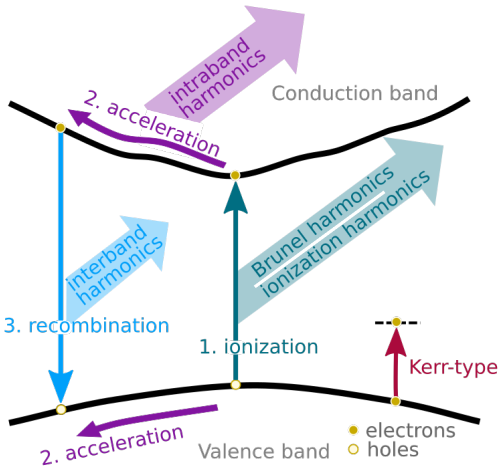

Fig. 6.4.1: Schematic description of harmonic generation in solids. Each of the depicted mechanisms is associated with nonlinearities that lead to the emission of harmonics and compete with the perturbative Kerr-type contributions.

Brunel and the ionization current is extremely challenging since the only characteristic difference between the two mechanisms is the resulting relative phase of the generated harmonics with respect to the driving field. Since this phase is not accessible in the current experimental setup, we cannot determine experimentally which of the two mechanisms dominates the generation of the detected signal. Numerical results provided by our collaborators from the University of Rostock however show that the harmonic signal generated by the ionization current is generally much stronger than the Brunel harmonic signal [see Fig. 6.4.2]. Accordingly, the harmonic signal generated by the ionization current dominates over the Kerr-type wave mixing contribution at significantly smaller intensities than the Brunel mechanism and is the leading mechanism responsible for the observations reported in this chapter.

Because of the numerical simulations and the presented experimental obser-

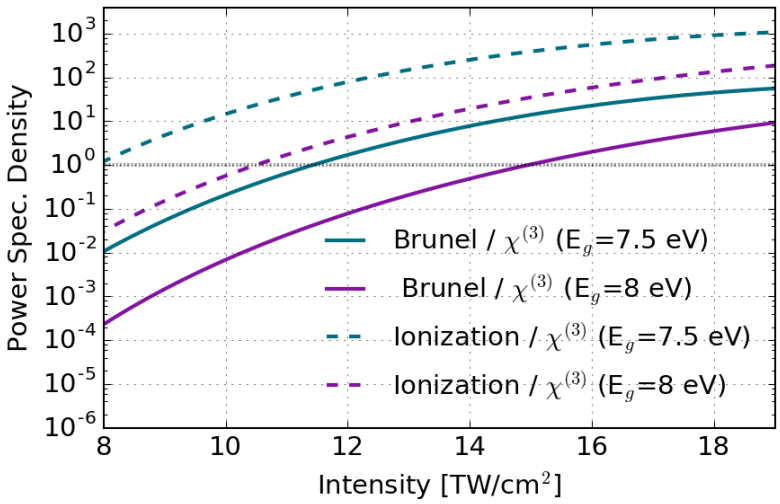

Fig. 6.4.2: Numerical simulation of the $n = 1$ harmonic yield as a function of the MIR pump laser pulse intensity. Harmonic emission due to the Brunel and ionization current are compared to the Kerr-type nonlinearity. Results obtained by our theory collaborators from the University of Rostock.

vations it can be concluded that low-order harmonics generated in a two-color pump-probe experiment in fused silica are dominated by the nonlinearity of the ionization current that reflects the transport of the electrons through the classically forbidden region and that was hitherto essentially overlooked in the context of harmonic generation in solids. The presented findings complement the picture of harmonic generation in solids with a new mechanism for low-order harmonic generation in the strong-field regime.

6.5 Summary

In conclusion, experimental results on two-color wave mixing in amorphous fused silica have been discussed in this chapter. Time-resolved detection of low-order harmonics in a close-to-collinear, cross-polarized pump-probe configuration using a MIR pump and a NIR probe laser pulse has been analyzed regarding the underlying nonlinear process. Careful investigations of the temporal signature, the pump and probe intensity dependence and the relative strength of the harmonic emission in parallel and perpendicular polarization configurations enabled the exclusion of Kerr-type nonlinearities as a dominant source of the observed emission for intensities close to the damage threshold of the samples. Performing experiments in crystalline quartz samples and demonstrating that the observed harmonic emission does not depend on the structural anisotropy of the crystal furthermore ruled out the intraband mechanism as a possible source of the detected signal. The interband mechanism could be excluded due to the low photon energies of the observed harmonics. Hence, the conclusion was reached that attosecond dynamics of strong-field ionization are responsible for the observed generation of low-order harmonics in fused silica.
Due to the combination of experimental and theoretical results and the excellent agreement between both, a mechanism previously overlooked in the context of HHG in solids - the ionization current - could be identified as the dominant source of nonlinearity leading to the formation of low-order harmonics in strongly excited fused silica. Furthermore, it was established that harmonic emission due to the ionization current generally dominates harmonic emission generated by the conventional Brunel current.

Chapter 7

Phase matching of low-order harmonic generation

In the course of chapter 6 the source of low-order harmonic generation in strongly excited fused silica was identified as the ionization current resulting from strong-field ionization of electrons from the valence to the conduction band. Moreover, the prevalence of the ionization current over the conventional Brunel current was evidenced with the help of numerical simulations. However, only the local response of the irradiated target to the two-color irradiation was considered up to this point. This chapter is dedicated to the influence of propagation and the corresponding phase matching condition enabling an efficient wave mixing process leading to the generation of measurable quantities of low-order harmonics. In Sec. 7.1 the fundamentals of phase matching are discussed. Section 7.2 contains experimental results on two-color wave mixing in gold-coated fused silica samples. The influence of the tilting angle of the irradiated target with respect to the incoming laser pulses is experimentally analyzed in Sec. 7.3. Finally, Sec. 7.4 contains experimental results on imaging of the harmonic emission in the far field, before the chapter is summarized in Sec. 7.5. Remarkably, a significant enhancement of the harmonic yield is observed in gold-coated samples and attributed to a self quasi-phase matching mechanism.

7.1 Introduction to phase matching

Whenever an intense electromagnetic field propagates through a nonlinear medium the nonlinear polarization $\mathbf{P}^{\mathrm{NL}}$ leads to the generation of photons with an energy that equals an even and/or odd multiple of the fundamental photon energy. In general the efficiency of such a frequency conversion process [such as second harmonic generation (SHG), third harmonic generation (THG) or four-wave mixing (FWM)] depends on the overlap of the field that generates the new

electric field and the generated field itself. During the propagation through the nonlinear medium photons are converted from the fundamental to the newly generated frequency. As a consequence the intensity of the incident field decreases while the strength of the generated field increases. Besides energy conservation determining the energy of the photons contained in the generated field also the conservation of momentum has an important impact on the frequency conversion process. In an optimal case the difference between the sum of the wave vectors of the incoming and generated fields is zero [29]:

$$\Delta\mathbf{k} = \mathbf{k}_{\text{generated}} - \mathbf{k}_{\text{fundamental}} = 0. \tag{7.1.1}$$

In the more complex case of two driving fields that are combined to generate a harmonic field (e.g. via FWM) the corresponding phase mismatch $\Delta\mathbf{k}$ is given by

$$\Delta\mathbf{k} = (n\mathbf{k}_1 + m\mathbf{k}_2) - \mathbf{k}_{\text{signal}}. \tag{7.1.2}$$

Here $\mathbf{k}_1$ and $\mathbf{k}_2$ denote the wave vectors of the two incident fields while $\mathbf{k}_{\text{signal}}$ describes the wave vector of the generated field. n and m are the number of photons taken from the two input fields. Only when the phase mismatch is close to zero, constructive interference leads to a continuous buildup of the harmonic signal. The length over which the fundamental and the harmonic field exhibit a phase shift of π is called the coherence length L_c and is given by

$$L_c = \frac{\pi}{\Delta k}. \tag{7.1.3}$$

Thus, a large phase mismatch leads to a short coherence length. Therefore, only low conversion efficiencies are expected for non-phase matched frequency mixing processes.

7.2 Experiments in gold-coated samples

Up to now only the local nonlinear response has been considered when comparing the numerical results to experimental data. This led to the conclusion that the ionization current is the dominant source of harmonic emission in the scenario discussed in Ch. 6. However, a more accurate description of the low-order harmonic generation processes requires the inclusion of nonlinear pulse propagation effects in a three-dimensional model. Though a full (3+1)-dimensional treatment is currently not available due to limitations of the computing capabilities, numerical results of the generated harmonic field including one-dimensional propagation are displayed in Fig. 7.2.1.

Generally, a wavevector mismatch leads to an oscillating field amplitude of the generated wave with propagation distance due to alternating constructive and destructive interference. Thus, the oscillations of the harmonic signal during propagation through the target indicate a non-phase matched process. According

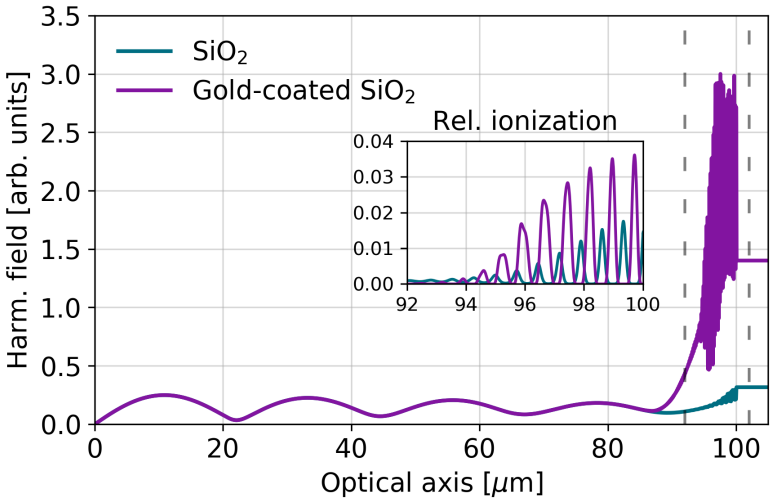

Fig. 7.2.1: Numerical simulation of two-color wave mixing in fused silica. Comparison of the $n = 1$ harmonic yield upon propagation in 100 µm fused silica with an uncoated and a gold-coated rear surface.

Wavelength λ [nm]	Refractive index n	Wave vector k [μm^{-1}]
2100 (pump)	1.4366	4.298
800 (probe)	1.4533	11.414
454.05 ($n = 1$)	1.4653	20.276
316.98 ($n = 2$)	1.4834	29.405
243.48 ($n = 3$)	1.5118	38.997
197.65 ($n = 4$)	1.5538	49.393
166.34 ($n = 5$)	1.6232	61.315

Table 7.2.1: Refractive indices and resulting wave vectors for the used pump and probe wavelengths as well as the harmonic wavelengths of the first five harmonic orders. Refractive index values are taken from Ref. [32].

to the theoretical considerations given in Sec. 7.1 this indicates a coherence length that is shorter than the thickness of the sample. The refractive indices and the corresponding wave vectors for the first five harmonic orders in fused silica are summarized in Tab 7.2.1. The phase mismatch Δk_n of the respective harmonic order n can be calculated by (see Eq. 7.1.1)

$$\Delta k_n = (2nk_{\text{pump}} + k_{\text{probe}}) - k_n, \tag{7.2.1}$$

with k_{pump} and k_{probe} being the wave vectors of the fundamental pump and probe wavelength and k_n the wave vector of the n-th harmonic. Table 7.2.2 summarizes the phase mismatches and the corresponding coherence lengths (calculated according to Eq. 7.1.3) for the first five harmonic orders. As indicated by the results shown in Fig. 7.2.1 the coherence length is indeed much shorter than the sample thickness (500 µm) for the $n = 1$ harmonic and even shorter for higher harmonic orders. Consequently, the observed emission is the result of phase matching over the last coherence length only. Still, the generated signal is sufficiently strong to allow the detection of the radiation generated by a single pair of pump and probe laser pulses. A more detailed analysis of the numerical results reveals that the majority of the harmonic signal is generated close to the rear surface of the target (see Fig. 7.2.1). As demonstrated in the inset of Fig. 7.2.1 also the ionization of the sample significantly increases close to the rear surface while displaying a periodic modulation. The enhanced ionization and harmonic generation can be traced back to a quasi-stationary wave that is formed due to the back reflection of the pump laser electric field on the rear surface (interface located at a propagation length of 100 µm in Fig. 7.2.1). The coherent superposition of the incoming and

Wavelength λ [nm]	Phase mismatch $\lvert\Delta k\rvert$ [μm^{-1}]	Coherence length L_c [μm]
454.05 ($n = 1$)	0.266	11.81
316.98 ($n = 2$)	0.799	3.93
243.48 ($n = 3$)	1.795	1.75
197.65 ($n = 4$)	3.595	0.874
166.34 ($n = 5$)	6.921	0.454

Table 7.2.2: Phase mismatch Δk and coherence length L_c for the first five harmonic orders.

the reflected electric field of the pump laser pulse leads to the formation of a standing wave, and hence, a periodic plasma grating - similar to the observations presented in [259] where a periodic structure of laser-induced modifications close to the exit surface of a glass sample was attributed to the interference of two superimposed counterpropagating electromagnetic fields - potentially affecting the phase matching condition. To further investigate this quasi-phase matching effect induced by the formation of a quasi-stationary wave, the same simulation

was performed with a thin (25 nm) gold layer added on the rear surface of the 100 µm SiO_2 sample. Since the gold coating significantly increases the reflectivity of the rear surface for the MIR pump laser field, the effect already observed in the uncoated sample is substantially increased (see purple line in Fig. 7.2.1).

For an experimental verification of the predicted quasi-phase matching mechanism UV-grade fused silica samples with a partially gold-coated (film thickness $d \approx 25\,\mathrm{nm}$) surface are prepared[1]. The sample is mounted on a computer-controlled translation stage and is only partially coated (see sketch in Fig. 7.2.2). Therefore, the emission from a coated area of the sample can directly be compared to the harmonic yield obtained from an uncoated region of the substrate. Figure 7.2.2 displays the harmonic yield that is detected from a coated area of the a-SiO_2 sample normalized with respect to the signal obtained from an uncoated part of the substrate. In the case of a gold-coated rear surface a clear enhancement of the $n = 1$ harmonic emission is found up to pump laser intensities of $\approx 4.6\,\mathrm{TW\,cm^{-2}}$. The same measurement is performed with a gold coating applied to the front surface of the sample. The coated front surface leads to a strong attenuation of the observed wave mixing signal. The laser-induced damage threshold (LIDT) of the gold coating, which is naturally much lower than that of the fused silica, is indicated by the colored area in Fig. 7.2.2. At excitation intensities above the LIDT of the coating the normalized yield of the $n = 1$ harmonic converges towards unity in both discussed cases. Since a damaged or even ablated coating has no effect on the reflectivity of the rear surface anymore the harmonic yield is no longer affected.

For a profound analysis of a possible enhancement of the harmonic emission in

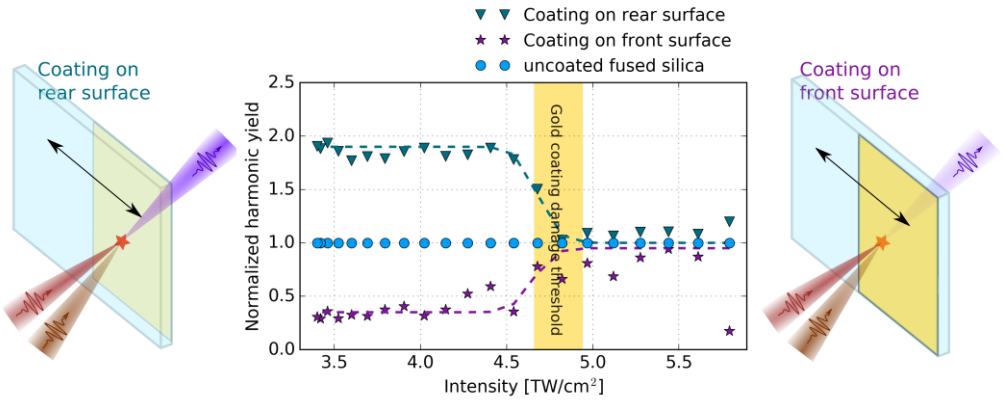

Fig. 7.2.2: Normalized $n = 1$ harmonic yield as a function of the MIR pump laser intensity without accounting for the reduced transmission through the gold coating.

[1]The gold-coated fused silica samples were provided by Dr. D. Engel from the Max-Born-Institute, Berlin

the gold coated samples, a characterization of the gold coating transmission at the $n = 1$ harmonic wavelength is required. In order to determine the transmission of the applied coating at exactly the desired wavelength, the first harmonic order is generated in a pristine fused silica sample. Subsequently, the gold coated sample is inserted into the beam path of the harmonic radiation in front of the UV/VIS spectrometer. Comparison of the two measurements exposes the transmission of the thin gold layer.

Figure 7.2.3(a) shows the $n = 1$ harmonic spectrum acquired with an uncoated

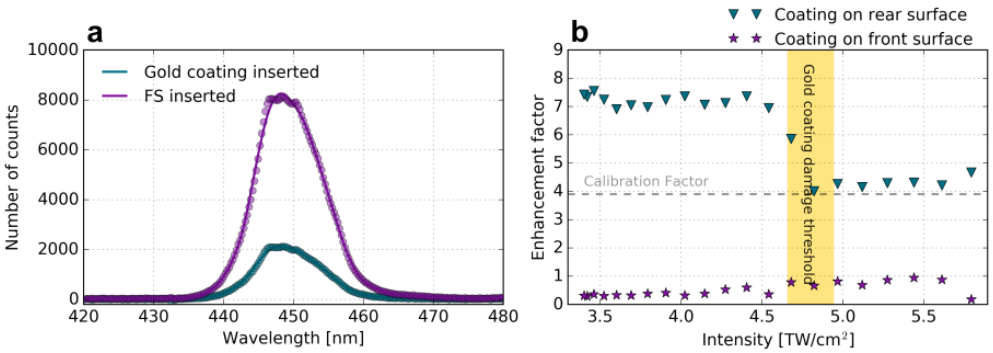

Fig. 7.2.3: Experimental results obtained with gold-coated fused silica samples. **a**. $n = 1$ harmonic spectrum with a gold-coated and an uncoated sample inserted into the harmonic beampath as measured by the UV/VIS spectrometer. **b**. Resulting effective enhancement factors of the $n = 1$ harmonic yield obtained with a gold coating on the rear and on the front surface, as a function of the MIR pump laser intensity.

and a gold-coated sample inserted into the beam path of the harmonic signal. The transmission at the $n = 1$ harmonic wavelength is evaluated to be $\approx 25.64\,\%$. Taking the reduced transmission of the thin gold layer into account the harmonic signal generated in coated and uncoated SiO_2 samples from Fig. 7.2.2 can be compared in order to analyze a potential enhancement of the harmonic generation. The resulting enhancement factor obtained with the gold coating on the rear and on the front surface is shown in Fig. 7.2.3(b). Up to the LIDT the effective enhancement factor is evaluated to be nearly independent on the pump intensity at a value of ≈ 7 with a gold coating on the rear surface. Conversely, the harmonic emission is significantly suppressed when the gold coating is applied on the front surface of the sample.

Strikingly, the signal is not as severely reduced as expected. Instead, the normalized harmonic yield still reaches $\approx 25\,\%$ of the signal in the uncoated case (without taking the reduced transmission of the thin gold layer into account). The reflectivity of the gold coating for the 2.1 µm pump laser pulse is experimentally evaluated to 80 %. Accordingly, a much stronger decrease of the harmonic signal should result. One possibility to rationalize this observation is that a non-negligible

fraction of the detected harmonic radiation is generated within the thin gold film. Especially for Kerr-type nonlinearities this seems reasonable because the third-order nonlinear susceptibility of gold ($\chi^{(3)}_{\mathrm{Au}} \approx 1.82 \times 10^{-15}\,\mathrm{m^2\,V^{-2}}$ [260]) is up to seven orders of magnitude higher than that of SiO_2 ($\chi^{(3)}_{\mathrm{SiO_2}} \approx 1.6 \times 10^{-22}\,\mathrm{m^2\,V^{-2}}$ [261]). The remaining signal observed with a gold coating on the front surface of the fused silica sample might be generated by Kerr-type four-wave mixing inside the gold coating. Nevertheless, it is still possible to extract the effective enhancement of harmonic emission from the bulk SiO_2 target by subtracting the signal acquired with a coating on the front surface from the harmonic yield obtained with a coated rear surface. Results of this procedure are presented in Fig. 7.2.4. As expected the correction for additional wave mixing inside the gold coating reduces the enhancement factor. Still, a considerable increase of the detected harmonic signal is found with a higher reflectivity of the rear surface. The effective enhancement factor of the two-color wave mixing signal is evaluated to values between 5 and 6 for MIR laser intensities below the LIDT of the gold coating.
A further comparison of the experiments performed with the gold-coated samples and the study of the effective nonlinearity presented in Fig. 6.2.1 reveals that at the intensities where the experiments with the gold-coated samples were performed, i.e. at intensities below the damage threshold of the gold coating, harmonic generation due to SFI is not the dominant process. Instead the measurements and calculations of the effective nonlinearity in this intensity range indicate that the experiments with the gold-coated samples can only be performed under conditions where Kerr-type nonlinearities govern the harmonic emission. Hence, the experiments performed with the gold-coated samples demonstrate that an increased rear surface reflectivity influences the conversion efficiency for a Kerr-type wave mixing process. Generally, though, SFI-induced harmonics should obey the same phase matching condition (assuming a negligible influence of the plasma on the phase matching). Due to the higher nonlinearity of SFI compared to Kerr-type four-wave mixing an improved phase matching should even result in a much stronger enhancement of the harmonic signal. Nevertheless, an experimental verification demonstrating the influence of the quasi-stationary wave forming close to the rear surface of the sample on the phase matching of SFI-induced harmonic generation still needs to be performed. Further experimental studies presented in the following section also indicate a non-trivial phase matching condition potentially verifying the theoretically predicted strong impact of the rearside reflectivity on the harmonic conversion efficiency.

7.3 Influence of the sample tilting angle

Further experiments are performed to provide a more detailed understanding of the phase matching mechanism in low-order harmonic generation in solid dielectrics. To begin with, the $n = 1$ harmonic yield is measured as a function of

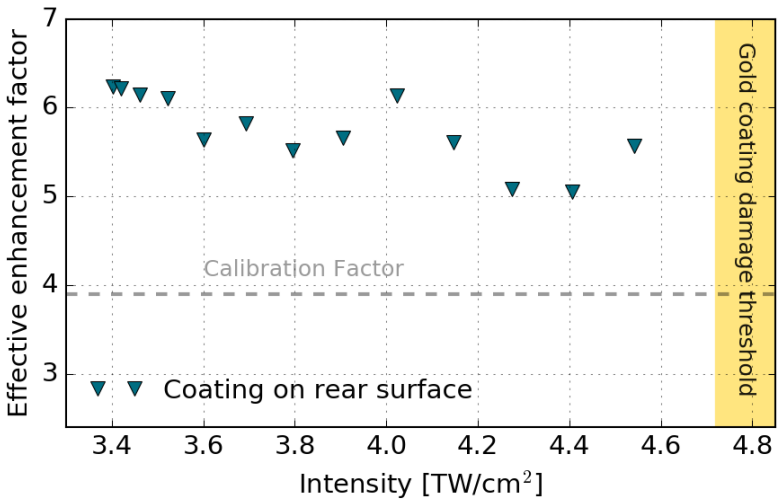

Fig. 7.2.4: Effective enhancement of the $n = 1$ harmonic yield with a gold-coated rear surface after subtracting the signal generated within the coating.

the tilting angle ϕ of the fused silica sample with respect to the MIR pump laser pulse. Normal incidence ($\phi = 0$) is determined by adjusting the back reflection of the laser diode radiation from the sample as described in Sec. 4.2. Results obtained at a pump intensity of $\approx 11.5\,\mathrm{TW\,cm^{-2}}$ are presented in Fig. 7.3.1. A double-peaked structure can be observed with a first peak at $\phi \approx 0°$, a second maximum at an tilting angle of $\phi \approx 4°$ and a minimum in between. The double-peaked structure is approximated by a numerical fit consisting of the sum of two lorentzian functions given by [72]:

$$Y(\phi) = A_1 \left(1 + \frac{4}{1+\sqrt{2}} \left\{\frac{x - x_1}{w_1}\right\}^2\right)^{-2} + A_2 \left(1 + \frac{4}{1+\sqrt{2}} \left\{\frac{x - x_2}{w_2}\right\}^2\right)^{-2}. \tag{7.3.1}$$

Here, A_1 and A_2 are the amplitudes, x_1 and x_2 the central positions and w_1 and w_2 the width of the peaks. According to the numerical analysis the first maximum is reached at a tilting angle of $\phi = -0.56°$ and the second maximum is located at an angle of $\phi = 3.75°$. A possible interpretation of this fitting procedure is the precise determination of the pump-probe angle that is otherwise difficult to access experimentally. While the angle corresponding to the first maximum in Fig. 7.3.1 is reasonably close to the angle for normal incidence of the pump laser beam the angle corresponding to the second maximum identifies the angle of incidence of the probe laser beam on the SiO_2 sample. The observed dependence of the generated signal strength on the tilting angle of the sample can not be explained by only considering forward propagating wave vectors. In

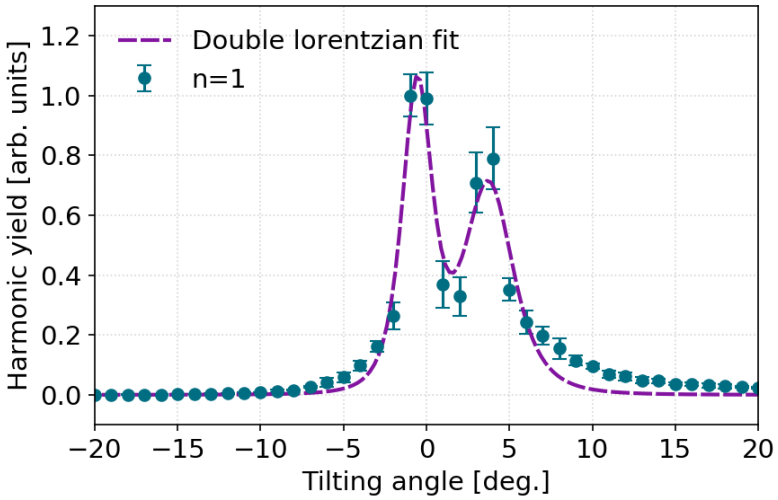

Fig. 7.3.1: Yield of the $n = 1$ harmonic order as a function of the tilting angle of the fused silica sample compared to a numerical fit according to Eq. 7.3.1.

fact, if the reflectivity of the rear surface would not play a role for the phase matching process no (or only a weak) dependence of the harmonic signal on the tilting angle would result.

For normal incidence of the MIR pump laser pulse the overlap between the incident and the reflected wave is optimized [see Fig. 7.3.2(a)]. Hence, the resulting improvement of the phase matching condition by the quasi-stationary grating, that was discussed in the previous section, is maximized. For a tilting angle matching the pump-probe angle, the resulting grating induced by the intense pump laser pulse is formed perpendicular to the propagation direction of the probe laser pulse [see Fig. 7.3.2(b)]. Accordingly, the wave vector associated with the grating - $\mathbf{k}_{\text{grating}}$ - is parallel to $\mathbf{k}_{\text{probe}}$. Whenever $\mathbf{k}_{\text{grating}}$ is parallel either to $\mathbf{k}_{\text{pump}}$ or $\mathbf{k}_{\text{probe}}$ efficient quasi-phase matching results in a significant enhancement of the $n = 1$ harmonic emission.

7.4 Frequency-resolved spatial imaging

A second set of experiments to investigate the influence of phase matching on the generation of harmonics due to SFI is based on spatial imaging of the generated harmonic radiation. Contrary to the presented experimental setup in Fig. 4.2.1 the fused silica sample is not mounted on a translation stage anymore. Instead it remains in a fixed position while an iris of 100 µm diameter is mounted on the x-y translational stage at a certain distance Δ (between 2 and 5 cm) behind the

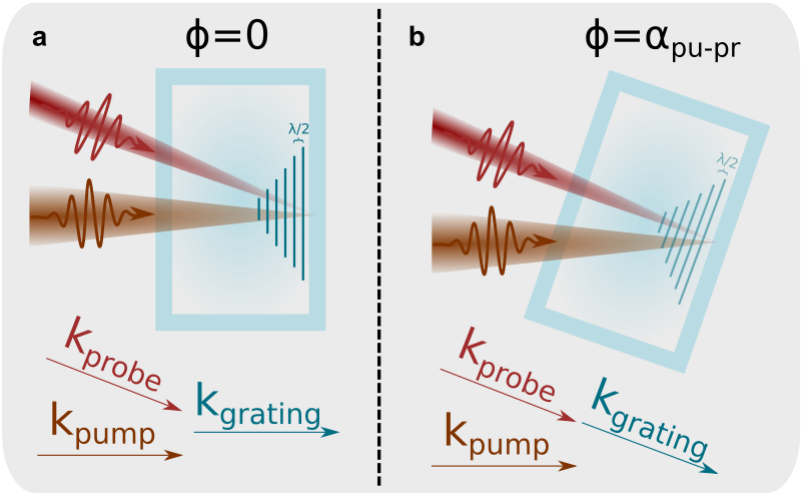

Fig. 7.3.2: Sketch of the influence of the tilting angle of the sample on the formation of a quasi-stationary grating and the subsequent phase matching condition.

sample (see Fig. 7.4.1).

Constantly generating harmonics in the sample while scanning the pinhole and

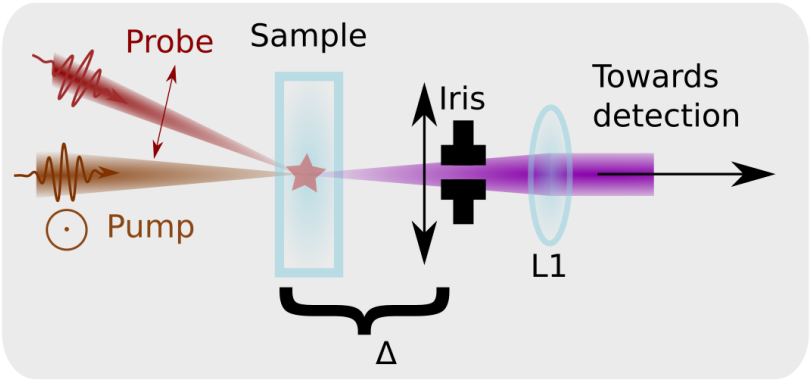

Fig. 7.4.1: Experimental setup utilized to image the emission direction of the $n = 1$ harmonic with respect to the fundamental pump and probe laser pulses.

measuring pump, probe and harmonic spectra at each position of the iris reveals the spatial structure of the harmonic emission with respect to the generating pump and probe laser fields. Experimental results obtained at a distance of 2 and 3 cm between the sample and the iris are presented in Fig. 7.4.2. Here the zero-point of the horizontal and vertical positions only serves as an arbitrary reference and is not the same for the measurements at $\Delta = 2$ cm (Fig. 7.4.2**a**, **b**, **c**) and $\Delta = 3$ cm (Fig. 7.4.2**d**, **e**, **f**).

By analyzing the center of gravity of the two-dimensional maps the respective

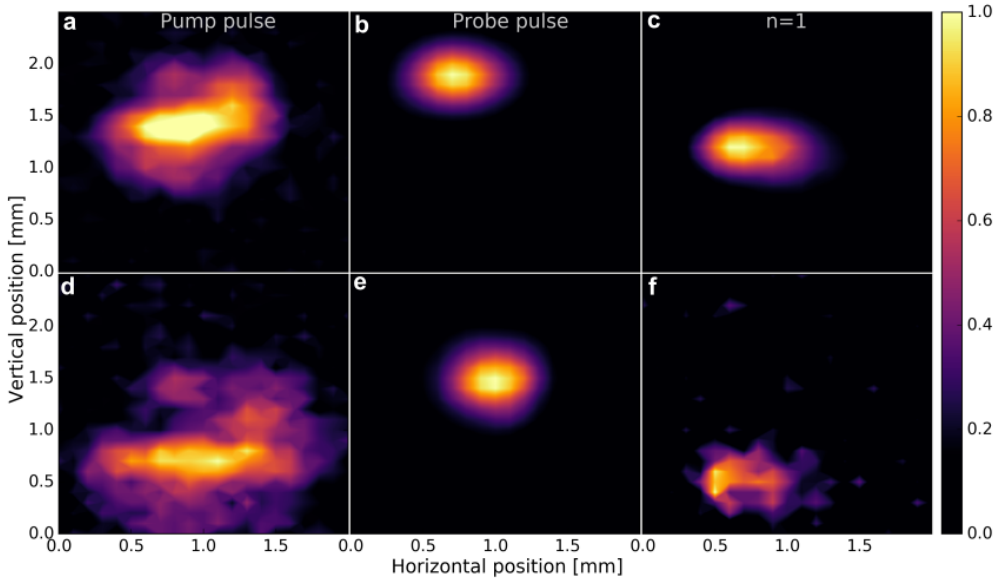

Fig. 7.4.2: Frequency-resolved spatial imaging of the frequencies escaping the fused silica sample. **a**, **b** & **c**. Spatial profile of the pump, probe and first harmonic at a distance of 2 cm from the sample. **d**, **e** & **f**. Same at a distance of 3 cm from the sample. Note that the coordinate system in **a**, **b** and **c** is independent of that in **d**, **e** and **f**.

position of the pump, probe and $n = 1$ beams at a given distance from the sample can be extracted.

Figure 7.4.3 displays the resulting central positions obtained from the measure-

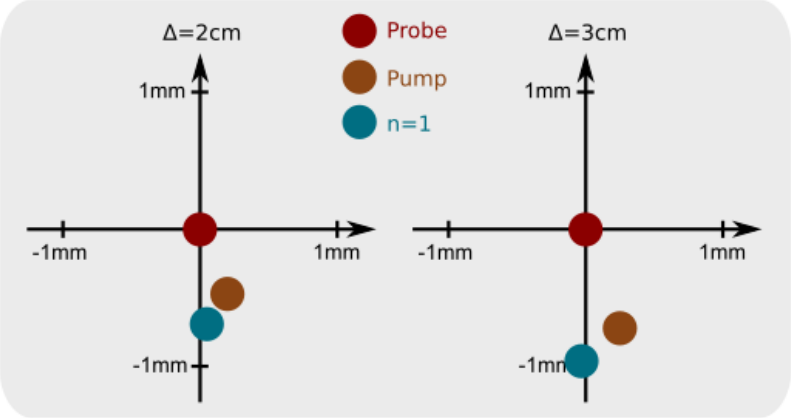

Fig. 7.4.3: Central positions of the pump, probe and $n = 1$ harmonic beams at a distance of $\Delta = 2\,\text{cm}$ and $3\,\text{cm}$, respectively.

ment shown in Fig. 7.4.2. Strikingly, the $n = 1$ harmonic beam propagates outside of the cone formed by the pump and probe laser beam. Due to restrictions on the momentum conservation this behavior is not possible for a conventional phase matching condition where the k-vector of the generated signal always propagates within the cone formed by wave vectors of the two generating, forward propagating fields. Hence, the frequency-resolved spatial imaging of the pump, probe and harmonic radiation further supports the hypothesis of a non-conventional phase matching process underlying the observed harmonic generation.

7.5 Discussion

In this chapter, experimental investigations regarding the phase matching of low-order harmonic generation driven by a two-color laser field in fused silica have been presented. Based on numerical results taking into account the propagation of the pump and probe laser fields through the SiO_2 sample the importance of the rear surface reflectivity was examined. Two-color wave mixing experiments performed with gold-coated fused silica samples showed that indeed an increased reflectivity of the rear surface enhances the strength of the harmonic radiation emerging from the sample. The presence of a non-conventional phase matching condition was further underpinned by the observed strong dependence of the $n = 1$ harmonic yield on the tilting angle of the sample with respect to the MIR pump laser pulse. Finally, it was demonstrated that the generated harmonic emission propagates outside of the cone formed by the wave vectors of the incoming pump and probe laser pulse unequivocally verifying a non-conventional

underlying phase matching process.
In conclusion, the entirety of the presented experimental results indicate that a novel self-quasi-phase matching process based on reflection of the strong MIR pump laser pulse on the rear surface of the SiO_2 sample enhances the emission of low-order wave mixing signals in a two-color configuration. The quasi-stationary grating that is formed in the proximity of the exit surface of the sample can only be attributed to the strong MIR laser pulse as the NIR probe laser pulse is too weak to significantly modify the optical properties of the substrate.

Chapter 8

Linking harmonic generation and plasma formation in laser-driven solids

The previous two chapters discussed the generation of low-order harmonics from a two-color field in amorphous fused silica. A combination of experimental and numerical results was exploited to demonstrate a relation between the detected harmonic radiation and strong-field ionization driven by the intense MIR pump laser pulse. While Ch. 6 and 7 only used the harmonics analysis part of the detection unit, the experiments presented in Ch. 5 were solely acquired with the help of the probe analysis part (see Fig. 4.2.2) and enabled the isolation of the carrier dynamics induced by the strong 2.1 µm pulse in the SiO_2 samples.
The present chapter aims at combining the results simultaneously acquired in both parts of the detection unit. The gained knowledge is used to link the generation of low-order harmonics to the dynamics of plasma formation. This chapter consists of two parts. The first section is dedicated to the reconstruction of the strong-field induced plasma formation with an unprecedented time-resolution with the help of a phase-retrieval algorithm. The second section discusses a strategy to reveal the relative role of SFI and IMP in the ultrafast plasma density buildup in laser excited solids.

8.1 Real-time plasma formation in solid dielectrics

8.1.1 Introduction

In Ch. 5 a time-resolved measurement of the transmission of a weak probe laser pulse through an excited fused silica sample was analyzed to uncover the

formation and relaxation dynamics of the electron-hole plasma generated within the irradiated target. The limited time-resolution due to the duration of the probe laser pulses of 45 fs inhibits the detection of phenomena occurring on shorter timescales. Generally, it is challenging to study sub-cycle ionization dynamics based on observations in the temporal domain. Only extremely short pulses with pulse durations on the order of attoseconds provide a sufficient time resolution. However, attosecond pulses are only available in a spectral range where solid dielectrics such as fused silica are strongly absorbing. Hence, it is not feasible to study ultrafast electron dynamics in bulk solids by using attosecond pulses. Still, several compelling experimental studies have demonstrated the occurrence of attosecond ionization dynamics in bulk solids [23, 26, 64, 128]. In this section the detection of the optical signature of SFI in the frequency domain is used to determine the temporal evolution of the plasma density solely induced by photoionization.

8.1.2 Data processing

Figure 8.1.1 displays a time-resolved spectrum containing the first three orders of harmonics according to equation 6.1.1. The spectra are generated by a mid-IR pump laser pulse of 2400 nm central wavelength at a peak intensity of $12\,\mathrm{TW\,cm^{-2}}$. The delay-independent artefacts around a wavelength of 266 nm are attributed to third-harmonic generation of the NIR probe laser pulse in the fused silica sample. While the $n = 1$ and the $n = 2$ harmonic signal are both centered around the expected wavelength (indicated by the dashed lines in Fig. 8.1.1), the $n = 3$ harmonic appears slightly blueshifted. However, the observed discrepancy between the theoretically expected and the measured central wavelength of the third harmonic order do not influence the analysis presented below. According to the description presented in Sec. 3.4, the time-frequency map containing the low-order harmonics is described by

$$I_{\mathrm{exp}}(\omega,\tau) = \left| \int \frac{\partial j(t,\tau)}{\partial t} e^{-i\omega t} dt \right|^2 \tag{8.1.1}$$

with $\partial j(t)/\partial t$ being the time-derivative of the total plasma current density (see Eq. 6.4.1). Under the assumption that the Brunel contribution dominates the total plasma current density and therefore also the generation of low-order harmonics, Eq. 8.1.1 can be rewritten as

$$I_{\mathrm{exp}}(\omega,\tau) = \left| \int \rho(t) E_{\mathrm{pr}}(t-\tau) e^{-i\omega t} dt \right|^2 . \tag{8.1.2}$$

Due to the limited bandwidth of the spectrometer used in the experiments (160 nm to 600 nm), only a restricted part of the generated response in the frequency domain is detected. Hence, the low-frequency, DC component (see cycle-averaged

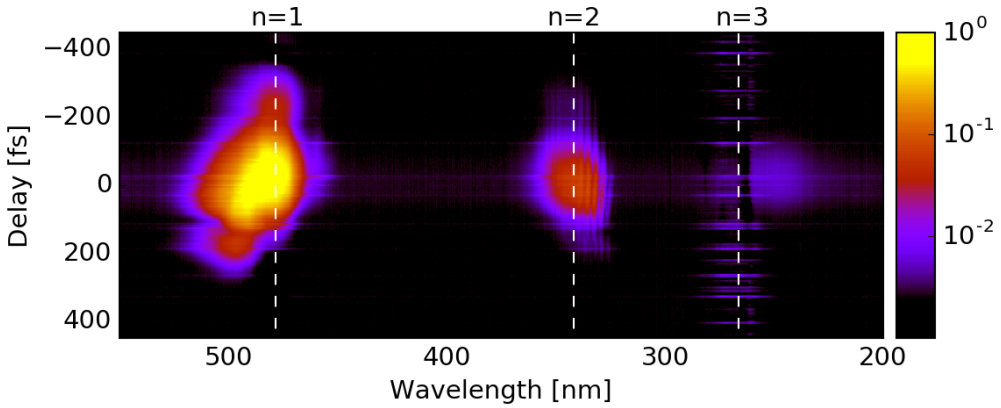

Fig. 8.1.1: Time-resolved harmonic spectrum resulting from two-color irradiation of amorphous fused silica at 2.4 µm and 796 nm, sampled with an interval of 3.3 fs. The dotted lines represent the expected positions of the first three harmonic orders.

component in Fig. 3.4.1) arising from the cycle-averaged $\rho_{\mathrm{ca}}(t)$ introduced in Sec. 3.4 does not affect the time-resolved spectrum shown in Fig. 8.1.1. The total plasma density $\rho(t)$ in Eq. 8.1.2 can therefore be replaced by $\rho_{\mathrm{sub}}(t)$ introduced in Sec. 3.4 (corresponding to the part of $\rho(t)$ that varies on sub-cycle timescales). The quantity measured by the spectrometer is therefore given by:

$$I_{\mathrm{exp}}(\omega,\tau) = \left| \int \rho_{\mathrm{sub}}(t) E_{\mathrm{pr}}(t-\tau) e^{-i\omega t} dt \right|^2 . \tag{8.1.3}$$

Equation 8.1.3 is of the same form as the expression describing the measured signal in a cross-correlation frequency-resolved optical gating (FROG) measurement [262–264]. Since only the magnitude and not the phase of the low-order harmonics can be acquired, the signal represented by Eq. 8.1.3 constitutes a typical phase retrieval problem [265]. Thus, an iterative algorithm enables the reconstruction of the unknown quantity $\rho_{\mathrm{sub}}(t)$ representing the sub-cycle variations of the plasma density. Owing to its robustness, time-domain ptychography [266] constitutes an appealing methodology. The analog of the diffraction spectrum used in conventional ptychographic experiments is, in the presented experiment, $I_{\mathrm{exp}}(\omega,\tau)$ and the object to reconstruct is $\rho_{\mathrm{sub}}(t)$. The results provided by a ptychographic iterative engine (PIE) [267, 268] after 1000 iterations are presented in Fig. 8.1.2[1]. The retrieved time-resolved spectrum displayed in Fig. 8.1.2(a) accurately reproduces the spectral features of the experimental spectrogram. Figure 8.1.2(b) shows the spectral intensity of the retrieved unknown quantity. Strong peaks, appearing at even multiples of the mid-IR pump laser frequency

[1]The ptychographic analysis was performed by Dr. Tobias Witting from the Max-Born-Institute, Berlin.

(indicated by the vertical dashed lines), can be observed. The reconstructed function is shown as a function of time in Fig. 8.1.2(c). It takes the form of the product of a rapidly oscillating function with a periodicity corresponding to half the optical period of the mid-IR pump laser pulse with a slowly varying envelope (see dashed line).

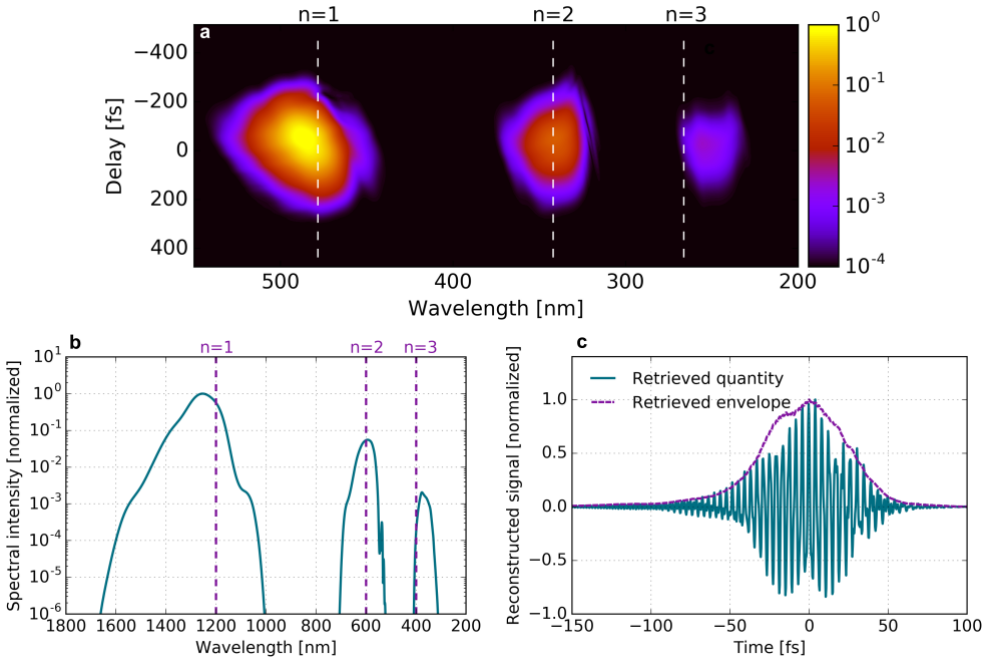

Fig. 8.1.2: Results for the reconstruction of strong-field driven plasma dynamics from the time-resolved detection of two-color low-order wave mixing signals governed by the Brunel mechanism. **a**. Time-resolved harmonic spectrum retrieved by the PIE. **b**. Spectral intensity of the reconstructed field. **c**. Temporal profile of the reconstructed signal ($\rho_{\mathrm{sub}}(t)$).

8.1.3 Discussion

As already mentioned above, in a scenario where the nonlinear Brunel current dominates all other nonlinearities leading to the generation of low-order harmonics, the iterative algorithm directly provides access to the sub-cycle variations of the plasma density due to SFI. Results obtained under the assumption that the Brunel contribution dominates all other nonlinearities leading to harmonic emission at the observed frequencies are presented in Fig. 8.1.3. To obtain the total plasma formation due to SFI the reconstructed signal as shown in Fig. 8.1.2(c) is analyzed. While the rapidly oscillating function contains the information on the high-frequency component of the plasma density buildup $\rho_{\mathrm{sub}}(t)$, the envelope of

the retrieved signal enables the reconstruction of the cycle-averaged evolution of the plasma formation driven by SFI. As demonstrated in [269], the delay dependence of all harmonic orders is identical. Hence, the temporal profile of a single harmonic contains sufficient information to extract the temporal profile of the cycle-averaged plasma density buildup due to SFI. Thus, direct integration of the retrieved envelope yields the cycle-averaged temporal evolution of the plasma density while adding the oscillating function to the integrated envelope enables the reconstruction of the total plasma formation due to SFI. The obtained result as presented in Fig. 8.1.3 generally shows a good agreement with the numerical result obtained using the experimental parameters and the model discussed in Sec. 2.2.6. The colored area around the extracted result for $\rho_{\mathrm{SFI}}(t)$ represents the uncertainty of the reconstruction that amounts to one optical cycle of the driving field ($\approx 8\,\mathrm{fs}$). As a result of the limited bandwidth of the pump and probe laser pulses the generated harmonic orders do not spectrally interfere (see Figs. 8.1.1 and 6.1.1(a)). Therefore, the relative phase between the different harmonic orders remains obscure. For the reconstruction of the sub-cycle variations of the plasma density it is assumed that all harmonic orders are emitted in phase which is in agreement with the theoretical prediction. Furthermore, with the presented algorithm and the given experimental parameters it is not possible to determine the relative phase between the MIR excitation laser pulse and the emitted harmonic radiation due to the lacking carrier envelope phase stabilization.

As extensively investigated in Ch. 6 the nonlinear Brunel current is *NOT*

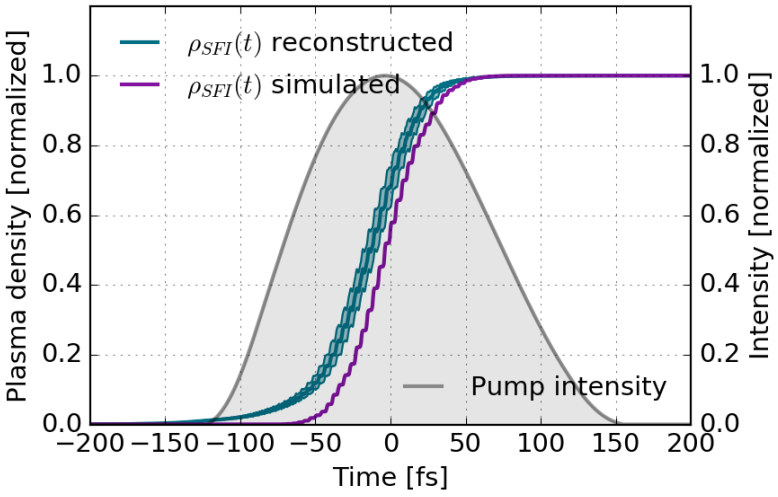

Fig. 8.1.3: Temporal profile of the plasma density buildup due to SFI reconstructed from the result of the iterative phase retrieval algorithm.

the dominating source of low-order harmonic emission from strongly excited SiO_2 samples. Instead, it was demonstrated that the ionization current governs the generation of low-order harmonics at pump intensities close to the damage

threshold of the irradiated target. Hence, the analysis presented above is not directly applicable to the low-order harmonic spectra acquired under the given experimental conditions. Nevertheless, the measured quantity can still be expressed in an equation similar to Eq. 8.1.2. Replacing the Brunel current by the ionization current according to Eq. 6.4.1 gives

$$I_{\mathrm{exp}}(\omega,\tau) = \left| \int \frac{\partial}{\partial t} \left\{ x_0 \frac{\partial \rho(t,\tau)}{\partial t} \right\} \exp(-i\omega t) dt \right|^2 . \tag{8.1.4}$$

Hence, using a PIE to analyze the time-resolved spectrum containing ionization harmonics still reveals intimate information on the nonlinear current associated with SFI. The extraction of the sub-cycle plasma dynamics induced by SFI from a time-resolved measurement of low-order harmonics generated by the ionization current however remains an open challenge up to date.

8.2 Revealing the relative importance of strong-field and electron-impact ionization in ultrafast laser-induced plasma formation in solid dielectrics

8.2.1 Introduction

The relative contribution of direct laser-induced strong-field ionization and indirect electron-impact ionization to the formation of an electron-hole plasma in solids is a subject of intense research since several decades [22, 28, 49, 50, 77, 112, 116, 270]. Since both mechanisms lead to partially intrapulse dynamics of the conduction band electron density, a direct disentanglement of the two processes based on time-domain experiments is extremely challenging. Hence, this chapter describes an experimental technique enabling the determination of the relative role of the two major excitation mechanisms. By combining the characterization of the total plasma density via time-resolved transmission measurements with detection of the optical signature of SFI in the frequency domain, the temporal evolution of the plasma density due to SFI can be decoupled from the dynamics of the total plasma density. Before applying this strategy on experimental results presented in Ch. 5 and Ch. 6 a numerical analysis of the relative contribution of SFI and IMP is discussed.

8.2.2 Numerical simulations

As stated in Sec. 2.2.5 the strong-field-driven carrier dynamics in solid dielectrics can be approximated by a single rate equation (see Eq. 2.2.36). A numerical solution of the SRE is illustrated in Fig. 8.2.1(a) for an incident pulse of 150 fs

FWHM pulse duration, a central wavelength of 2100 nm and a peak intensity of 15 TW cm^{-2}. While the implementation of all three terms from Eq. 2.2.36 clearly leads to a surpassing of the critical plasma density indicated by the dashed horizontal line, the maximum plasma density stays far below the critical density if electron-impact ionization is neglected. Thus, under the chosen conditions, surpassing the critical plasma density is mainly driven by IMP, which relies on seed electrons provided by SFI to induce an avalanche effect of excited quasi-free carriers in the conduction band. The influence of plasma relaxation becomes obvious when comparing the resulting plasma density taking only SFI or taking both SFI and relaxation into account [see blue and purple curves in Fig. 8.2.1(a)]. Due to the assumption of a single exponential decay a linear decrease of the plasma density can be observed in a semi-logarithmic representation once the laser intensity falls below the ionization threshold. The SFI and IMP rates leading to this plasma formation presented in Fig. 8.2.1(a) are shown in Fig. 8.2.1(b). Here, the SFI rate is multiplied by a factor of 500 to show both rates on the same scale. Clearly, IMP is the dominant ionization mechanisms under the given conditions. Hence the corresponding impact ionization rate is much stronger than the SFI rate. Apparently the two time-dependent ionization rates only slightly overlap in time since a sufficient number of seed electrons generated by SFI is required to efficiently trigger IMP. The relative delay of the IMP rate with respect to the SFI rate might indicate a possibility to deduce the relative role of SFI and IMP from careful analysis of the temporal structure the plasma density buildup exhibits.

Generally, the IMP rate is delayed compared to the SFI rate. Since IMP relies on

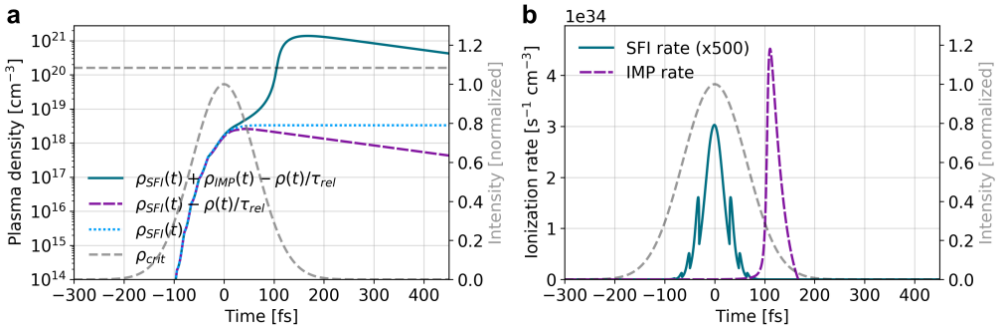

Fig. 8.2.1: **a**. Dynamics of the conduction band electron density induced by a 150 fs, 2.1 µm laser pulse of 15 TW cm^{-2} intensity. **b**. Corresponding SFI and IMP ionization rates. The SFI rate is multiplied by a factor of 500 for clarity.

the availability of seed electrons to trigger an avalanche effect it naturally starts later than SFI. According to Eq. 2.2.23 the IMP rate depends linearly on the laser intensity, hence both SFI as well as IMP are intrapulse excitation mechanisms. A more detailed analysis of the relative timing between SFI and IMP is displayed

in Fig. 8.2.2. Here the plasma formation due to SFI only [$\rho_{\mathrm{SFI}}(t)$] is compared to the conduction band electron density induced by SFI and IMP [$\rho_{\mathrm{tot}}(t)$]. The time delay between the maxima of the two resulting plasma density buildups Δt is used as an observable. Numerical simulations of Δt as a function of the laser intensity are presented for a pulse duration of 50 fs [Fig. 8.2.2(a)] and 150 fs [Fig. 8.2.2(b)].

Independent of the pulse duration and the laser wavelength the resulting values of Δt display an identical qualitative behavior. Naturally, at small intensities $\Delta t \approx 0$ since impact ionization only plays a negligible role. Once IMP starts to significantly influence the plasma dynamics Δt increases until it reaches a peak that is approximately on the order of the pulse duration. At even higher laser intensities an opposite behavior is observed. In this intensity regime SFI is able to produce a significant number of seed electrons for efficient electron-impact ionization already early in the pulse. Hence, the conduction band population reaches its maximum at earlier times. These observations indicate that the relative importance of SFI and IMP cannot directly be reconstructed from the temporal profile of the total plasma density alone due to the ambiguity of the relation between Δt and the laser intensity, i.e. $\Delta t(I)$ is a surjective but not an injective function.

Numerically, it is naturally easy to track the origin of excited conduction band

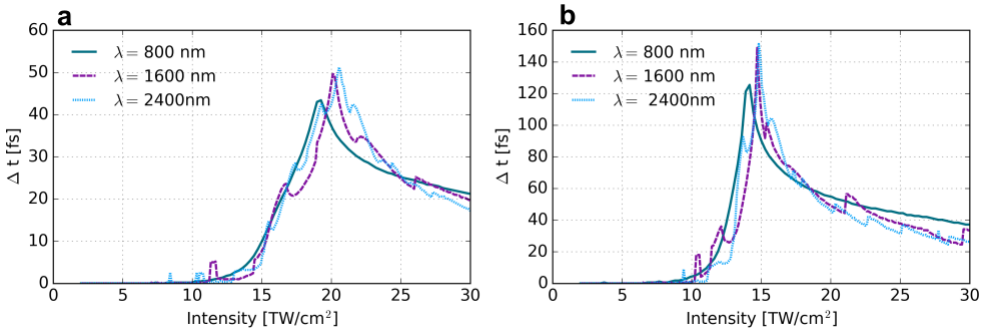

Fig. 8.2.2: Numerical simulations on the relative timing of SFI and IMP. **a**. Time delay between the maximum value of $\rho_{\mathrm{SFI}}(t)$ and $\rho_{\mathrm{tot}}(t)$ as a function of the excitation intensity for three different pump wavelengths ($\tau_p = 50$ fs). **b** Same as in **a** for $\tau_p = 150$ fs.

electrons. Based on the presented numerical approaches for SFI, IMP and solving the rate equation for the conduction band electron density (see Sec. 2.2) it is possible to determine the fraction of excited carriers generated by either SFI or IMP for a given set of experimental parameters. Numerical results obtained for the fraction of conduction band electrons generated by direct SFI are presented in Fig. 8.2.3.

The ratio of conduction band electrons excited by SFI in fused silica as a function of the laser wavelength and the peak intensity is displayed in Fig. 8.2.3(a)&(c) for

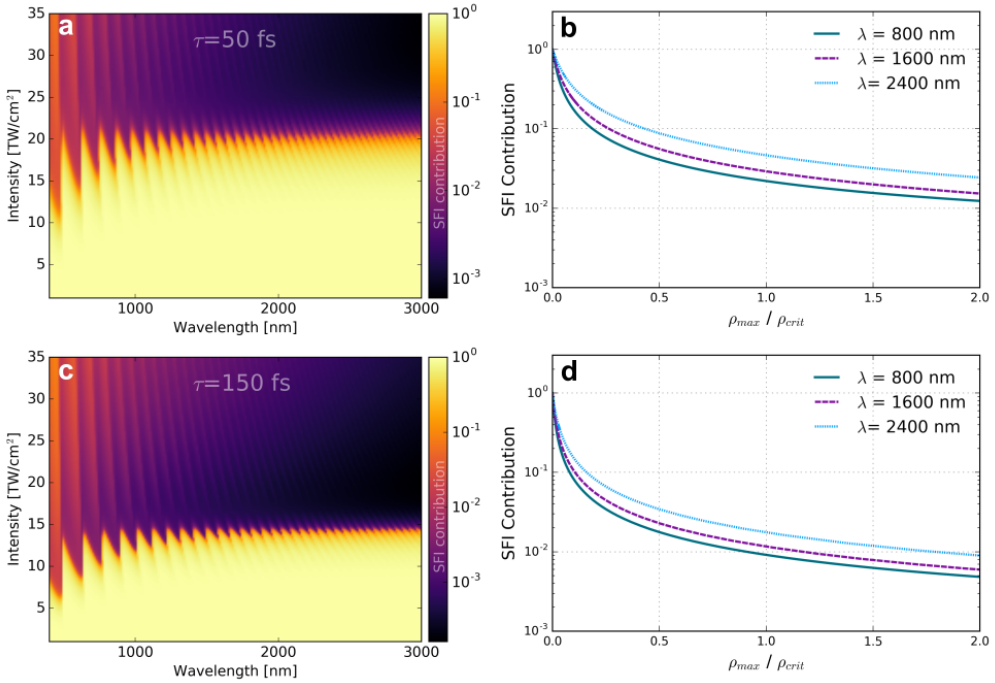

Fig. 8.2.3: Numerical simulations of the relative contribution of SFI to $\rho(t)$. **a**. SFI contribution as a function of wavelength and intensity for a pulse duration of 50 fs. **b** Ratio of free electrons generated by SFI depending on the relative carrier density with respect to the critical plasma density $\rho_{\max}/\rho_{\text{crit}}$ for a pulse duration of 50 fs. **c**. Same as in **a** for $\tau_p = 150$ fs. **d**. Same as in **b** for $\tau_p = 150$ fs

a fixed FWHM pulse duration of 50 fs and 150 fs, respectively. Pulse durations of 50 and 150 fs have been chosen to demonstrate the influence of the pulse duration on the relative contribution of SFI and IMP. As discussed in Ch. 2.2.6 the SFI rate according to Keldysh (see Eq. 2.2.4) is not well suited to compute the excitation probability resulting from the irradiation with few-cycle pulses due to the associated spectral width. Figure 8.2.3(b) & (d) show the dependence of the SFI contribution on the maximum conduction band electron density normalized with respect to the critical density according to Eq. 2.2.34. In the two-dimensional representation of the SFI contribution for a pulse duration of 50 fs [Fig. 8.2.3(a)] signatures of MPI order transitions are clearly visible in the regime of short wavelengths (up to $\approx 2\,\mu$m). In general, a threshold intensity can be observed above which IMP tends to dominate the plasma density buildup. Towards the mid-IR regime this threshold for dominating IMP converges. Comparing the behavior to the intensity dependence of the total SFI rate according to Keldysh (see Fig. 2.2.5) this is due to the dominance of TI over MPI and the relatively insensitive character of the SFI rate with respect to the wavelength in the tunneling domain. As a general rule, IMP governs the ionization of solid dielectrics at high laser intensities and long wavelengths. Such a trend is supported by the results obtained for a pulse duration of 150 fs [see Fig. 8.2.3(c)], where a similar behavior is observed. The only difference is the earlier onset of IMP in terms of laser intensity. Additionally, the signatures of MPI order transitions are even less pronounced indicating that longer pulse durations favor IMP. The general trend of stronger impact ionization for longer pulse durations is also shown by Figs. 8.2.3(b) & (d). Independent of the excitation wavelength the SFI contribution is clearly smaller for the longer pulse duration. Strikingly, a weaker influence of IMP for longer wavelengths is observed when analyzing the SFI contribution as a function of the maximum plasma density for a fixed pulse duration (Figs. 8.2.3(b) & (d) both show the highest SFI contribution for an excitation wavelength 0f 2400 nm irrespective of the pulse duration). Conversely, according to Eq. 2.2.24 a quadratic behavior of the impact ionization cross-section on the laser wavelength is predicted. Hence, a much stronger influence of IMP on the total plasma density for long driving wavelengths might be expected.
Using a fixed number of optical cycles of the excitation pulse instead of a fixed pulse duration in the simulations changes the described results. As already determined, shorter pulse durations favor SFI. Due to the longer duration of an optical cycle of long wavelength pulses, the usage of a fixed pulse duration to compare the importance of SFI and IMP for different wavelength regimes is misleading. Figure 8.2.4 shows numerical results obtained by fixing the number of optical cycles of the laser pulses used in the simulations. Figures 8.2.4(a) & (c) display the SFI contribution as a function of the laser intensity for pulse durations equal to 10 and 50 optical cycles, respectively. The ratio of SFI generated carriers as a function of the relative carrier density is displayed in Figs. 8.2.4(b) & (d). Analysis of the intensity dependence of the SFI contribution now indicates the prevalence of IMP for long driving wavelengths. In the case of the ten-optical-

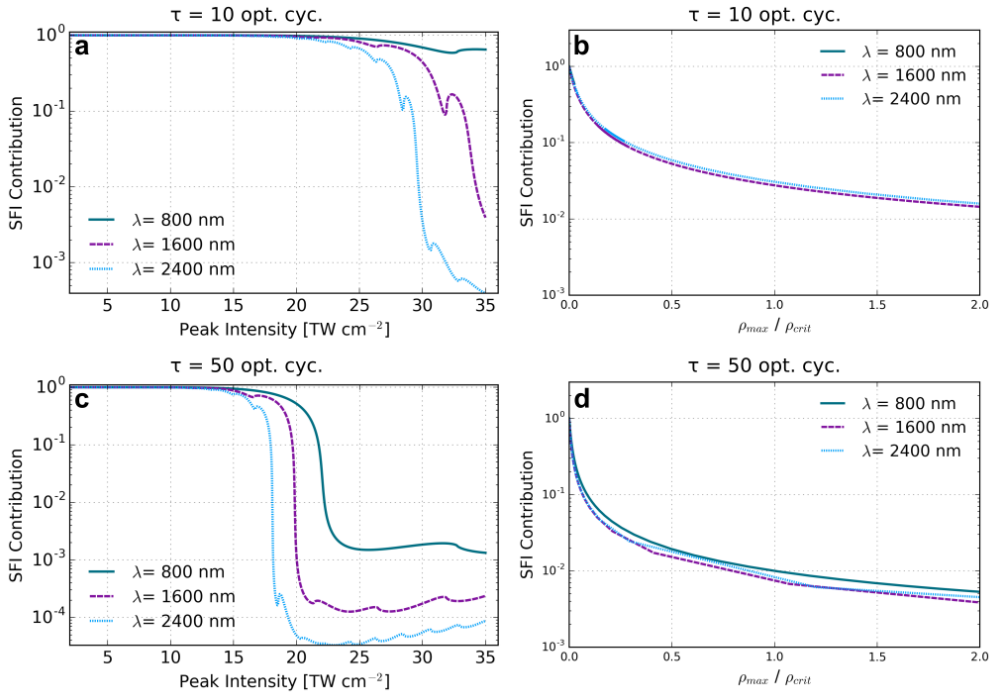

Fig. 8.2.4: Numerical simulations of the relative importance of SFI using a fixed number of optical cycles. **a**. SFI contribution as a function of the peak intensity for three different wavelengths and a pulse duration corresponding to ten optical cycles. **b**. Ratio of free electrons generated by SFI depending on generated carrier density normalized with respect to the critical density. The pulse duration corresponds to ten optical cycles of the driving field. **c**. Same as in **a** for a pulse duration of 50 optical cycles. **d**. Same as in **b** for a pulse duration of 50 optical cycles.

cycle driving pulse [see Fig. 8.2.4(a)] the onset of dominating IMP takes place at much higher intensities ($\approx 25\,\mathrm{TW\,cm^{-2}}$) compared to the 50-optical-cycle pulse ($\approx 15\,\mathrm{TW\,cm^{-2}}$). However, comparing the SFI contribution as a function of the maximum density of free carriers with respect to the critical density for different excitation wavelengths points out that the wavelength only has a minor influence on the excitation mechanisms that are involved to reach a certain conduction band population. On the contrary, the numerical results suggest that the duration of the excitation pulses - besides the intensity - mainly determines whether SFI or IMP dominates the ionization process.
In conclusion, it can be stated that - using the presented models for SFI and IMP and calculating the plasma dynamics by solving the rate equation given in Eq. 2.2.36 - the influence of IMP decreases for short pulse durations. Experimental evidence for the low relevance of IMP in laser-matter interaction using 43 fs pulses of 800 nm wavelength is given in Ref. [23]. Several compelling experimental and theoretical studies can be found claiming both the disappearance of IMP at short pulse durations and the opposite. As already outlined above, experimentally distinguishing between free carriers that are generated from SFI or IMP is extremely challenging. However, as reviewed in Sec. 3.4 and extensively analyzed experimentally in Ch. 6, SFI leads to a unique optical signature in the frequency domain that can potentially be exploited to isolate the plasma formation due to SFI from the total density of generated excited carriers. This might provide a new strategy to experimentally determine the relative importance of the two competing ionization mechanisms.

8.2.3 Experimental Results

Figure 8.2.5 displays experimental results obtained in order to isolate the temporal evolution of the plasma density due to SFI. A time-resolved spectrum containing the $n = 1$ harmonic generated by a $10\,\mathrm{TW\,cm^{-2}}$ pump laser pulse of 2.1 µm wavelength is shown in Fig. 8.2.5(a). The projection of the $n = 1$ harmonic on the delay axis is shown in Fig. 8.2.5(b) together with the temporal profile of the mid-IR pump laser pulse. Additionally, the direct integration of the temporal profile of the $n = 1$ harmonic is displayed. The integrated signal is obtained via

$$S_{n=1}(\tau) \propto \int_{-\infty}^{\tau} P_{n=1}(t)dt, \tag{8.2.1}$$

where $P_{n=1}(t)$ denotes the projection of the first harmonic order and $S_{n=1}(\tau)$ is the integrated signal.

Further results obtained by characterizing the transmission of the weak NIR probe laser pulse through the pump laser-induced electron-hole plasma as a function of the pump-probe delay are presented in Fig. 8.2.6. According to the algorithm described in Ch. 5 the temporal evolution of the total plasma density is separated into the contributions from SFI, IMP and relaxation. The

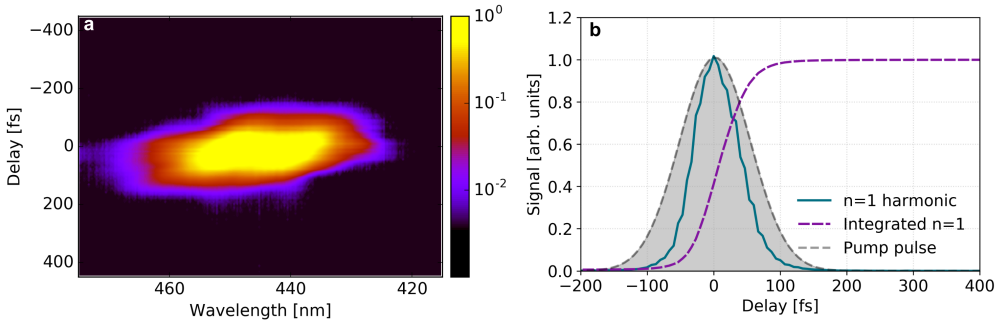

Fig. 8.2.5: **a**. Time-resolved spectrum showing the $n = 1$ harmonic obtained at a mid-IR laser intensity of $10\,\mathrm{TW\,cm^{-2}}$. **b**. Temporally integrated harmonic signal and integrated signal of the delay projection compared to the temporal profile of the pump laser pulse obtained by a Gaussian fit to the measured profile shown in Fig. 4.3.4(c).

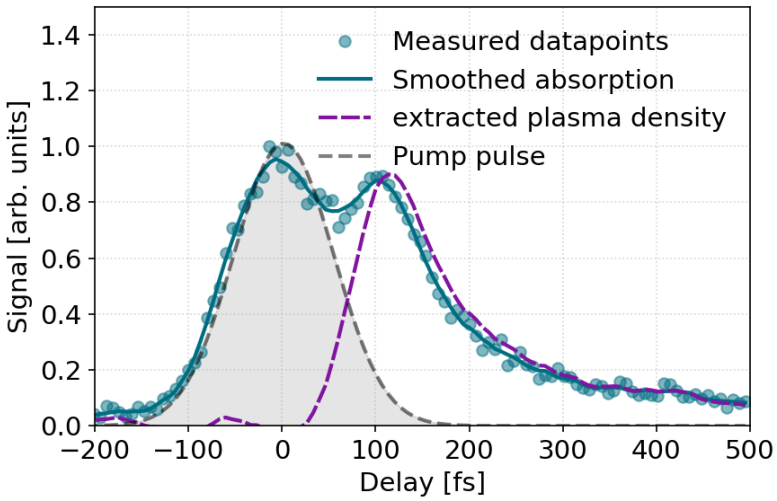

Fig. 8.2.6: Experimental results obtained by a time-resolved absorption measurement of the NIR probe laser pulse as discussed in Ch. 35 revealing the carrier dynamics due to SFI, IMP and relaxation mechanisms.

experimental results presented in Figs. 8.2.5 and 8.2.6 are acquired simultaneously where Fig. 8.2.5 displays results obtained by the harmonics analysis part of the detection unit and Fig. 8.2.6 shows results measured with the detectors of the probe analysis section (see also Fig. 4.2.2). Hence, the combination of the results exploits the full experimental setup described in Ch. 4.

8.2.4 Data processing

As established in Ch. 6 the observed harmonic emission is directly linked to interband transitions of electrons from the valence to the conduction band induced by the strong laser field. Accordingly, low-order harmonics are only generated when SFI occurs in the SiO_2 sample. Interpreting the temporally integrated signal $P_{n=1}(\tau)$ as a direct signature of SFI enables the reconstruction of the cycle-averaged dynamics of the conduction electron density induced by SFI. The direct integration of $P_{n=1}$ as described by Eq. 8.2.1 immediately yields the temporal structure of $\rho_{\mathrm{ca,SFI}}(t)$. Hence, the time-resolved detection of a single harmonic order is used to determine the plasma dynamics due to SFI. Chapter 5 provided a detailed description of the procedure allowing the isolation of the plasma density buildup from time-resolved transmission data. Applying this procedure results in the signal shown in Fig. 8.2.6.
In conclusion both results can be interpreted as a plasma density where the low-order harmonic spectra provide information on the SFI-induced plasma dynamics while the total plasma density buildup is extracted from the time-resolved absorption of the NIR probe laser pulse.

8.2.5 Discussion

The simultaneous acquisition of both $\rho_{\mathrm{SFI}}(t)$ and $\rho_{\mathrm{tot}}(t)$ enables the representation of the total plasma density and the formation of the electron-hole plasma due to SFI on a common time axis. A comparison of the total plasma formation and the evolution of the plasma density solely generated by SFI is displayed in Fig. 8.2.7. Clearly, the total plasma density increases at a significantly later point in time. While the temporal evolution of the plasma density due to SFI mainly occurs during the center of the excitation pulse the total plasma density displays a significant delay. The presented result demonstrates that for the given experimental parameters the time-resolved transmission measurement is insensitive to the plasma densities generated by SFI only. No absorption of the NIR probe laser pulse is induced by the electron-hole plasma produced by SFI. Hence, it can be stated that under the given experimental conditions IMP completely dominates the formation of an electron-hole plasma in SiO_2. This interpretation is furthermore supported by the clear delay that is observed between $\rho_{\mathrm{SFI}}(t)$ and $\rho_{\mathrm{tot}}(t)$ (for comparison see Fig. 8.2.2 and the accompanying discussion).
To compare the experimental result to the predictions of the numerical model,

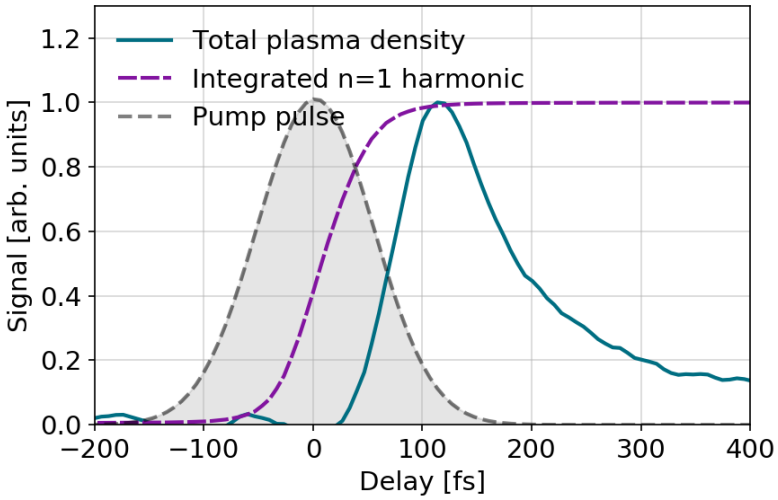

Fig. 8.2.7: Comparison of the integrated $n = 1$ harmonic signal attributed to the strong-field induced plasma formation and the temporal evolution of the total plasma density.

simulations under the conditions of the experiment are performed. Numerical results for the relative contribution of SFI to the laser-induced conduction band electron density are presented in Fig. 8.2.8 for a pump wavelength of 2.1 µm in fused silica (material parameters are taken from Tab. 2.1.1). The theoretical results predict a dominance of IMP over SFI only for mid-IR intensities of $\geq 15\,\mathrm{TW\,cm^{-2}}$ while at an intensity of $10\,\mathrm{TW\,cm^{-2}}$ SFI governs the excitation. The discrepancy between the experimental and the numerical results might be due to the nonlinear propagation of the mid-IR laser pulse in the SiO_2 sample. Since the simulation only accounts for the local response, nonlinear propagation effects are not considered in the simulation. The occurrence of self-focusing (see Sec. 2.1.1) might reduce the effective beam size of the mid-IR pump laser pulse in the focal plane resulting in an increased peak intensity. The effect of self-focusing on the ionization yield in bulk fused silica has been demonstrated by the dependence of the laser-induced damage threshold on the sample thickness [271]. Accordingly, it is extremely likely that self-focusing also influences the strength of the laser-driven ionization in the presented experiments and potentially causes the difference between the numerical and the experimental result.

In conclusion, an experimental procedure enabling the identification of the relative importance of SFI and IMP for the formation of an electron-hole plasma in transparent solids has been proposed and executed using a mid-IR pump laser pulse to excite a fused silica sample. The results show a strong predominance of IMP over SFI at an intensity close to the laser-induced damage threshold of the irradiated target. Furthermore, the detection of the optical signature of SFI provides a significantly enhanced tool for plasma diagnostics compared to

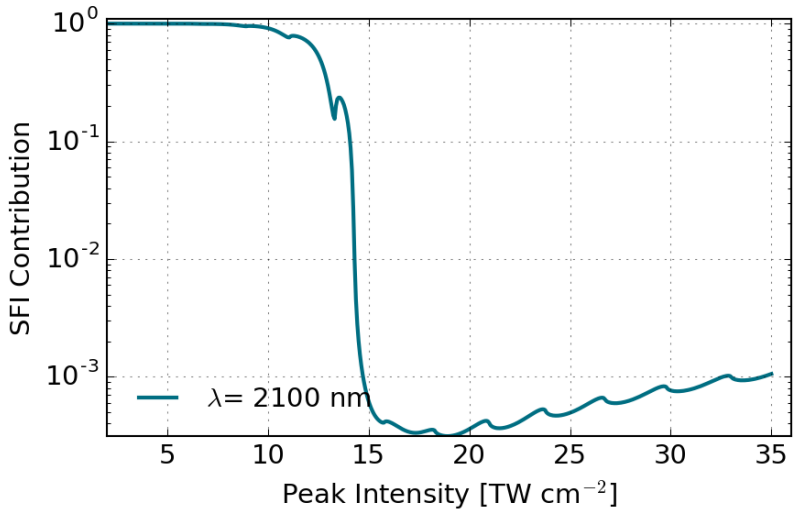

Fig. 8.2.8: Numerical simulation of the relative importance of SFI for the total plasma formation under the given experimental conditions in SiO_2.

conventional methods such as time-resolved absorption, reflectivity or phase shift measurements.

Chapter 9

Conclusion

In this thesis, the formation of an electron-hole plasma in bulk fused silica samples excited by fs MIR laser pulses was studied in a cross-polarized, close-to-collinear pump-probe experiment.
Relevant findings were reported in the experimental chapters even though some aspects remained unclear. Since several topics are covered within this thesis the present chapter is divided into four sections. To begin with, the time-resolved experiments on plasma formation and relaxation dynamics in fused silica are discussed. Afterwards, the chapter dedicated to the identification of the origin of low-order harmonic generation from strongly excited fused silica is reviewed. Therein, the newly discovered mechanism leading to the emission of low-order harmonics and possible continuations of the presented experiment are emphasized. Subsequently, the experimental investigations shedding light on the phase matching condition of the observed wave mixing process are summarized. Finally, the interpretation of the experimental results given in Ch. 8 is reviewed and connected to an outlook on possible future experimental studies.

Ultrafast excitation and relaxation dynamics in solid dielectrics The implementation of a pump-probe experiment for a time-resolved absorption and cross-phase modulation measurement was presented in Ch. 5 of this thesis. After describing the procedure to analyze the data, the time-resolved evolution of the plasma density was obtained. The decay of the electron-hole plasma density was approximated, following a commonly used approach, by a single exponential relaxation time. Extracting the experimentally determined relaxation time of the conduction band electron density as a function of the pump laser intensity revealed a strong dependence of the decay rate on the excitation strength. This result contradicts previous studies carried out in fused silica at different pump and probe wavelengths. A possible explanation for the discrepancy between the presented and previously reported results is based on a detrapping of trapped

carriers by vibrational activation of the medium and on the significantly higher ponderomotive energy of the electrons accelerated by MIR laser pulses compared to shorter wavelengths.
Besides extensive numerical studies, different follow-up experiments might be able to rationalize the observed results and provide deeper insights into the relaxation dynamics. By systematically changing the wavelength of the pump laser pulse from the ultraviolet to the mid-infrared spectral domain while keeping all remaining parameters unchanged, the potential influence of the ponderomotive energy on the relaxation time could be clarified. A second possible extension of the presented setup is the addition of a second probe laser pulse. Carefully selecting the photon energy of the second probe laser pulse to hit the absorption band of the self-trapped excitons leads to a resonant absorption of the additional probe laser pulse by the laser-induced intergap states. Time-resolved measurement of the transmission through the excited sample enables the extraction of the self-trapped exciton population as a function of the pump-probe delay [107]. Comparing the results obtained by the two probe laser pulses allows to determine whether the electron-hole plasma indeed decays into self-trapped excitons or if additional mechanisms govern the ultrafast relaxation of the conduction band population. Finally, using a probe laser pulse with a broad spectrum covering the range from the UV to the VIS spectral range would allow to study the variation of the defect population in a broad energy range within the bandgap as a function of the pump-probe delay. Hence, possible changes of the absorption at photon energies corresponding to interband states are a direct signature of a population gradient at particular defect levels. This transient absorption measurement over a wide spectral range would contain a plethora of information on dynamics of defect creation, plasma relaxation and electron-hole recombination in transparent solids.

Origin of low-order harmonic generation in solid dielectrics Chapter 6 was dedicated to the time-resolved detection of low-order harmonics generated by a two-color field in fused silica. With the help of experiments performed in crystalline quartz samples and extensive numerical modeling of the experiment by our collaboration partners from the University of Rostock all possible sources of harmonic generation presented in Ch. 3 could be excluded. A previously unreported mechanism associated with the transport of an electron through the potential barrier into the conduction band was identified as a novel source of harmonic generation in solids. Harmonic emission generated by the nonlinear ionization current not only complements the field of harmonic generation in solids but also provides an innovative technique to study ionization dynamics in bulk solids on a sub-cycle timescale.
A wide range of possible continuations could follow the presented experiments. Since the discussed novel harmonic generation mechanisms was only established for a specific set of experimental parameters a systematic study exploring the

influence of the material and the laser parameters - especially wavelength and pulse duration - would lead to a better understanding of the nonlinearity of strong-field ionization and its role in harmonic generation. Furthermore, determining the relative phase of the generated harmonics with respect to the phase of the excitation laser field would unequivocally identify the underlying harmonic generation process. Since this would require a laser system with a stabilized carrier envelope phase the proposed experiment cannot be realized employing the laser system used for the experiments presented in this thesis. Besides further completing the picture of high-order harmonic generation in solids in the low-order, strong-field driven regime the presented results may potentially have impact on applications such as ultrashort pulse laser micromachining. Due to the unprecedented insights on the plasma formation dynamics, time-resolved detection of low-order harmonics from laser excited solid dielectrics provides a powerful tool for further studies on fundamental as well as on applied topics.

Phase matching of low-order harmonic generation Chapter 7 was exclusively composed of experimental studies regarding the phase matching of low-order harmonic generation in fused silica. Experiments performed in gold-coated SiO_2 samples confirmed the enhanced conversion efficiency due to an increased reflectivity of the rear surface predicted by numerical simulations. Due to the laser-induced damage threshold of the gold coating, the intensity range of the measurements was severely limited. Hence, the influence of a gold coating on the rear surface of the substrates could only be studied in a regime where Kerr-type nonlinearities are expected to govern the harmonic generation. However, the phase matching condition for harmonic emission generated by either Kerr-type bound electron nonlinearities or by strong-field ionization should be nearly identical. For higher harmonic orders the importance of Kerr-type harmonics is expected to decrease significantly. Thus, using harmonic orders with $n \geq 2$ might result in a quasi-background-free measurement of the influence of a highly reflective rear surface on the generation of ionization current harmonics. An alternative approach is to improve the coating applied to the surface of the substrate in order to increase the reflectivity for the mid-infrared pump wavelength. A customized design of the optical coating increasing the reflectivity at the wavelength of the pump laser pulse would furthermore prevent harmonic generation within the coating.
Further experiments presented in Ch. 7 analyzed the influence of phase matching on the harmonic emission by analyzing the harmonic yield as a function of the angle of the sample with respect to the incoming pump and probe laser beams and by analyzing the spatial distribution of the pump, probe and $n = 1$ harmonic beam behind the target. Both measurements support the main hypothesis suggested by the numerical analysis indicating a non-conventional phase matching process influenced by the quasi-stationary grating formed inside the sample due to the reflection of the excitation field on the rear surface.

Linking carrier dynamics to harmonic generation The time-resolved detection of low-order harmonics generated by a two-color field in fused silica was linked to the dynamics of laser-induced plasma formation in Ch. 8. The application of an iterative phase retrieval algorithm enabled the reconstruction of the strong-field induced plasma formation with sub-cycle precision assuming that the harmonic emission results from the nonlinear Brunel current. As demonstrated in Ch. 6 the Brunel contribution does not govern the total plasma current density in the experimental configuration discussed in this thesis. Instead the ionization current was identified as the dominant source of nonlinearity leading to the observed low-order wave mixing signal at intensities close to the damage threshold of the fused silica samples. The challenges of the interpretation of the experimental results based on the establishment of the ionization current as a source of harmonic generation were discussed. Similar issues were discussed in the second section of Ch. 8 dedicated to the identification of the relative role of strong-field and electron-impact ionization in ultrafast plasma formation in solid dielectrics. Herein the temporal signature of the detected harmonics was compared to the total plasma density obtained by time-resolved absorption measurements. Interpreting the delay-dependent harmonic emission as a direct signature of strong-field ionization enables to reconstruct the cycle-averaged generation of conduction band electrons solely due to multiphoton or tunneling ionization. Hence, comparing the two experimental results reveals the relative importance of electron-impact ionization. It was found that under the given experimental conditions strong-field ionization only provides seed electrons to enable efficient collisional ionization but does not contribute significantly to the total number of conduction band electrons. This demonstrates that the proposed technique is able to identify plasma dynamics due to SFI even at plasma densities that are orders of magnitude smaller than the critical density.
Future advancements of the presented experimental strategies critically depend on the theoretical progress. Since the relationship between the strong-field induced carrier dynamics and the quantity retrieved from the time-resolved harmonic spectrum is unclear, a definite interpretation of the results provided by the ptychographic iterative engine is not feasible at this stage.

Bibliography

[1] E. N. Glezer, M. Milosavljevic, L. Huang, R. J. Finlay, T.-H. Her, J. P. Callan, and E. Mazur. Three-dimensional optical storage inside transparent materials. *Optics Letters*, 21(24):2023 – 2025, 1995.

[2] K. M. Davis, K. Miura, N. Sugimoto, and K. Hirao. Writing waveguides in glass with a femtosecond laser. *Optics Letters*, 21(21):1729 – 1731, 1996.

[3] K. Miura, J. Qiu, H. Inouye, T. Mitsuyu, and K. Hirao. Photowritten optical waveguides in various glasses with ultrashort pulse laser. *Applied Physics Letters*, 71(23):3329 – 3331, 1997.

[4] K. Mittholiya, P. K. Anshad, A. K. Mallik, S. Bhardwaj, A. Hedge, A. Bhatnagar, R. Bernard, J. A. Dharmadhikari, D. Mathur, and A. K. Dharmadhikari. Inscription of waveguides and power splitters in borosilicate glass using ultrashort laser pulses. *Journal of Optics*, 46(3):304 – 310, 2017.

[5] S. Nisar, L. Li, and A. Sheikh. Laser glass cutting techniques - A review. *Journal of Laser Applications*, 25(4), 2013.

[6] F. Ahmed, M. S. Lee, H. Sekita, T. Sumiyoshi, and M. Kamata. Display glass cutting by femtosecond laser induced single shot periodic void array. *Applied Physics A*, 93:189 – 192, 2008.

[7] R. R. Gattass and E. Mazur. Femtosecond laser micromachining in transparent materials. *Nature Photonics*, 2(4):219 – 225, 2008.

[8] D. Du, X. Liu, G. Korn, J. Squier, and G. Mourou. Laser-induced breakdown by impact ionization in SiO_2 with pulse widths from 7 ns to 150 fs. *Applied Physics Letters*, 64(23):3071 – 3073, 1994.

[9] P. P. Pronko, S. K. Dutta, J. Squier, J. V. Rudd, D. Du, and G. Mourou. Machining of sub-micron holes using a femtosecond laser at 800 nm. *Optics Communications*, 114:106 – 110, 1995.

[10] A. Mermillod-Blondin, B. Klessen, F. J. A. Furch, and M. J. J. Vrakking. Few-cycle pulses for bulk micromachining of fused silica. In *Proc. SPIE*, volume 9740, pages 9740 – 9740 –6. SPIE, 2016.

[11] F. J. Furch, W. D. Engel, T. Witting, A. Perez-Leija, M. J. J. Vrakking, and A. Mermillod-Blondin. Single-step fabrication of surface waveguides in fused silica with few-cycle laser pulses. *Optics Letters*, 44(17):4267 – 4270, 2019.

[12] P. A. Zhokhov and A. M. Zheltikov. Optical breakdown of solids by few-cycle laser pulses. *Scientific Reports*, 8(1824), 2018.

[13] N. Talisa and E. A. Chowdhury. Few cycle pulse laser ablation study of single layer TiO_2 thin films using time resolved surface microscopy. *Optics Express*, 26(23), 2018.

[14] M. Nisoli, S. Stagira, S. De Silvestri, O. Svelto, S. Sartania, Z. Cheng, M. Lenzner, Ch. Spielmann, and F. Krausz. A novel-high energy pulse compression system: generation of multigigawatt sub-5-fs pulses. *Applied Physics B*, 65:189 – 196, 1997.

[15] M. Nurhuda, A. Suda, M. Kaku, and K. Midorikawa. Optimization of hollow fiber pulse compression using pressure gradients. *Applied Physics B*, 89:209 – 215, 2007.

[16] M. Schultze, T. Binhammer, A. Steinmann, G. Palmer, M. Emons, and U. Morgner. Few-cycle OPCPA system at 143 kHz with more than 1 μJ of pulse energy. *Optics Express*, 18(3), 2010.

[17] J. Rothhardt, S. Demmler, S. Hädrich, J. Limpert, and A. Tünnermann. Octave-spanning OPCPA system delivering CEP-stable few-cycle pulses and 22 W of average power at 1 MHz repetition rate. *Optics Express*, 20(10), 2012.

[18] E. Mottay, X. Liu, H. Zhang, E. Mazur, R. Sanatinia, and W. Pfleging. Industrial applications of ultrafast laser processing. *MRS Bulletin*, 41(12):984 – 992, 2016.

[19] K. Sugioka and Y. Cheng. Ultrafast lasers - reliable tools for advanced materials processing. *Light Sci Appl*, 3(4), 2014.

[20] K. C. Phillips, J. H. Gandhi, E. Mazur, and S. K. Sundaram. Ultrafast laser processing of materials: a review. *Advances in Optics and Photonics*, 7(4):684 – 712, 2015.

[21] M. Malinauskas, A. Žukauskas, S. Hasegawa, Y. Hayasaki, V. Mizeikis, R. Buividas, and S. Juodkazis. Ultrafast laser processing of materials: from science to industry. *Light: Science & Applications*, 5(8), 2016.

[22] M. Jupé, L. Jensen, A. Melnikaitis, V. Sirutkaitis, and D. Ristau. Calculations and experimental demonstration of multi-photon absorption governing fs laser-induced damage in titania. *Optics Express*, 17(15), 2009.

[23] M. Gertsvolf, M. Spanner, D. M. Rayner, and P. B. Corkum. Demonstration of attosecond ionzation dynamics inside transparent solids. *J. Phys. B: At. Mol. Opt. Phys.*, 43:1 – 5, 2010.

[24] F. Brunel. Harmonic generation due to plasma effects in a gas undergoing multiphoton ionization in the high intensity limit. *J. Opt. Soc. Am. B*, 7(4):521 – 526, 1990.

[25] A. J. Verhoef, A. V. Mitrofanov, E. E. Serebryannikov, D. V. Kartashov, A. M. Zheltikov, and A. Baltuska. Optical Detection of Tunneling Ionization. *Phys Rev. Lett.*, 104(163904), 2010.

[26] A. V. Mitrofanov, A. J. Verhoef, E. E. Serebryannikov, J. Lumeau, L. Glebov, A. M. Zheltikov, and A. Baltuska. Optical Detection of Attosecond Ionization Induced by a Few-Cycle Laser Field in a Transparent Dielectric Material. *Phys. Rev. Lett.*, 106(147401), 2011.

[27] D. von der Linde and H. Schüler. Breakdown threshold and plasma formation in femtosecond laser-solid interaction. *J. Opt. Soc. Am. B*, 13(1), 1996.

[28] C. B. Schaffer, A. Brodeur, and E. Mazur. Laser-induced breakdown and damage in bulk transparent materials induced by tightly focused femtosecond laser pulses. *Measurement Science and Technology*, 12(1784), 2001.

[29] R. W. Boyd. *Nonlinear Optics*. Academic Press, 3rd edition, 2007.

[30] E. Dremetsika, B. Dlubak, S.-P. Gorza, C. Ciret, M.-B. Martin, S. Hofmann, P. Seneor, D. Dolfi, S. Massar, P. Emplit, and P. Kockaert. Measuring the nonlinear refractive index of graphene using the optical Kerr effect method. *Optics Letters*, 41(14):3281 – 3284, 2016.

[31] J. R. Gulley, S. W. Winkler, W. M. Dennis, C. M. Liebig, and R. Stoian. Interaction of ultrashort-laser pulses with induced undercritical plasmas in fused silica. *Physical Review A*, 85(013808), 2012.

[32] I. H. Malitson. Interspecimen comparison of the refractive index of fused silica. *J. Opt. Soc. Am.*, 55:1205 – 1208, 1965.

[33] M. J. Soileau, W. E. Willams, N. Mansour, and E. W. van Stryland. Laser-induced damage and the role of self-focusing. *Optical Engineering*, 28(10), 1989.

[34] D. Homoelle, L. Vuong, and A. L. Gaeta. Self-focusing effects in femtosecond laser-induced damage in solids. In *Conference on Lasers and Electro-Optics, 2004. (CLEO).*, volume 1, page 2 pp., 2004.

[35] L. B. Glebov. Intrinsic laser-induced breakdown of silicate glasses. In *Proc. SPIE 4679*, volume 4679, pages 4679 – 4679 – 11, 2002.

[36] R. M. Wood. *Laser-Induced Damage of Optical Materials*. CRC Press, 2003.

[37] D. Ristau, editor. *Laser-induced damage in optical materials*. CRC Press, 2014.

[38] R. H. Stolen and C. Lin. Self-phase-modulation in silica optical fibers. *Physical Review A*, 17(4), 1978.

[39] S. C. Pinault and M. J. Potasek. Frequency broadening by self-phase modulation in optical fibers. *J. Opt. Soc. Am. B*, 2(8), 1985.

[40] M. Nisoli, S. De Silvestri, and O. Svelto. Generation of high energy 10 fs pulses by a new pulse compression technique. *Appl. Phys. Lett.*, 68(2793), 1996.

[41] M. Hofer, M. E. Fermann, F. Haberl, M. H. Ober, and A. J. Schmidt. Mode locking with cross-phase and self-phase modulation. *Optics Letters*, 16(7), 1991.

[42] M. N. Islam, L. F. Mollenauer, R. H. Stolen, J. R. Simpson, and H. T. Shang. Cross-phase modulation in optical fibers. *Optics Letters*, 12(8), 1987.

[43] E. A. Anashkina, V. N. Ginzburg, A. A. Kochetkov, I. V. Yakovlev, A. V. Kim, and E. A. Khazanov. Single-shot laser pulse reconstruction based on self-phase modulated spectra measurements. *Scientific Reports*, 6(33749), 2016.

[44] J. J. Ferreiro, R. de La Fuente, and E. López-Lago. Characterization of arbitrarily polarized ultrashort laser pulses by cross-phase modulation. *Optics Letters*, 26(13):1025 – 1027, 2001.

[45] P. Audebert, Ph. Daguzan, A. Dos Santos, J. C. Gauthier, J. C. Geindre, S. Guizard, G. Hamoniaux, K. Krastev, P. Martin, G. Petite, and A. Antonetti. Space-Time Observation of an Electron Gas in SiO_2. *Physical Review Letters*, 73(14), 1994.

[46] B. C. Stuart, M. D. Feit, S. Herman, A. M. Rubenchik, B. W. Shore, and M. D. Perry. Nanosecond-to-femtosecond laser-induced breakdown in dielectrics. *Physical Review B*, 53(4), 1996.

[47] P. Martin, S. Guizard, Ph. Daguzan, G. Petite, P. d'Oliveira, P. Meynadier, and M. Perdrix. Subpicosecond study of carrier trapping dynamics in wide-band-gap crystals. *Phys. Rev. B*, 55(9):5799 – 5810, 1997.

[48] F. Quéré, S. Guizard, P. Martin, G. Petite, O. Gobert, P. Meynadier, and M. Perdrix. Ultrafast carrier dynamics in laser-excited materials: subpicosecond optical studies. *Appl. Phys. B*, 68:459 – 463, 1999.

[49] L. Sudrie, A. Couairon, M. Franco, B. Lamouroux, B. Prade, S. Tzortzakis, and A. Mysyrowicz. Femtosecond laser-induced damage and filamentary propagation in fused silica. *Physical Review Letters*, 89(186601), 2002.

[50] S. S. Mao, F. Quéré, S. Guizard, X. Mao, R. E. Russo, G. Petite, and P. Martin. Dynamics of femtosecond laser interactions with dielectrics. *Applied Physics A*, 79(7):1695 – 1709, 2004.

[51] M. Mero, J. Liu, W. Rudolph, K. Starke, and D. Ristau. Scaling laws of femtosecond laser pulse induced breakdown in oxide films. *Phys. Rev. B*, 71(115109), 2005.

[52] L. Gallais, D.-B. Douti, M. Commandré, G. Bataviciute, E. Pupka, M. Sciuka, L. Smalakys, V. Sirutkaitis, and A. Melninkaitis. Wavelength dependence of femtosecond laser-induced damage threshold of optical materials. *Journal of Applied Physics*, 117(223103), 2015.

[53] D. Grojo, M. Gertsvolf, S. Lei, T. Barrilot, D. M. Rayner, and P. B. Corkum. Exciton-seeded multiphoton ionization in bulk SiO_2. *Phys. Rev. B*, 81(212301), 2010.

[54] C. Zener. A theory of the electrical breakdown of solid dielectrics. In *Proc. R. Soc. Lond. A*, volume 145, pages 523 – 529, 1934.

[55] L. V. Keldysh. Ionization in the field of a strong electromagnetic wave. *Sov. Phys. JETP*, 20(5):1307 – 1314, 1965.

[56] A. M. Perelomov, V. S. Popov, and Terent'ev M. V. Ionization of atoms in an alternating electric field. *Sov. Phys. JETP*, 23(5), 1966.

[57] M. V. Ammosov, N. B. Delone, and V. P. Krainov. Tunnel ionization of complex atoms and of atomic ions in an alternating electromagnetic field. *Sov. Phys. JETP*, 64(6):1191 – 1194, 1986.

[58] G. L. Yudin and M. Y. Ivanov. Nonadiabatic tunnel ionization: Looking inside a laser cycle. *Physical Review A*, 64(1), 2001.

[59] P. A. Zhokhov and A. M. Zheltikov. Field-Cycle-Resolved Photoionization in Solids. *Phys. Rev. Lett.*, 119(133903), 2014.

[60] E. E. Serebryannikov, A. J. Verhoef, A. Mitrofanov, A. Baltuska, and A. M. Zheltikov. Signatures of attosecond electron tunneling dynamics in the evolution of intense few-cycle light pulses. *Phys. Rev. A*, 80(053809), 2009.

[61] L. V. Keldysh. Multiphoton ionization by a very short pulse. *Physics-Uspekhi*, 60(11):1187, 2017.

[62] P. A. Zhokhov and A. M. Zheltikov. Depth-resolved subcycle dynamics of photoionization in solids. *Physical Review A*, 96(033415), 2017.

[63] M. Uiberacker, Th. Uphues, M. Schultze, A. J. Verhoef, V. Yakovlev, M. F. Kling, J. Rauschenberger, N. M. Kabachnik, H. Schröder, M. Lezius, K. L. Kompa, H.-G. Muller, M. J. J. Vrakking, S. Hendel, U. Kleineberg, U. Heinzmann, M. Drescher, and F. Krausz. Attosecond real-time observation of electron tunneling in atoms. *Nature*, 446:627 – 632, 2007.

[64] A. P. Pati, I. S. Wahyutama, and A. N. Pfeiffer. Subcycle-resolved probe retardation in strong-field pumped dielectrics. *Nat. Comm.*, 6(7746), 2015.

[65] P. Eckle, A. N. Pfeiffer, C. Cirelli, A. Staudte, R. Dörner, , H. G. Muller, M. Büttiker, and U. Keller. Attosecond ionization and tunneling delay time measurements in helium. *Science*, 322(5907):1525 – 1529, 2008.

[66] D. Shafir, H. Soifer, B. D. Bruner, M. Dagan, Y. Mairesse, S. Patchkovskii, M. Y. Ivanov, O. Smirnova, and N. Dudovich. Resolving the time when an electron exits a tunnelling barrier. *Nature*, 485(7398):323, 2012.

[67] M. Schultze, M. Fieß, N. Karpowicz, J. Gagnon, M. Korbman, M. Hofstetter, S. Neppl, A. L. Cavalieri, Y. Komninos, Th. Mecouris, C. A. Nicolaides, R. Pazourek, S. Nagele, J. Feist, J. Burgdörfer, A. M. Azzeer, R. Ernstorfer, R. Kienberger, U. Kleineberg, E. Goulielmakis, F. Krausz, and V. S. Yakovlev. Delay in photoemission. *Science*, 328(5986):1658 – 1662, 2010.

[68] L. Torlina, F. Morales, J. Kaushal, I. Ivanov, A. Kheifets, A. Zielinski, A. Scrinzi, H. G. Muller, S. Sukiasyan, M. Ivanov, and O. Smirnova. Interpreting attoclock measurements of tunnelling times. *Nature Physics*, 11(6):503, 2015.

[69] I. Babushkin, A. J. Galan, V. Vaicaitis, A. Husakou, F. Morales, A. Demircan, J. R. C. Andrade, U. Morgner, and M. Ivanov. All-optical attoclock: accessing exahertz dynamics of optical tunnelling through terahertz emission. *arxiv*, (1803.04187), 2018.

[70] M. Y. Ivanov, M. Spanner, and O. Smirnova. Anatomy of strong field ionization. *J. Mod. Opt.*, 52(2 – 3):165 – 184, 2005.

[71] J. R. Gulley. Ultrafast laser-induced damage and the influence of spectral effects. *Optical Engineering*, 51(12), 2012.

[72] P. Jürgens, M. Jupé, M. Gyamfi, and D. Ristau. Ultrafast polychromatic ionization of dielectric solids. In G. J. Exarhos, V. E. Gruzdev, J. A. Menapace, D. Ristau, and MJ. Soileau, editors, *Laser-Induced Damage in Optical Materials 2016*, volume 10014. SPIE, 2016.

[73] S. Yamada, M. Noda, K. Nobusada, and K. Yabana. Time-dependent density functional theory for interaction of ultrashort light pulse with thin materials. *Physical Review B*, 98(24):245147, 2018.

[74] N. Bloembergen. Laser-induced electric breakdown in solids. *IEEE J. Quantum Electron.*, 10(375), 1974.

[75] A. S. Epifanov. Avalanche ionization induced in solid transparent dielectrics by strong laser pulses. *Sv. Phys. JETP*, 40(5), 1975.

[76] B. C. Stuart, M. D. Feit, A. M. Rubenchik, B. W. Shore, and M. D. Perry. Laser-Induced Damage in Dielectrics with Nanosecond to Subpicosecond Pulses. *Physical Review Letters*, 74(12), 1995.

[77] B. Rethfeld. Unified Model for the Free-Electron Avalanche in Laser-Irradiated Dielectrics. *Physical Review Letters*, 92(18), 2004.

[78] P. Drude. Zur Elektronentheorie der Metalle Teil I. *Annalen der Physik*, 1(566), 1900.

[79] P. Drude. Zur Elektronentheorie der Metalle Teil II. *Annalen der Physik*, 3(369), 1900.

[80] M. Fox. *Optical Properties of Solids*. Oxford University Press, 2002.

[81] M. D. Feit and J. J. A. Fleck. Effect of refraction on spot-size dependence of laser-induced breakdown. *Appl. Phys. Lett.*, 24(4), 1974.

[82] L. V. Keldysh. Kinetic theory of impact ionization in semiconductors. *Sov. Phys. JETP*, 37(10):509 – 518, 1960.

[83] A. Kaiser, B. Rethfeld, M. Vicanek, and G. Simon. Microscopic processes in dielectrics under irradiation by subpicosecond laser pulses. *Physical Review B*, 61(17), 2000.

[84] B. H. Christensen and P. Balling. Modeling ultrashort-pulse laser ablation of dielectric materials. *Physical Review B*, 79(155424), 2009.

[85] T. Winkler, L. Haahr-Lillevang, C. Sarpe, B. Zielinski, N. Götte, A. Senftleben, P. Balling, and T. Baumert. Laser amplification in excited dielectrics. *Nature Physics*, 2017.

[86] T. Apostolova and Y. Hahn. Modeling of laser-induced breakdown in dielectrics with subpicosecond pulses. *Journal of Applied Physics*, 88(2), 2000.

[87] S. W. Winkler, I. M. Burakov, R. Stoian, N. M. Bulgakova, A. Husakou, A. Mermillod-Blondin, A. Rosenfeld, D. Ashkenasi, and I. V. Hertel. Transient response of dielectric materials exposed to ultrafast laser radiation. *Applied Physics A*, 84:413 – 422, 2006.

[88] X. Mao, S. S. Mao, and E. Russo. Imaging femtosecond laser-induced electronic excitation in glass. *Applied Physics Letters*, 82(697), 2003.

[89] D. Giguére, G. Olivié, F. Vidal, S. Toetsch, G. Girard, T. Ozaki, J.-C. Kieffer, O. Nada, and I. Brunette. Laser ablation threshold dependence on pulse duration for fused silica and corneal tissues: experiments and modeling. *Journal of the Optical Society of America A*, 24(6), 2007.

[90] A. Q. Wu, I. H. Chowdhury, and X. Xu. Femtosecond laser absorption in fused silica: Numerical and experimental investigation. *Physical Review B*, 72(085128), 2005.

[91] Q. Sun, H. Jiang, Y. Liu, Z. Wu, H. Yang, and Q. Gong. Measurement of the collision time of dense electronic plasma induced by a femtosecond laser in fused silica. *Optics Letters*, 30(3):320 – 322, 2005.

[92] A. L. Gaeta. Catastrophic Collapse of Ultrashort Pulses. *Physical Review Letters*, 84(3582), 2000.

[93] A. Couairon, E. Gaižauskas, D. Faccio, A. Dubietis, and P. Di Trapani. Nonlinear X-wave formation by femtosecond filamentation in Kerr media. *Physical Review E*, 73(016608), 2006.

[94] A. Couairon, L. Sudrie, M. Franco, B. Prade, and A. Mysyrowicz. Filamentation and damage in fused silica induced by tightly focused femtosecond laser pulses. *Phys. Rev. B*, 71(125435), 2005.

[95] S. Tzortzakis, L. Sudrie, M. Franco, B. Prade, A. Mysyrowicz, A Couairon, and L. Bergé. Self-Guided Propagation of Ultrashort IR Laser Pulses in Fused Silica. *Physical Review Letters*, 87(213902), 2001.

[96] S. Skupin and L. Bergé. Self-guiding of femtosecond light pulses in condensed media: Plasma generation versus chromatic dispersion. *Physica D*, 220(14), 2006.

[97] J. R. Gulley and T. E. Lanier. Model for ultrashort laser pulse-induced ionization dynamics in transparent solids. *Physical Review B*, 90(155119), 2014.

[98] P. Balling and J. Schou. Femtosecond-laser ablation dynamics of dielectrics: basics and applications for thin films. *Reports on Progress in Physics*, 76(3), 2013.

[99] A. Couairon and a. Mysyrowicz. Femtosecond filamentation in transparent media. *Phys. Rep.*, 441:47 – 189, 2007.

[100] Y. M. Li and R. Fedosejevs. Ionization-induced blue shift of KrF laser pulses in an underdense plasma. *Phys. Rev. E*, 54(2):2166 – 2169, 1996.

[101] A. J. Verhoef, A. Mitrofanov, A. anad Zheltikov, and A. Baltuska. Plasma-blueshift spectral shear interferometry for characterization of ultimately short optical pulses. *Opt. Lett.*, 34(1):82 – 84, 2009.

[102] S. Guizard, P. Martin, Ph. Daguzan, G. Petite, P. Audebert, J. P. Geindre, A. Dos Santos, and A. Antonnetti. Contrasted Behaviour of an Electron Gas in MgO, Al_2O_3 and SiO_2. *Europhysics Letters*, 29(5), 1995.

[103] R. Stoian, K. Mishchik, G. Cheng, C. Mauclair, C. D'Amico, J. P. Colombier, and M. Zamfirescu. Investigation and control of ultrafast laser-induced isotropic and anisotropic nanoscale-modulated index patterns in bulk fused silica. *Opt. Mater. Express*, 3(10), 2013.

[104] A. N. Trukhin. Self-trapped exciton luminescence in α-quartz. *Nuclear Instruments and Methods in Physics Research Section B: Beam Interaction with Materials and Atoms*, 91(1 – 4):334 – 337, 1994.

[105] T. Sugiyama, H. Fujiwara, T. Suzuki, and K. Tanimura. Femtosecond time-resolved spectroscopy of self-trapping processes of holes and electron-hole pairs in alkali bromide crystals. *Physical Review B*, 1996.

[106] E. D. Thoma, H. M. Yochum, and R. T. Williams. Subpicosecond spectroscopy of hole and exciton self-trapping in alkali-halide crystals. *Physical Review B*, 56(8001), 1997.

[107] S. Guizard, P. Martin, G. Petite, P. D'Oliveira, and P. Meynadier. Time-resolved study of laser-induced colour centres in SiO_2. *Journal of Physics: Condensed Matter*, 8(1281), 1996.

[108] C. Itoh, K. Tanimura, and N. Itoh. Optical studies of self-trapped excitons in SiO_2. *J. Phys. C: Solid State Phys.*, 21:4693 – 4702, 1988.

[109] K. S. Song and R. T. Williams. *Self-Trapped Excitons*. Springer Berlin, Heidelberg, New York, 1993.

[110] M. Mero, J. Liu, A. Sabbah, J. Jasapara, K. Starke, D. Ristau, J. K. McIver, and W. Rudolph, editors. *Femtosecond pulse damage and pre-damage behavior of dielectric thin films*, volume 4932 of *Laser-Induced Damage in Optical Matls. 2002 / 7th Intl. Wkshp. on Laser Beam & Optics Characterization*. SPIE, G. Exarhos, A. Guenther, N. Kaiser, K. Lewis, M. Soileau, C. Stolz, A.Giesen, H. Weber, 2003.

[111] C. Pan, L. Jiang, Q. Wang, J. Sun, G. Wang, and Y. Lu. Temporal-spatial measurement of electron relaxation time in femtosecond laser induced plasma using two-color pump-probe imaging technique. *Appl. Phys. Lett.*, 112(191101), 2018.

[112] B. G. Gorshkov, A. S. Epifanov, and A. A. Manenkov. The relative role of impact and multiphoton ionization mechanisms in laser induced damage of transparent dielectrics. In A. J. Glass and A. H. Guenther, editors, *Damage in Laser Materials*, 1978.

[113] M. Lenzner, J. Krüger, S. Sartania, Z. Cheng, Ch. Spielmann, G. Mourou, W. Kautek, and F. Krausz. Femtosecond Optical Breakdown in Dielectrics. *Phys. Rev. Lett.*, 80(18):4076 – 4079, 1998.

[114] A.-C. Tien, S. Backus, H. Kapteyn, M. Murnane, and G. Mourou. Short-Pulse Laser Damage in Transparent Materials as a Function of Pulse Duration. *Physical Review Letters*, 82(3883), 1999.

[115] J. Jasapara, A. V. V. Nampoothiri, W. Rudolph, D. Ristau, and K. Starke. Femtosecond laser pulse induced breakdown in dielectric thin films. *Physical Review B*, 63(045117), 2001.

[116] N. Linz, S. Freidank, X.-X. Liang, and A. Vogel. Wavelength dependence of femtosecond laser-induced breakdown in water and implications for laser surgery. *Physical Review B*, 94(024113), 2016.

[117] M. Garcia-Lechuga, L. Haahr-Lillevang, J. Siegel, P. Balling, S. Guizard, and J. Solis. Simultaneous time-space resolved reflectivity and interferometric measurements of dielectrics excited with femtosecond laser pulses. *Physical Review B*, 95(214114), 2017.

[118] V. Gruzdev and O. Sergaeva. Ultrafast modification of band structure of wide-band-solids by ultrashort pulses of laser-driven electron oscillations. *Physical Review B*, 98(115202), 2018.

[119] O. Sergaeva, V. Gruzdev, D. Austin, and E. Chowdhury. Ultrafast excitation of conduction-band electrons by high-intensity ultrashort laser pulses in band-gap solids: Vinogradov equation versus Drude model. *Journal of the Optical Society of America B*, 35(11), 2018.

[120] C. Fourment, B. Chimier, F. Deneuville, D. Descamps, F. Dorchies, G. Duchateau, M.-C. Nadeau, and S. Petit. Ultrafast changes in optical properties of SiO_2 excited by femtosecond laser at the damage threshold and above. *Physical Review B*, 98(155110), 2018.

[121] M. Mero, B. Clapp, J. C. Jasapara, W. Rudolph, D. Ristau, K. Starke, J. Krüger, S. Marting, and W. Kautek. On the damage behavior of dielectrics films when illuminated with multiple femtosecond laser pulses. *Optical Engineering*, 44(5), 2005.

[122] A. R. Chowdhury, J. C. Dickens, A. A. Neuber, and R. P. Joshi. Assessing the role of trap-to-band impact ionization and hole transport on the

dark currents of 4H-SiC photoconductive switches containing deep defects. *Journal of Applied Physics*, 120(245705), 2016.

[123] E. Goulielmakis, M. Schultze, M. Hofstetter, V. S. Yakovlev, J. Gagnon, M. Uiberacker, A. L. Aquila, EM. Gullikson, D. T. Attwood, R. Keinberger, F. Krausz, and U. Kleineberg. Single-cycle nonlinear optics. *Science*, 320(5883):1614 – 1617, 2008.

[124] G. Sansone, E. Benedetti, F. Calegari, C. Vozzi, L. Avaldi, R. Flammini, L. Poletto, P. Villoresi, C. Altucci, R. Velotta, S. Stagira, S. De Silvestri, and M. Nisoli. Isolated Single-Cycle Attosecond Pulses. *Science*, 314(5798):443 – 446, 2006.

[125] M. Y. Shverdin, D. R. Walker, D. D. Yavuz, G. Y. Yin, and S. E. Harris. Generation of a Single-Cycle Optical Pulse. *Physical Review Letters*, 94(033904), 2005.

[126] Y. Kawakami, H. Itoh, K. Yonemitsu, and S. Iwai. Strong light-field effects driven by nearly single-cycle 7 fs light-field in correlated organic conductors. *Journal of Physics B: Atomic, Molecular and Optical Physics*, 51(17), 2018.

[127] K. Ramasesha, S. R. Leone, and D. M. Neumark. Real-Time Probing of Electron Dynamics Using Attosecond Time-Resolved Spectroscopy. *Annual review of physical chemistry*, 67:41 – 63, 2016.

[128] A. Sommer, E. M. Bothschafter, S. A. Sato, C. Jakubeit, T. Latka, O. Razskazovskaya, H. Fattahi, M. Jobst, W. Schweinberger, V. Shirvanyan, V. S. Yakovlev, R. Kienberger, K. Yabana, N. Karpowicz, M. Schultze, and F. Krausz. Attosecond nonlinear polarization and light-matter energy transfer in solids. *Nature*, 534:86 – 90, 2016.

[129] M. Schultze, K. Ramasesha, C. D. Pemmaraju, S. A. Sato, D. Whitmore, A. Gandman, J. S. Prell, L. J. Borja, D. Prendergast, K. Yabana, D. M. Neumark, and S. R. Leone. Attosecond band-gap dynamics in silicon. *Science*, 346(6215):1348 – 1352, 2014.

[130] J. Reimann, S. Schlauderer, C. P. Schmid, F. Langer, S. Baierl, K. A. Kokh, O. E. Tereshchenko, A. Kimura, C. Lange, J. Güdde, U. Höfer, and R. Huber. Subcycle observation of lightwave-driven Dirac currents in a topological surface band. *Nature*, 2018.

[131] M. Garg, M. Zhan, T. T. Luu, H. Lakhotia, T. Klostermann, A. Guggenmos, and E. Goulielmakis. Multi-petahertz electronic metrology. *Nature*, 538:359 – 363, 2016.

[132] A. Schiffrin, T. Paasch-Colbert, N. Karpowicz, V. Apalkov, D. Gerster, S. Mühlbrandt, M. Korbmann, J. Reichert, M. Schultze, S. Holzner, J. V.

Barth, R. Kienberger, E. Ernstorfer, V. S. Yakovlev, M. I. Stockmann, and F. Krausz. Optical-field-induced current in dielectrics. *Nature*, 493:70 – 74, 2013.

[133] M. Schultze, E. M. Bothschafter, A. Sommer, S. Holzner, W. Schweinberger, M. Fiess, M. Hofstetter, R. Kienberger, V. Apalkov, V. Yakovlev, M. I. Stockmann, and F. Krausz. Controlling dielectrics with the electric field of light. *Nature*, 493:75 – 78, 2013.

[134] P. B. Corkum. Plasma Perspective on Strong-Field Multiphoton Ionization. *Phys Rev. Lett.*, 71(13), 1993.

[135] K. J. Schafer, B. Yang, L. F. DiMauro, and K. C. Kulander. Above threshold ionization beyond the high harmonic cutoff. *Physical Review Letters*, 70(11):1599 – 1602, 1993.

[136] M. Lewenstein, Ph. Balcou, M. Yu. Ivanov, A. L'Huillier, and P. B. Corkum. Theory of high-harmonic generation by low-frequency laser fields. *Phys. Rev. A*, 49(3):2, 1994.

[137] P. B. Corkum and F. Krausz. Attosecond science. *Nature Physics*, 3:381 – 387, 2007.

[138] F. Krausz and M. Ivanov. Attosecond Physics. *Revies of Modern Physics*, 81(1), 2009.

[139] P. Colosimo, G. Doumy, C. I. Blaga, J. Wheeler, C. Hauri, F. Catoire, J. Tate, R. Chirla, A. M. March, G. G. Paulus, H. G. Muller, P. Agostini, and L. F. DiMauro. Scaling strong-field interactions towards the classical limit. *Nature Physics*, 4(5):386 – 389, 2008.

[140] G. Doumy, J. Wheeler, C. Roedig, R. Chirla, P. Agostini, and L. F. DiMauro. Attosecond synchronization of high-order harmonics from midinfrared drivers. *Physical Review Letters*, 102(093002), 2009.

[141] B. E. Schmidt, A. D. Shiner, M. Gigére, P. Lassonde, C. A. Trallero-Herrero, J. C. Kieffer, P. B. Corkum, D. M. Villeneuve, and F. Légaré. High harmonic generation with long-wavelength few-cycle laser pulses. *Journal of Physics B: Atomic, Molecular and Optical Physics*, 45(7):074008, 2012.

[142] D. Jang, R. M. Schwartz, D. Woodbury, J. Griff-McMahon, A. H. Younis, H. M. Milchberg, and K.-Y. Kim. Efficient terahertz and Brunel harmonic generation from air plasma via mid-infrared coherent control. *Optica*, 6(10):1338 – 1341, 2019.

[143] P. A. Franken, A. E. Hill, C. W. Peters, and G. Weinreich. Generation of Optical Harmonics. *Physical Review Letters*, 7(118), 1961.

[144] C. Q. Abadie, M. Wu, and M. B. Gaarde. Spatiotemporal filtering of high-order harmonics in solids. *Optics Letters*, 43(21), 2018.

[145] S. Almalki, A. M. Parks, G. Bart, P. B. Corkum, T. Brabec, and C. R. McDonald. High harmonic generation tomography of impurities in solids: Conceptual analysis. *Phys. Rev. B*, 98:144307, Oct 2018.

[146] S. Almalki, A. M. Parks, T. Brabec, and C. R. McDonald. Nanoengineering of Strong Field Processes in Solids. *J. Phys. B: At. Mol. Opt. Phys.*, 2018.

[147] A. Chacón, W. Zhu, S. P. Kelly, A. Dauphin, E. Pisanty, A. Picón, C. Ticknor, M. F. Ciappina, A. Saxena, and M. Lewenstein. Observing Topological Phase Transitions with High Harmonic Generation. *arxiv*, (1807.01616), 2018.

[148] Z.-Y. Chen and R. Qin. Circularly polarized extreme ultraviolet high harmonic generation in graphene. *Opt. Express*, 27(3):3761–3770, Feb 2019.

[149] L. A. Chizhova, F. Libisch, and J. Burgdörfer. High-harmonic generation in graphene: Interband response and the harmmonic cutoff. *Physical Review B*, 95(085436), 2017.

[150] N. Tancogne-Dejean, O. D. Mücke, F. Kärtner, and A. Rubio. Ellipticity dependence of high-harmonic generation in solids originating from coupled intraband and interband dynamics. *Nature Communications*, 8(745), 2017.

[151] N. Tancogne-Dejean, O. D. Mücke, F. Kärtner, and A. Rubio. Impact of the Electronic Band Structure in High-Harmonic Generation Spectra of Solids. *Physical Review Letters*, 118(087403), 2017.

[152] N. Tancogne-Dejean and A. Rubio. Atomic-like high-harmonic generation from two-dimensional materials. *Science Advances*, 4, 2018.

[153] T.-Y. Du and X.-B. Bian. Quasi-classical analysis of the dynamics of the high-order harmonic generation from solids. *Optics Express*, 25(1), 2017.

[154] P. Földi, M. G. Benedict, and V. S. Yakovlev. The effect of dynamical Bloch oscillations on optical-field-induced current in a wide-gap dielectric. *New J. Phys.*, 15, 2013.

[155] P. Földi. Gauge invariance and interpretation of interband and intraband processes in high-order harmonic generation from bulk solids. *Physical Revew B*, 96(035112), 2017.

[156] S. Ghimire, A. D. DiChiara, E. Sistrunk, G. Ndabashimiye, U. B. Szafruga, A. Mohammad, P. Agostini, L. F. DiMauro, and D. A. Reis. Generation and propagation of high-order hharmonic in crstals. *Phys. Rev. A*, 85, 2012.

[157] D. Golde, T. Meier, and S. W. Koch. High harmonics generated in semiconductor nanostructures by the coupled dynamics of optical inter- and intraband excitations. *Physical Review B*, 77(075330), 2008.

[158] D. Golde, M. Kira, T. Meier, and S. W. Koch. Microscopic theory of the extremely nonlinear terahertz response of semiconductors. *Phys. Status Solidi B*, 248(4), 2011.

[159] K. K. Hansen, D. Bauer, and L. B. Madsen. Finite-system effects on high-order harmonic generation: From atoms to solids. *Physical Review A*, 97(043424), 2018.

[160] P. G. Hawkins and M. Y. Ivanov. Role of subcycle transition dynamics in high-order-harmonic generation in periodic structures. *Phys. Rev. A*, 87(063842), 2013.

[161] P. G. Hawkins, M. Y. Ivanov, and V. S. Yakovlev. Effect of multiple conduction bands on high-harmonic emission from dielectrics. *Physical Review A*, 91(013405), 2015.

[162] T. Higuchi, M. I. Stockman, and P. Hommelhoff. Strong-Field Perspective on High-Harmonic Radiation from Bulk Solids. *Phys. Rev. Lett.*, 113(213901), 2014.

[163] U. Huttner, K. Schuh, J. V. Moloney, and S. W. Koch. Similarities and differences between high-harmonic generation in atoms and solids. *Journal of the Optical Society of America B: Optical Physics*, 33(7), 2016.

[164] M. Ivanov and O. Smirnova. Opportunities for sub-laser-cycle spectroscopy in condensed phase. *Chem. Phys.*, 414:3 – 9, 2013.

[165] G.-R. Jia, X.-H. Huang, and X.-B. Bian. Nonadiabatic redshifts in high-order harmonic generation from solids. *Optics Express*, 25(20), 2017.

[166] S. Jiang, H. Wei, J. Chen, C. Yu, R. Lu, and C. D. Lin. Effect of transition dipole phase on high-order-harmonic generation in solid materials. *Physical Review A*, 96(053850), 2017.

[167] J.-Z. Jin, X.-R. Xiao, H. Liang, M.-X. Wang, S.-G. Chen, Q. Gong, and L.-Y. Peng. High-order harmonic generation from a two-dimensional band structure. *Physical Review A*, 97(043420), 2018.

[168] L. Li, P. Lan, X. Zhu, T. Huang, and P. Lu. High harmonic generation with circularly polarized fields in solid: a quantum trajectory perspective. *arxiv*, (1805.12370), 2018.

[169] L. Li, P. Lan, X. Liu, L. He, X. Zhu, O. D. Mücke, and P. Lu. Method for direct observation of Bloch oscillations in semiconductors. *Optics Express*, 26(18), 2018.

[170] L. Li, P. Lan, X. Zhu, T. Huang, Q. Zhang, M. Lein, and P. Lu. Reciprocal-Space-Trajectory Perspective on High-Harmonic Generation in Solids. *Phys. Rev. Lett.*, 122:193901, May 2019.

[171] L. Liu, J. Zhao, W. Dong, J. Liu, Y. Huang, and Z. Zhao. Spatial coherence in high-order-harmonic generation from periodic solid structures. *Physical Review A*, 96(053403), 2017.

[172] X. Liu, X. Zhu, P. Lan, X. Zhang, D. Wang, Q. Zhang, and P. Lu. Time-dependent population imaging for high-order-harmonic generation in solids. *Physical Review A*, 95(063419), 2017.

[173] T. T. Luu and H. J. Wörner. High-order harmonic generation in solids: A unifying approach. *Physical Review B*, 94(115164), 2016.

[174] C. R. McDonald, G. Vampa, P. B. Corkum, and T. Brabec. Interband Bloch oscillation mechanism for high-harmonic generation in semiconductor crystals. *Physical Review A*, 92(033845), 2015.

[175] S. Gholam-Mirzaei, J. Beetar, and M. Chini. High harmonic generation in ZnO with a high-power mid-IR OPA. *Applied Physics Letters*, 110(061101), 2017.

[176] E. N. Osika, A. Chaćon, L. Ortmann, N. Suárez, J. A. Pérez-Hernández, B. Szafran, M. F. Ciappina, F. Sols, A. S. Landsmann, and M. Lewenstein. Wannier-Bloch Approach to Localization in High-Harmonics Generation in Solids. *Physical Review X*, 7(021017), 2017.

[177] R. E. F. Silva, I. V. Blinov, A. N. Rubtsov, O. Smirnova, and M. Ivanov. High-harmonic spectroscopy of ultrafast many-body dynamics in strongly correlated systems. *Nature Photonics*, 12(266), 2018.

[178] G. Vampa, C. R. McDonald, G. Orlando, P. B. Corkum, and T. Brabec. Semiclassical analysis of high harmonic generation in bulk crystals. *Physical Review B*, 91(064302), 2015.

[179] G. Vampa, C. R. McDonald, G. Orlando, D. D. Klug, P. B. Corkum, and T. Brabec. Theoretical Analysis of High-Harmonic Generation in Solids. *Phys. Rev. Lett.*, 113(073901), 2014.

[180] M. Wu, S. Ghimire, D. A. Reis, K. J. Schafer, and M. B. Gaarde. High-harmonic generation from Bloch electrons in solids. *Physical Review A*, 91(043839), 2015.

[181] M. Wu, Y. You, S. Ghimire, D. A. Reis, D. A. Browne, K. J. Schafer, and M. B. Gaarde. Orientation dependence of temporal and spectral properties of high-order harmonics in solids. *Physical Review A*, 96(063412), 2017.

[182] C. Yu, K. K. Hansen, and L. B. Madsen. Enhanced high-order harmonic generation in donor-doped band-gap materials. *Physical Review A*, 99(1), Jan 2019.

[183] J. Luo and F. Chen. High harmonic generation from a two-dimensional square lattice by a circularly polarized laser pulse. *Journal of the Optical Society of America B*, 2018.

[184] T.-Y. Du, D. Tang, and X.-B. Bian. Subcycle interference in high-order harmonic generation from solids. *Physical Review A*, 98(063416), 2018.

[185] T. N. Ikeda, K. Chinzei, and H. Tsunetsugu. Floquet-theoretical formulation and analysis of high-order harmonic generation in solids. *Physical Review A*, 98(063426), 2018.

[186] X. Liu, L. Li, X. Zhu, T. Huang, X. Zhang, D. Wang, P. Lan, and P. Lu. Wavelength dependence of high-order harmonic yields in solids. *Physical Review A*, 98(063419), 2018.

[187] D. Gauthier, S. Kaassamani, D. Franz, R. Nicolas, J.-T. Gomes, L. Lavoute, D. Gaponov, S. Février, G. Jargot, M. Hanna, W. Boutu, and H. Merdji. Orbital angular momentum from semiconductor high-order harmonics. *Opt. Lett.*, 44(3):546–549, Feb 2019.

[188] S. Ghimire, A. D. DiChiara, E. Sistrunk, P. Agostini, L. F. DiMauro, and D. A. Reis. Observation of high-order harmonic generation in a bulk crystal. *Nat. Phys.*, 7:138 – 141, 2011.

[189] S. Ghimire, G. Ndabashimiye, A. D. DiChiara, E. Sistrunk, M. I. Stockman, P. Agostini, L. F. DiMauro, and D. A. Reis. Strong-field and attosecond physics in solids. *J. Phys. B.: At. Mol. Opt. Phys.*, 47(204030), 2014.

[190] S. Gholam-Mirzaei, J. Beetar, and M. Chini. High harmonic generation in ZnO with a high-power mid-IR OPA. *Applied Physics Letters*, 110(061101), 2017.

[191] H. A. Hafez, S. Kovalev, J.-C. Deinert, Z. Mics, B. Green, N. Awari, M. Chen, S. Germanskiy, U. Lehnert, J. Teichert, Z. Wang, Z. Tielrooij, K.-J. andLiu, Z. Chen, A. Narita, K. Müllen, M. Bonn, M. Gensch, , and D. Tuchinovich. Extremely efficient terahertz high-harmonic generation in graphene by hot Dirac fermions. *Nature*, 2018.

[192] T. J. Hammond, S. Mochoć, C. Zhang, G. Vampa, D. Klug, A. Y. Naumov, D. M. Villeneuve, and P. B. Corkum. Integrating solids and gases for attosecond pulse generation. *Nature Photonics*, 11(594), 2017.

[193] M. Hohenleutner, F. Langer, O. Schubert, M. Knorr, U. Huttner, S. W. Koch, M. Kira, and R. Huber. Real-time observation of interfering crystal electrons in high-harmonic generation. *Nature*, 523(572), 2015.

[194] T. T. Luu, M. Garg, S. Yu. Kruchinin, A. Moulet, M. Th. Hassan, and E. Goulielmakis. Extreme ultraviolet high-harmonic spectroscopy of solids. *Nature*, 521:498 – 502, 2015.

[195] K. Kaneshima, Y. Shinohara, K. Takeuchi, N. Ishii, K. Imasaka, T. Kaji, S. Ashihara, K. L. Ishikawa, and J. Itatani. Polarization-Resolved Study of High Harmonics from Bulk Semiconductors. *Physical Review Letters*, 120(243903), 2018.

[196] F. Langer, Hohenleutner M., C. P. Schmid, C. Poellmann, P. Nagler, T. Korn, C. Schüller, M. S. Sherwin, U. Huttner, J. T. Steiner, S. W. Koch, M. Kira, and R. Huber. Lightwave-driven quasiparticle collisions on a subcycle timescale. *Nature*, 533(225), 2016.

[197] F. Langer, C. P. Schmid, S. Schlauderer, M. Gmitra, J. Fabian, P. Nagler, C. Schüller, T. Korn, P. G. Hawkins, J. T. Steiner, U. Huttner, S. W. Koch, M. Kira, and R. Huber. Lightwave valleytronics in a monolayer of tungsten diselenide. *Nature*, 557(76), 2018.

[198] A. A. Lanin, E. A. Stepanov, A. B. Fedotov, and A. M. Zheltikov. Mapping the electron band structure by intraband high-harmonic generation in solids. *Optica*, 4(5), 2017.

[199] K. F. Lee, X. Ding, T. J. Hammond, M. E. Fermann, G. Vampa, and P. B. Corkum. Harmonic generation in solids with direct fiber laser pumping. *Optics Letters*, 42(6), 2017.

[200] T. T. Luu, Z. Yin, A. Jain, T. Gaumnitz, Y. Pertot, J. Ma, and H. J. Wörner. Extreme-ultraviolet high-harmonic generation in liquids. *Nature Communications*, 9(3723), 2018.

[201] T. T. Luu, V. Scagnoli, S. Saha, L. J. Heyderman, and H. J. Wörner. Generation of coherent extreme-ultraviolet radiation from α-quartz using 50 fs laser pulses at 1030 nm wavelength and high repetition rates. *Optics Letters*, 2018.

[202] T. T. Luu and H. J. Wörner. Measurement of the Berry curvature of solids using high-harmonic spectroscopy. *Nature Communications*, 9(916), 2018.

[203] G. Ndabashimiye, S. Ghimire, M. Wu, D. A. Browne, K. J. Schafer, M. B. Gaarde, and D. A. Reis. Solid-state harmonics beyond the atomic limit. *Nature*, 534(520), 2016.

[204] N. Saito, P. Xia, F. Lu, T. Kanai, J. Itatani, and N. Ishi. Observation of selection rules for circularly polarized fields in high-harmonic generation from a crystalline solid. *Optica*, 4(11), 2017.

[205] O. Schubert, M. Hohenleutner, F. Langer, B. Urbanek, C. Lange, U. Huttner, D. Golde, T. Meier, M. Kira, S. W. Koch, and R. Huber. Sub-cycle control of terahertz high-harmonic generation by dynamical Bloch oscillations. *Nature Photonics*, 8(119), 2014.

[206] J. Seres, E. Seres, C. Serrat, and T. Schumm. High harmonic generation from surface states of solids. *arxiv*, (1805.00388), 2018.

[207] M. Sivis, M. Taucer, G. Vampa, K. Johnston, A. Staudte, A. Y. Naumov, D. M. Villeneuve, C. Ropers, and P. B. Corkum. Tailored semiconductors for high-harmonic optoelectronics. *Science*, 357(303), 2017.

[208] M. Taucer, T. J. Hammond, P. B. Corkum, G. Vampa, C. Couture, N. Thiré, B. E. Schmidt, F. Légaré, H. Selvi, N. Unsuree, B. Hamilton, T. J. Echtermeyer, and M. A. Denecke. Nonperturbative harmonic generation in graphene from intense midinfrared pulsed light. *Physical Review B*, 96(195420), 2017.

[209] G. Vampa, T. J. Hammond, N. Thiré, B. E. Schmidt, F. Légaré, C. R. McDonald, T. Brabec, D. D. Klug, and P. B. Corkum. All-Optical Reconstruction of Crystal Band Structure. *Physical Review Letters*, 2015.

[210] G. Vampa, T. J. Hammond, N. Thiré, B. E. Schmidt, Légaré F., C. R. McDonald, T. Brabec, and P. B. Corkum. Linking high harmonics from gases and solids. *Nature*, 522:462 – 464, 2015.

[211] G. Vampa and T. Brabec. Merge of high harmonic generation from gases and solids and its implications for attosecond science. *J. Phys. B: At. Mol. Opt. Phys.*, 50(083001), 2017.

[212] G. Vampa, Y. S. You, H. Liu, S. Ghimire, and D. A. Reis. Observation of backward high-harmonic emission from solids. *Optics Express*, 26(9), 2018.

[213] G. Vampa, B. G. Ghamsari, S. Siadat Mousavi, T. J. Hammond, A. Olivieri, E. Lisicka-Skrek, A. Yu Naumov, D. M. Villeneuve, A. Staudte, P. Berini, and P. B. Corkum. Plasmon-enhanced high-harmonic generation from silicon. *Nature Physics*, 13(659), 2017.

[214] Z. Wang, H. Park, Y. H. Lai, J. Xu, C. I. Blaga, F. Yang, P. Agostini, and L. F. DiMauro. The roles of photo-carrier doping and driving wavelength in high harmonic generation from a semiconductor. *Nature Communications*, 8(1686), 2018.

[215] Y. S. You, D. A. Reis, and S. Ghimire. Anisotropic high-harmonic generation in bulk crystals. *Nature Physics*, 13(345), 2016.

[216] Y. S. You, Y. Yin, Y. Wu, A. Chew, X. Ren, F. Zhuang, S. Gholam-Mirzaei, M. Chini, Z. Chang, and S. Ghimire. High-harmonic generation in amorphous solids. *Nature Communications*, 8(724), 2017.

[217] Y. S. You, J. Lu, E. F. Cunningham, C. Roedel, and S. Ghimire. Crystal orientation-dependent polarization state of high-order harmonics. *Opt. Lett.*, 44(3):530–533, Feb 2019.

[218] B. Zaks, R. B. Liu, and M. S. Sherwin. Experimental observation of electron-hole recollisions. *Nature*, 483(580), 2012.

[219] G. P. Zhang, M. S. Si, M. Murakami, Y. H. Bai, and T. F. George. Generating high-order optical and spin harmonics from ferromagnetic monolayers. *Nature Communications*, 9(3031), 2018.

[220] T. T. Luu and H. J. Wörner. Observing broken inversion symmetry in solids using two-color high-order harmonic spectroscopy. *Physical Review A*, 98(041802), 2018.

[221] S. Ghimire and D. A. Reis. High-harmonic generation from solids. *Nature Physics*, 2018.

[222] P. Xia, C. Kim, F. Lu, T. Kanai, H. Akiyama, J. Itatani, and N. Ishii. Nonlinear propagation effects in high harmonic generation in reflection and transmission from gallium arsenide. *Optics Express*, 26(22), 2018.

[223] M. Garg, H. Y. Kim, and E. Goulielmakis. Ultimate waveform reproducibility of extreme-ultraviolet pulses by high-harmonic generation in quartz. *Nature Photonics*, 1, 2018.

[224] J. Lu, E. F. Cunningham, Y. S. You, D. A. Reis, and S. Ghimire. Interferometry of dipole phase in high harmonics from solids. *Nature Photonics*, 2018.

[225] H. Park, A. Camper, K. Kafka, B. Ma, Y. H. Lai, C. Blaga, P. Agostini, L. F. DiMauro, and E. Chowdhury. High-order harmonic generations in intense MIR fields by cascaded three-wave mixing in a fractal-poled $LiNbO_3$ photonic crystal. *Optics Letters*, 42(19):4020 – 4023, 2017.

[226] T. Balcunias, A. J. Verhoef, A. V. Mitrofanov, G. Fan, E. E. Serebryannikov, M. Y. Ivanov, A. M. Zheltikov, and A. Baltuska. Optical and THz signatures of sub-cycle tunneling dynamics. *Chem. Phys.*, 414:92 – 99, 2013.

[227] C. W. Siders, G. Rodriguez, J. L. W. Siders, F. G. Omenetto, and A. J. Taylor. Measurement of Ultrafast Ionization Dynamics of Gases by Multipulse Interferometric Frequency-Resolved Optical Gating. *Phys. Rev. Lett.*, 87(26), 2001.

[228] C. Kittel. *Introduction to Solid State Physics*. John Wiley & Sons, Inc, 8 edition, 2004.

[229] F. Bloch. Über die Quantenmechanik der Elektronen in Kristallgittern. *Zeitschrift für Physik*, 52(7 – 8):555 – 600, 1929.

[230] C. Yu, S. Jiang, T. Wu, G. Yuan, Z. Wang, C. Jin, and R. Lu. Two-dimensional imaging of energy bands from crystal orientation dependent higher-order harmonic spectra in h-BN. *Physical Review B*, 98:085439, 2018.

[231] I. Babushkin, W. Kuehn, C. Köhler, S. Skupin, L. Berge, K. Reimann, M. Woerner, J. Herrmann, and T. Elsaesser. Ultrafast Spatiotemporal Dynamics of Terahertz Generation by Ionizing Two-Color Femtosecond Pulses in Gases. *Phys. Rev. Lett.*, 105(053903), 2010.

[232] I. Babushkin, C. Brée, C. M. Dietrich, A. Demircan, U. Morgner, and A. Husakou. Terahertz and higher-oder Brunel harmonics: from tunnel to multiphoton ionization regime in tailored fields. *Journal of Modern Optics*, 64(10 – 11):1078 – 1087, 2017.

[233] J. M. Khosrofian and B. A. Garetz. Measurement of a Gaussian laser beam diameter through the direct inversion of knife-edge data. *Applied Optics*, 22(21):3406 – 3410, 1983.

[234] Y. Suzaki and A. Tachibana. Measurement of the μm sized radius of Gaussian laser beam using the scanning knife-edge. *Applied Optics*, 14(12):2809 – 2810, 1975.

[235] M. A. C. de Araújo, R. Silva, E. de Lima, D. P. Pereira, and P. C. de Oliveira. Measurement of Gaussian laser beam radius using the knife-edge technique: improvement on data analysis. *Applied Optics*, 48(2):393 – 396, 2009.

[236] A. Rogalski, Martyniuk P., and M. Kopytko. Challenges of small-pixel infrared detectors: a review. *Rep. Prog. Phys.*, 79(046501), 2016.

[237] C. Iaconis and I. A. Walmsley. Spectral phase interferometry for direct electric-field reconstruction of ultrashort optical pulses. *Optics Letters*, 23(10):792 – 794, 1998.

[238] S. Ye and M. Huang. Direct observation of the reversible and irreversible processes in femtosecond laser-irradiated fused silica at the near-damage-threshold fluence. *arxiv*, (1803.02566), 2018.

[239] V. V. Temnov, K. Sokolowski-Tinten, P. Zhou, A. El-Khamhawy, and D. von der Linde. Multiphoton Ionization in Dielectrics: Comparison of Circular and Linear Polarization. *Phys Rev. Lett.*, 97(237403), 2006.

[240] M. Mero, A. J. Sabbah, J. Zeller, and W. Rudolph. Femtosecond dynamics of dielectrics films in the pre-ablation regime. *Applied Physics A*, 81:317 – 324, 2005.

[241] M. Lebugle, N. Sanner, N. Varkentina, M. Sentis, and O. Utéza. Dynamics of femtosecond laser absorption of fused silica in the ablation regime. *Journal of Applied Physics*, 116(063105), 2014.

[242] Y. Hayasaki, S. I. Fukuda, S. Hasegawa, and S. Juodkazis. Two-color pump-probe interferometry of ultra-fast light-matter interaction. *Scientific Reports*, 7(10405), 2017.

[243] A. Mouskeftaras, S. Guizard, N. Fedorov, and S. Klimentov. Mechanisms of femtosecond laser ablation of dielectrics revealed by double pump-probe experiment. *Applied Physics A*, 110:709 – 715, 2013.

[244] T. Tokizaki, T. Makimura, H. Akiyama, A. Nakamura, K. Tanimura, and N. Itoh. Femtosecond Cascade-Excitation Spectroscopy for Nonradiative Deexcitation and Lattice Relaxation of the Self-Trapped Exciton in NaCl. *Physical Review Letters*, 67(19), 1991.

[245] P. N. Saeta and I. Greene. Primary Relaxation Processes at the Band Edge of SiO_2. *Physical Review Letters*, 70(23), 1993.

[246] D. Strickland and G. Mourou. Compression of amplified chirped optical pulses. *Optics Communications*, 55(6), 1985.

[247] M. Mero, Z. Heiner, V. Petrov, H. Rottke, F. Branchi, G. M. Thomas, and M. J. J. Vrakking. 43 W, 1.55 μm and 12.5 W, 3.1 μm dual-beam, sub-10 cycle, 100 kHz optical parametric chirped pulse amplifier. *Optics Letters*, 43(21):5246 – 5249, 2018.

[248] M. Gebhardt, C. Gaida, F. Stutzki, S. Hädrich, C. Jauregui, J. Limpert, and A. Tünnermann. High average power nonlinear compression to 4 GW, sub-50 fs pulses at 2μm wavelength. *Optics Letters*, 42(4):747 – 750, 2017.

[249] B. W. Mayer, C. R. Phillipts, L. Gallmann, and U. Keller. Mid-infrared pulse generation via achromatic quasi-phase-matched OPCPA. *Optics Express*, 22(17), 2014.

[250] D. Grojo, S. Leyder, P. Delaporte, W. Marine, M. Sentis, and O. Utéza. Long-wavelength multiphoton ionization inside band-gap solids. *Phys. Rev. B*, 88(195135), 2013.

[251] A. H. Chin, O. G. Calder'on, and J. Kono. Extreme Midinfrared Nonlinear Optics in Semiconductors. *Physical Review Letters*, 86(15), 2001.

[252] D. R. Austin, K. R. P. Kafka, Y. H. Lai, Z. Wang, C. I. Blaga, and E. A. Chowdhury. Femtosecond laser damage of germanium from near- to mid-infrared wavelengths. *Optics Letters*, 43(15):3702 – 3705, 2018.

[253] A. Beer. Bestimmung der absorption des rothen lichts in farbigen flussigkeiten. *Ann. Physik*, 162:78 – 88, 1852.

[254] G. Petite, P. Daguzan, S. Guizard, and P. Martin. Ultrafast processes in laser irradiated wide bandgap insulators. *Applied Surface Science*, 109:36 – 42, 1997.

[255] I. Tanimura, T. Tanaka, and N. Itoh. Creation of Quasistable Lattice Defects by Electronic Excitation in SiO_2. *Physical Review Letters*, 51(423), 1983.

[256] M. Justin, G. Betchewe, S. Y. Doka, J. Y. Effa, and T. C. Kofane. Chaos in semiconductor band-trap impact ionization. *Current Applied Physics*, 13:1209 – 1212, 2013.

[257] C. Bonnelle. Multiphonon-induced charge trapping-detrapping and damage in insulators. *Physical Review B*, 81(054307), 2010.

[258] P. Jürgens, B. Liewehr, B. Kruse, C. Peltz, Engel D., A. Husakou, T. Witting, M. Ivanov, M. J. J. Vrakking, T. Fennel, and A. Mermillod-Blondin. Origin of strong-field induced low-order harmonic generation in amorphous solids. *arxiv*, (1905.05126), 2019.

[259] P. K. Velpula, M. K. Bhuyan, F. Curvoisier, H. Zhang, . P. Colombier, and R. Stoian. Spatio-temporal dynamics in nondiffractive Bessel ultrafast laser nanoscale volume structuring. *Laser Photonics Rev.*, 10(2):230 – 244, 2016.

[260] R. W. Boyd, Z. Shi, and I. De Leon. The third-order nonlinear optical susceptibility of gold. *Optics Communications*, 326:74 – 79, 2014.

[261] U. Gubler and C. Bosshard. Optical third-harmonic generation in fused silica in gas atmosphere: Absolute value of the third-order nonlinear optical susceptibility $\chi^{(3)}$. *Physical Review B*, 61(16), 2000.

[262] R. Trebino. *Frequency-resolved optical gating: the measurement of ultrashort laser pulss*. Springer Science & Business Media, 2012.

[263] R. Trebino, K. W. DeLong, D. N. Fittinghoff, J. N. Sweetser, M. A. Krumbügel, B. A. Richman, and D. J. Kane. Measuring ultrashort laser pulses in the time-frequency domain using frequency-resolved optical gating. *Review of Scientific Instruments*, 68(9):3277 – 3295, 1997.

[264] S. Linden, H. Giessen, and J. Kuhl. XFROG - A New Method for Amplitude and Phase Characterization of Weak Ultrashort Pulses. *phys. stat. sol. (b)*, 206(119):119 – 124, 1998.

[265] R. Trebino and D. J. Kane. Using phase retrieval to measure the intensity and phase of ultrashort pulses: frequency-resolved optical gating. *Journal of the Optical Society of America A*, 10(5):1101 – 1111, 1993.

[266] D. Spangenberg, P. Neethling, E. Rohwer, M. H. Brügmann, and T. Feurer. Time-domain ptychography. *Phys. Rev. A*, 91(2):021803, 2015.

[267] T. Witting, D. Greening, D. Walke, P. Matia-Hernando, T. Barillot, J. P. Marangos, and J. W. G. Tisch. Time-domain ptychography of over-octave

spanning laser pulses in the single-cycle regime. *Optics Letters*, 41(18):4218 – 4221, 2016.

[268] J. Hyyti, E. Escoto, Steinmeyer G., and T. Witting. Interferometric time-domain ptychography for ultrafast pulse characterization. *Optics Letters*, 42(11):2185 – 2188, 2017.

[269] A. Mermillod-Blondin, P. Jürgens, B. Liewehr, B. Kruse, C. Peltz, T. Witting, A. Husakou, M. Ivanov, T. Fennel, and M. J. J. Vrakking. Study of plasma formation in solid dielectrics with the help of low-order harmonic emission. In Tetsuya Makimura, Gediminas Račiukaitis, and Carlos Molpeceres, editors, *Laser Applications in Microelectronic and Optoelectronic Manufacturing (LAMOM) XXIV*, volume 10905, pages 64 – 69. International Society for Optics and Photonics, SPIE, 2019.

[270] A. Vaidyanathan, T. Walker, and A. Guenther. The relative roles of avalanche multiplication and multiphoton absorption in laser-induced damage of dielectrics. *IEEE Journal of Quantum Electronics*, 16(1):89 – 93, 1980.

[271] M. Turowski, M. Jupé, L. Jensen, and D. Ristau. Laser-induced damage and nonlinear absorption of ultrashort laser pulses in the bulk of fused silica. In *Laser-Induced Damage in Optical Materials*, volume 7504. International Society for Optics and Photonics, 2009.

List of Publications

- **P. Jürgens**, T. Witting, B. Liewehr, B. Kruse, C. Peltz, A. Husakou, M. Ivanov, M. J. J. Vrakking, T. Fennel and A. Mermillod-Blondin, **On the relative contribution of strong-field and avalanche ionization during optical breakdown of fused silica** (in preparation).

- **P. Jürgens**, T. Witting, B. Liewehr, B. Kruse, C. Peltz, A. Husakou, M. Ivanov, M. J. J. Vrakking, T. Fennel and A. Mermillod-Blondin, **Real time monitoring of femtosecond laser-induced plasma formation in a solid dielectric** (in preparation).

- **P. Jürgens**, B. Liewehr, B. Kruse, C. Peltz, D. Engel, A. Husakou, M. Ivanov, M. J. J. Vrakking, T. Fennel and A. Mermillod-Blondin, **Self-regulating enhancement of two-color wave mixing in amorphous fused silica** (in preparation).

- **P. Jürgens**, B. Liewehr, B. Kruse, C. Peltz, D. Engel, T. Witting, A. Husakou, M. Ivanov, M. J. J. Vrakking, T. Fennel and A. Mermillod-Blondin, **Origin of strong-field induced low-order harmonic generation in amorphous quartz**, *Nature Physics* (under review).

- **P. Jürgens**, M. J. J. Vrakking, A. Husakou, R. Stoian and A. Mermillod-Blondin, **Plasma formation and relaxation dynamics in fused silica driven by femtosecond short-wavelength infrared laser pulses**, *Applied Physics Letters*, **115**, 191903 (2019).

- A. Mermillod-Blondin, **P. Jürgens**, B. Liewehr, B. Kruse, C. Peltz, T. Witting, A. Husakou, M. Ivanov, T. Fennel and M. J. J. Vrakking, **Study of plasma formation in solid dielectrics with the help of low-order harmonic emission** *Proc. SPIE* **10905**, pp. 64 - 69 (2019).

- **P. Jürgens**, M. Jupé, M. Gyamfi, D. Ristau, **Ultrafast polychromatic ionization of dielectric solids**, *Proc. SPIE* **10014**, pp. 10014 (2016).

- M. Gyamfi, M. Costella, T. Willemsen, **P. Jürgens**, M. Mende, L. Jensen, D. Ristau, **Dual wavelength laser damage mechanisms in the ultra-short pulse regime**, *Proc. SPIE* **10014**, pp. 10014 (2016).
- M. Gyamfi, **P. Jürgens**, L. Jensen, D. Ristau, **Delay dependency of two-pulse femtosecond laser damage** *Proc. SPIE* **9632**, pp. 9632 (2015).
- M. Gyamfi, **P. Jürgens**, M. Mende, L. Jensen, D. Ristau, **Dual-wavelength ultra-short pulse laser damage testing** *Proc. SPIE* **9237**, pp. 9237 (2014).

Acknowledgements

In the first place I would like to thank Prof. Marc Vrakking for giving me the opportunity to carry out my research at the Max-Born-Institute.
Further, I would like to express my thanks and gratitude to Prof. Thomas Baumert for co-refereeing this thesis.

My biggest thanks goes to my daily supervisor Dr. Alexandre Mermillod-Blondin. From my very first day at the Max-Born-Institute he made me feel welcome and treated me as a full-fledged member of his group. He always infected me with his enthusiasm and never failed to push me when I was tired. Dear Alexandre, without you this thesis would not have been possible, it is an honor working with you.

I would also like to express my deepest gratitude to the Rostock crew, Prof. Thomas Fennel, Dr. Christian Peltz, Benjamin Liewehr and Björn Kruse. Your expertise, creativity and unremitting efforts made the current interpretation of the low-order harmonics possible and I will always keep our "Brunel-power-days" in good memory.

I would like to thank Christoph Reiter and Dr. Tamas Nagy for keeping the laser in shape throughout the experimental campaigns and their unconditional support with problems. Further, I would like to thank Roman Peslin for his indispensable technical support, Dr. Dieter Engel for preparing the gold-coated samples and Dr. Tobias Witting for the phase retrieval. Thanks to Dr. Anton Husakou and Prof. Misha Ivanov for their theoretical support and the extremely instructive discussions on strong-field ionization and wave mixing in solids and especially to Dr. Arkadi Rosenfeld - without his ideas and experience in the lab the setup would not have looked the same.

Thanks to all the staff at MBI for supporting my work, especially to Dr. Federico Furch, Dr. Mark Mero, Dr. Oleg Kornilov, Dr. Arnaud Rouzée, Dr. Jochen Mikosch, Dr. Andrea Lübcke, Catrin Damm, Sabine Winter, Petra Rapelius and Ute Schlichting.

In addition, I would also like to thank my current and former fellow PhD and Master students Martin Galbraith, Achut Giree, Faruk Krecinic, Felix Brausse, Janne Hyyti, Lorenz von Grafenstein, Felix Willems, Esmerando Escoto, Felix Mahler, Evgenii Ikonnikov, Ulrich 'Uli' Bengs, Kathinka Gerlinger, Mara Osswald, Mikhail 'Mike' Osolodkov, Katharina Kolatzki, Pascal Engl, Björn Senfftleben, Milica Valent, Nicola Mayer and especially my office mates and the members of the "Festkomitee" Katrin Reininger, Florian Bach, Lorenz Drescher, Johann Hummert, Thomas Kubail Kalousdian and Janina Lebendig-Kuhla for all the fun times, the barbecues the karaoke nights etc...

Lastly, my biggest thanks to my family and friends for their loving support throughout the past years - you know who you are and you know what you mean to me!
I am especially grateful to Kathrin & Emma for supporting me and putting up with me during the most exhausting and sometimes frustrating experimental campaigns.

π, the last line is for you. I am inconceivably grateful for everything that was, that is and that will be.

Selbstständigkeitserklärung

Hiermit versichere ich, die vorliegende Arbeit selbstständig verfasst und keine anderen als die angegebenen Quellen und Hilfsmittel benutzt sowie die Zitate deutlich kenntlich gemacht zu haben. Die Arbeit ist weder in einem früheren Promotionsverfahren angenommen noch als ungenügend beurteilt worden.

Berlin, March 3, 2021 Peter Jürgens